page1 0

The attenuation of atmospheric Cerenkov photons

by **Michael Kevin Daniel**, M. Phys.

A thesis submitted to the University of Durham in accordance with the regulations for the admittance to the degree of Doctor of Philosophy.

September, 2002.

Department of Physics
University of Durham

Abstract

Whilst the atmosphere places a limit on the successful applications of many branches of astronomy, it becomes an invaluable tool for the detection of very high energy γ-rays. This thesis is concerned with reducing the systematic uncertainties inherent to using the atmosphere as a detector of very high energy radiation. The interaction processes important to high energy particles are met in the first chapter. The second chapter explores how these interaction processes are responsible for generating observable Cerenkov radiation that can be detected by ground based telescopes. A description of one of these atmospheric Cerenkov telescopes, the University of Durham Mark 6 telescope, is given in chapter 3. A timing analysis was performed on data obtained with this telescope of the high mass X-ray binary Centaurus X-3 and the findings are given in chapter 5. The result of the test for orbital modulation of the VHE γ-ray signal has implications for the possible site of VHE γ-ray emission in this system and for the analysis strategy required to test for modulation of the VHE signal at the pulsar period. One of the findings of the timing analysis was a need for more accurate flux estimates and spectral energy measurements of the VHE γ-ray signal, which requires a greater understanding of the systematic errors inherent to the atmospheric Cerenkov technique.

The effective collecting area of a Cerenkov telescope is related to the generation and attenuation of Cerenkov photons in the atmosphere. Uncertainties in the magnitude of the effective area result in errors in the deduced flux, whilst uncertainties in the function of effective area with energy result in errors of the spectral slope determined for any source. By using an inappropriate model for the atmosphere in simulations of atmospheric Cerenkov telescopes a systematic error can be introduced into calculations of the effective area. Chapter 6 compares the effective areas obtained from several model atmosphere types, including a contemporary model of the conditions at the Mark 6 site from data taken with atmospheric monitoring equipment employed in the Mark 6 operations.

The findings from this work are then all drawn together in the final chapter, along with a discussion of the future atmospheric monitoring work that will go in to the next generation of atmospheric Cerenkov telescope installations.

Preface

The work in this thesis is based on data taken with the University of Durham Mark 6 telescope (which was sited in Narrabri, New South Wales). The author has been involved in the pre-processing and analysis of data taken with this telescope and was part of the observational team for one dark moon period before the telescope was dismantled in April, 2000.

The re-analysis of the Cen. X-3 data set by the author, given in chapter 5, was part of a collaborative effort to refine the theoretical models of Armen Atoyan concerning γ-ray emission from X-ray binaries. The findings of the study having been published in [10].

The MODTRAN code, used in the atmospheric modelling of chapter 6, was developed by the Air Force Research Lab., Space Vehicles Directorate and was adapted by the author for use in this study.

None of the material contained in this thesis has been submitted previously to a degree in this or any other university. The work of others has been duly acknowledged.

Acknowledgements

There are many people responsible in aiding my thesis to this present state. This work has been made possible through my research studentship, funded by the Particle Physics and Astronomy Research Council, and the provision of the facilities of the Physics Department at the University of Durham, for which I thank Professor Michael Pennington. My supervisor, Keith Orford, has been one of many at the Observatory to provide guidance and insight to my research and I take this opportunity to thank Paula Chadwick, Steve Rayner and John Osborne for their invaluable advice. I would also like to thank Armen Atoyan who, in his three month stay at the Observatory, led my research along a most unexpected, but worthwhile path. The efforts of the technical staff at the Observatory have done much to give a professional shine to my laboratory fumblings and to extend my database of dirty jokes and I thank Susan Hilton, Ken Tindale and John Webster for this. Last, but by no means least, are my fellow students. They have ranged from the short visit of Jacek Niemiec to Sam Nolan's three years as office-mate and I would like to thank them along with Klaus-Michael Aye, Karl Lyons, Simon Shaw, Aristeidis Noutsos and Ian Latham for many interesting pub lunches and more.

Acknowledging people is like being asked to name your favourite film, an impossible task. There are so many out there, each with their own unique qualities, that to name a few would be a disservice to the many. Joy is a fleeting concept, so to those that have brought light to the darkest moments I give thanks: ensure I have shaken you by the hand and bought you a drink in gratitude. The only advice I can give is to read the acknowledgements of J. E. H. Turner and to add sweet potato when you mix the two pans. Serve with friends for full flavour...

Contents

Chapter 1

An introduction to the non-thermal universe

1.1 Introduction

The maturity of any astronomical field can be traced through many indicators. It begins by testing the equipment and techniques necessary to provide an unambiguous detection of a signal, at which point it can begin looking for sources of the radiation of interest. If a flux of radiation is detected from an object then it becomes necessary to try and understand the mechanisms at work in that object. The modelling and matching of theoretical spectra to observationally gained ones allows us to quantify the processes at work. By timing the signal from an object the stability of physical processes, or their regularity, can be probed. Atmospheric Cerenkov astronomy, detailed in chapter 2, has moved from a fledgling field that struggled against a seemingly overwhelming source of background radiation; through a difficult adolescence that saw sources appear sporadically on the basis of timing analyses only to disappear again with the advent of the imaging technique; and is now hopefully beginning to find maturity with the advent of the third generation of detectors that will be able to provide accurate enough spectral information to truly begin understanding the high end of the non-thermal universe.

1.1.1 The thermal universe vs the non-thermal universe

A source of electromagnetic radiation can be characterised according to one of three types of emission: spectra of characteristic lines at specific frequencies; the broader emission of a blackbody curve that is a trait of material in thermal equilibrium with its surroundings;

or a power law indicative of the acceleration of charged particles by external forces. The shape and features of a spectrum can tell a lot about the host environment. The characteristic lines of atomic spectra provide information on the composition of a source, with any Doppler shift or broadening of the line providing information on source motion. Blackbody curves cover a large range of the spectrum: from the cold of the 2.7 K cosmic microwave background through the infra-red outpourings of molecular clouds involved in star formation and the optical light from the stars themselves to the extreme temperatures that are generated in accretion discs formed around compact objects; where the potential energy released from the viscous flow of falling down the potential well of these objects heats matter to such high temperatures that the blackbody curve peaks in the ultra-violet to X-ray waveband. A blackbody curve tells of a medium in equilibrium with its surroundings. There are not just thermal processes at work in the universe, however. The power law spectrum characteristic of non-thermal radiation tells a story of material out of equilibrium with its surroundings, tells of acceleration occuring, it tells of highly energetic processes, sometimes within the most extreme environments imaginable. Much of this view of the universe lay hidden, however, as the photons generated in these sources often lay outside the optical wavelengths. It was not until astronomy opened out from the optical waveband that a full picture of the universe could be seen.

The optical depth of the atmosphere means there are only a few windows for directly observable astronomy from the ground. The optical regime dictated the world view of the universe for a long time, showing a universe of stars and little else. Radio astronomy, in its infancy, had been expected to be of little value: in blackbody terms the radio regime is a very cold place. A few molecular emission lines superimposed on low temperature blackbody curves from giant molecular clouds and stellar nurseries was the best that could be expected as the temperatures of stars means radiation falls off rapidly below the infra-red. Instead, emission from a wide range of astrophysical objects was discovered and a lot of them did not have the spectral slope associated with blackbody emission. This non-thermal emission had a similar spectrum to emission from electrons in synchrotron particle accelerators - the radio regime was actually probing the acceleration of charged particles in hot and relativistic plasmas. With the advent of X-ray and γ-ray astronomy from balloon flights, rocket soundings and satellite experiments more and more of the extreme environments in the universe began to be discovered. The widening of the scope of the electromagnetic spectrum that astronomical observations probe has brought many new insights. Some of these insights are serendipitous discoveries through the application

of new technologies. The discovery of the cosmic microwave background radiation, that is such an integral part of the big bang cosmological theory, is one such instance. This was from a background noise to radio astronomy observations that were being made from an antenna originally designed for sending radio signals long distances, which had been made obsolete by the advent of satellite transmissions. The motivation for monitoring new wavelength regions has also come from observations made at other wavelengths, sometimes just to see where the spectrum ends; or they can be to look for insights into other phenomena, for it is not only electromagnetic radiation that arrives at the Earth.

1.1.2 Cosmic radiation

Cosmic-rays are ionised, highly energetic nuclei, overwhelmingly consisting of single protons, but with representatives of most of the stable elements. Cosmic-rays now have a long history, going from a turn of the century (19th to 20th, that is) mystery as to the origin of the discharge of a gold-leaf electroscope; the Hess and Kolhörster balloon flights that proved they were of extra-terrestrial origin; and cosmic-rays were of invaluable use to the fledgling particle physics community and still contain a component accelerated to higher energies than any human engineered particle accelerator. The cosmic ray spectrum is a power law of differential slope in the range -2.5 to -2.7 up to energies of $\sim 10^{14}\,\mathrm{eV}$ where there is a break referred to as the 'knee' with an exponent of $\simeq 3$ [65]. These parts of the spectrum can be modelled by assuming Fermi acceleration from supernova remnants [12, 13, 66], although conclusive proof has yet to be obtained of this: the charged nature of cosmic-rays means their direction of origin becomes obscured by the galactic magnetic field and so can not be traced back to source. Very high energy γ-radiation generated in collisions sustained by cosmic-rays during their acceleration to high energies in a dense medium could be used to solve the mystery of the origin of comic-rays once and for all, provided that cosmic-rays are accelerated in a medium of convenient enough density of course. At the highest energies ($E > 10^{19}\,\mathrm{eV}$) there is another break in the cosmic-ray spectrum. At these energies cosmic-ray protons would suffer little deflection and could point back to their source, which due to energy considerations would have to be extra-galactic in origin [44], but would have a limited distance due to interaction with the cosmic microwave background; in contrast, however, the Larmor radius for iron nuclei is roughly the distance from the sun to the centre of the galaxy and if the highest energy cosmic-rays were composed of iron they could be galactic in origin.

Whilst it can be said that the charged component of cosmic-rays and the highest

energy photons can be seen to have an intimate connection, for the purposes of this work a distinction will be maintained between electromagnetic (photons) and hadronic (cosmic-ray) matter.

1.2 Energy loss processes

It is from the energy losses of highly energetic particles that we come to understand the processes that can accelerate particles to such high energies in the first place. It is the characteristic energy losses of charged particles that generate the electromagnetic radiation that points back to the non-thermal radiation sources. By examining the timescales and spectral characteristics of the generated radiation it is possible to determine the processes at work in a source and provide constraints to theoretical models. It is through understanding the energy loss processes that detectors and telescopes are constructed in order to probe the flux of radiation arriving at the Earth that tell of the conditions in the acceleration region so far away. As such, we shall explore the energy loss processes before moving on to seeing how high energy photons can be generated in an astrophysical source and then looking at the kinds of detectors employed to probe this radiation.

1.2.1 Interactions of photons with matter

There are three main processes that contribute to the energy loss curve for photons in matter, given in figure 1.1. At low energies (below 1 MeV) the photoelectric effect is dominant; for intermediate energies (0.1 to 10 MeV approximately) Compton scattering is considered; and at high energies ($E > 10\,\mathrm{MeV}$) pair production is king.

The photoelectric effect

In this process a low energy photon is absorbed by an electron bound in orbit around an atomic nucleus. The electron is subsequently emitted from the atom. This process is important for high Z atoms as the cross-section for interaction is proportional to $\sigma_{\mathrm{pe}} \propto Z^5\, E^{-3.5}$, where Z is the atomic number. The cross-section for the photoelectric effect has characteristic edges which occur whenever the incoming photon has just enough energy to make electrons overcome the binding energy of the next atomic electron shell. If the emitted electron is from one of the inner shells then one of the outer electrons will drop down emitting a fluorescence X-ray of energy characteristic to the atomic transition.

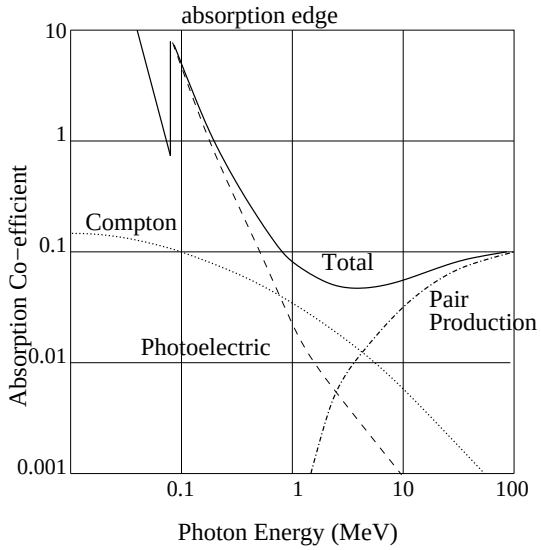

Figure 1.1: The photon absorption cross-section ($\mathrm{cm^2 g^{-1}}$) in lead as a function of photon energy. At low energies the photoelectric effect (dashed line) is the dominant process; at intermediate energies it is the Compton effect (dotted line); and at high energies it is that of pair production (dash-dot line). After [33].

Compton scattering

Akin to the photoelectric effect, but this time the electron can be considered to be free. A high energy photon collides with a stationary electron and imparts momentum to this electron which is scattered off at an angle to the photon. The value of this scattering angle is related to the change in momentum (and consequently change in wavelength) of the photon. As the electron is considered to be free this effect becomes important once energies become greater than $\sim 100\,\mathrm{keV}$, below which the effects of binding of the electron to the nucleus can be important. The cross section for Compton scattering can be approximated by the following [33]

$$\sigma_{\mathrm{cs}} \sim \frac{Z}{h\nu},$$

where h is Planck's constant and ν is the frequency of the photon. Compton scattering generally dominates energy deposition in the 0.1 to 10 MeV region.

The inverse Compton effect can be an important process for generating high energy photons. This is when a high energy electron collides with a low energy photon, imparting energy and boosting the photon up the energy ladder.

Pair production

Once a photon has an energy equal to twice the electron rest mass it can pair produce when interacting with an electromagnetic field, such as in the field of a nucleus. The incoming photon is absorbed in an ambient medium and its energy is converted to an electron-positron pair.

$$\gamma + A \rightarrow A + e^+ + e^-$$

This process *must* be an interaction in order to absorb some of the momentum of the photon: a zero mass particle spontaneously decaying in to non-zero mass particles in a vacuum would violate mass-energy conservation.

The pair production cross-section essentially scales as $\sigma_{\mathrm{pp}} \propto Z^2$. The cross-section rises rapidly from threshold and essentially dominates all energy-loss mechanisms for photon energies $E_\gamma \geq 10\,\mathrm{MeV}$. At energies $E_\gamma > 100\,\mathrm{MeV}$ the cross-section saturates and can be characterised by a mean free path for conversion (constant absorption coefficient) that is essentially equal to the electron radiation length of the medium (see section 2.3.1), this reflects the similarity of the two processes from a QED perspective.

1.2.2 Interaction of charged particles with matter

There are two main mechanisms for charged particles to lose energy within a medium: by ionisation and via bremsstrahlung. An impression of the energy loss curve is given in figure 1.2. Ionisation losses dominate the low energy region of the curve, with a characteristic minimum when $E \sim 3mc^2$; after this minimum the losses due to ionisation scale logarithmically, whereas bremsstrahlung goes linearly with energy. The point at which energy losses due to bremsstrahlung equal those due to ionisation is defined as the critical energy E_c, an energy important in the modelling of extensive air showers, which are met in chapter 2.3.

Ionisation

Ionisation is the process of a free charged particle giving energy to the atomic electrons of a medium. The energy loss rate due to ionisation, including relativistic effects, is described by the Bethe-Bloch equation

$$-\frac{\mathrm{d}E}{\mathrm{d}X} = \frac{4\pi N_a z^2 e^4}{\beta^2 mc^2}\frac{Z}{A}\left[\ln\left(\frac{2mc^2}{I}(\beta\gamma^2)\right) - \beta^2\right] \tag{1.1}$$

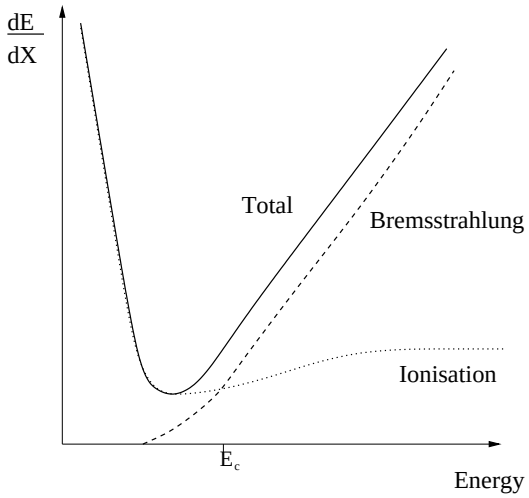

Figure 1.2: Energy loss due to a charged particle traversing matter. At low energies ionisation is the dominant energy loss process (dotted line): at high energies bremsstrahlung (dashed line) dominates. The point where the loss processes are equivalent is called the critical energy, E_c. The minimum in the curve approximately coincides with $E \sim 3mc^2$. After [33].

where X is the path length in $\mathrm{g\,cm^{-2}}$, m is the electron mass, e is the electron charge, z the particle charge, Z the atomic number of the absorbing medium, A the atomic mass of the absorbing medium, I is the effective ionisation potential ($I(z) \approx Z \times 13\,\mathrm{eV}$); N_a is Avogadro's number; $\beta = v/c$; and $\gamma = 1/\sqrt{1-\beta^2}$ is the Lorentz factor. The ionisation energy loss rate reaches a minimum value of $\approx 1\,\mathrm{MeV\,g\,cm^{-2}}$ when $\beta\gamma \approx 3$. Energy loss processes due to acceleration, particularly for lighter particles like electrons, come to dominate over ionisation as a particle's energy increases.

Bremsstrahlung

A charged particle moving in an electromagnetic field will be deflected and the acceleration due to the change in direction will lead to the radiation of electromagnetic energy

$$P = \frac{\mathrm{d}E}{\mathrm{d}t} = \frac{q^2a^2}{6\pi\epsilon c^3} \tag{1.2}$$

where P is the radiated power, q is the charge of the particle and a is the acceleration of the particle. When a charged particle is accelerated by an electric field, such as the nuclear Coulomb field, this radiation is known as bremsstrahlung, from the German for 'braking radiation'. The rate of energy loss by bremsstrahlung is inversely proportional to the square of the mass of the accelerated particle, i.e. for an electron it is $\sim 10^4$ times

that for a muon and $\sim 10^6$ times higher than that of a proton. The ratio of energy loss due to bremsstrahlung to the losses due to ionisation can be approximated [33] by the equation

$$\left(\frac{\mathrm{d}E}{\mathrm{d}X}\right)_{brem} / \left(\frac{\mathrm{d}E}{\mathrm{d}X}\right)_{ion} \approx \frac{EZ}{1200mc^2} \tag{1.3}$$

where m is the mass of the particle. The critical energy for an electron then works out as $\sim 85\,\mathrm{MeV}$ and for a muon it is $\sim 18\,\mathrm{GeV}$. It can then be seen that electrons, being not very massive particles, will suffer severe bremsstrahlung losses at energies where a more massive particle such as a proton will barely radiate anything at all.

1.3 The generation of high energy photons in astrophysical sources

High energy photons are generated from the energy losses sustained by a parent population of even more energetic particles. Processes involving electrons are usually due to the acceleration of the electron population, whereas processes involving hadronic matter are usually down to direct collisions. A good review of the radiation produced by the acceleration of a population of relativistic electrons can be found in [16]. Photons can also be produced by the annihilation of a matter/anti-matter pair, such as the 511 keV photons produced from $e^{\pm}$ annihilation. One of the postulated methods for detecting dark matter is through annihilation line radiation in the unprobed region of 50 to 300 GeV photons [14]. Figure 1.3 gives a pictorial representation of the processes in the following discussion.

1.3.1 Bremsstrahlung

The slope of the spectrum for bremsstrahlung is the same as the underlying electron spectrum because the intensity of photons is flat up to the maximum energy an electron can lose : $h\nu_{max} = (\gamma - 1)mc^2$ [65] (see figure 1.4). This means that the spectrum may be Maxwellian if the underlying electron population has a thermal origin to the velocity distribution (in the non-relativistic case) or a power law form if other acceleration processes are going on (as necessary for a relativistic population of electrons).

1.3.2 Synchrotron radiation

When a charged particle moves with a component of its momentum perpendicular to a magnetic field it is deflected, experiencing a centripetal force causing it to move in a circle

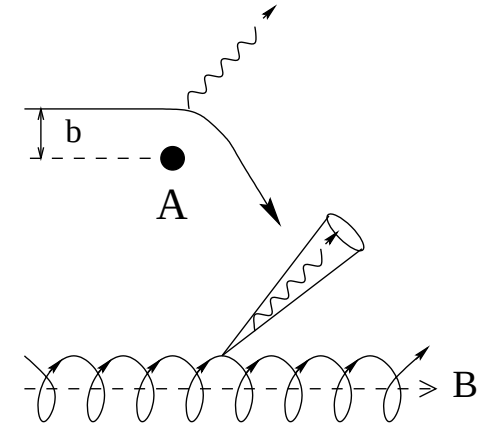

bremmsstrahlung

synchrotron radiation

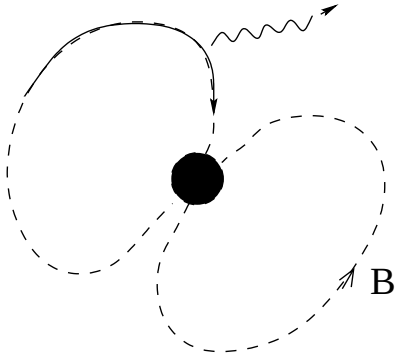

curvature radiation

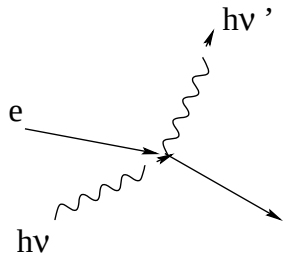

inverse Compton effect

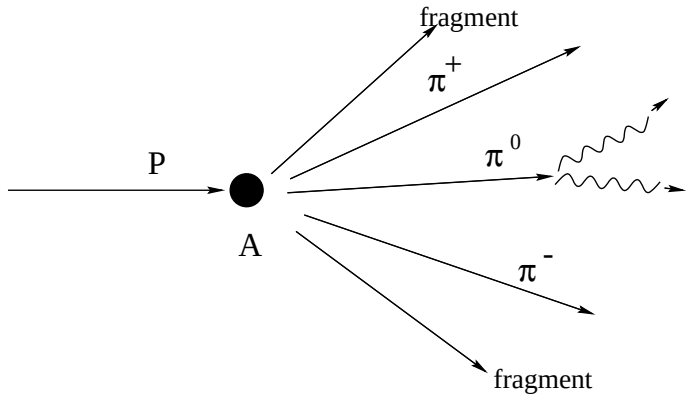

pion decay

Figure 1.3: Processes for producing high energy photons.

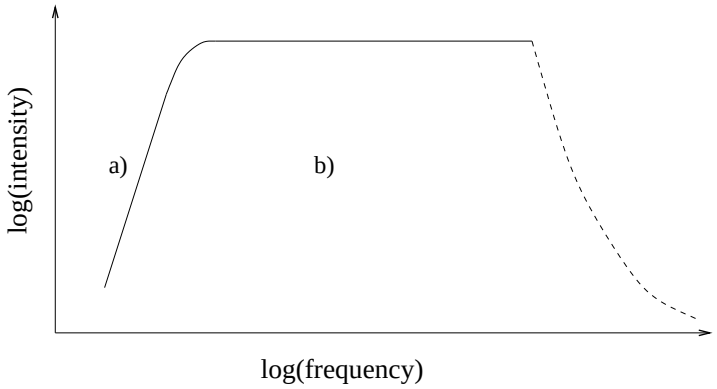

Figure 1.4: Schematic of the bremsstrahlung spectrum. Region a) corresponds to the self-absorbed region with a spectral slope $\propto \nu^2$. Region b) has a $\sim$ constant slope after the turnover region which marks when the optical depth is ~ 1. The dashed line marks the exponential cut-off, denoting the sharp break for the maximum energy a photon can lose.

perpendicular to both the magnetic field and the velocity component in the direction of the field. The particle effectively spirals around the magnetic field line. As we have already seen in the case of bremsstrahlung, whenever a charged particle is accelerated it consequently radiates electromagnetic energy (equation 1.2). The acceleration in the case of motion through a magnetic field is given by

$$a = \frac{v^2}{r} = \frac{e}{\gamma m}\mathbf{v} \times \mathbf{B}$$

where $\mathbf{v}$ is the velocity of the charged particle, γ the Lorentz factor and $\mathbf{B}$ the magnetic field acting on the charged particle. As the power radiated is $\propto 1/m^2$ we see that energy losses for electrons are more than 10^6 times those for protons. This is one of the reasons for the dearth of cosmic-ray electrons reaching Earth, they have radiated most of their energy before they have had a chance to arrive. For a population of particles with sub-relativistic speeds this radiation is called cyclotron radiation and for a parent population with relativistic velocities it is called synchrotron radiation. The characteristic frequency of the cyclotron radiation is simply the gyration frequency

$$\nu_g = \frac{qB}{2\pi m}.$$

The energy of this radiation is several orders of magnitude lower than the parent particle population which, as they are sub-relativistic, is of no interest to us.

In the relativistic limit the mass is γm and the characteristic frequency is ν_g/γ, i.e.

lower than the non-relativistic case and now dependent on energy. For synchrotron radiation the radiation is compressed into a small opening angle of size $\sim 1/\gamma$ around the instantaneous velocity vector of the particle, a process know as 'beaming', which results in a spreading of the energy spectrum that depends on the momenta of the particles. Synchrotron spectra typically have a power law shape, reflecting the power law spectra of the underlying charged particle population. A schematic of the synchrotron spectrum is given in figure 1.5. When the energy density in the synchrotron spectrum is high the electrons absorb some of the radiation giving rise to region a) in figure 1.5 which has a characteristic slope of $+5/2$. There is then a turnover region when the brightness temperature of the radiation is $\simeq$ kinetic temperature of the electron population. Region b) of figure 1.5 has a characteristic slope of ν^{α}, if the electrons have a power law spectrum like

$$N(E) = kE^{-x}$$

where k is some constant, $N(E)$ are the number of electrons of energy E and x is the spectral slope then the power radiated in synchrotron radiation, $P(\nu)$, will go as

$$P(\nu) \propto \nu^{-\frac{x-1}{2}}$$

therefore $\alpha = \frac{x-1}{2}$, can be used to give information on the spectrum of the underlying electron population.

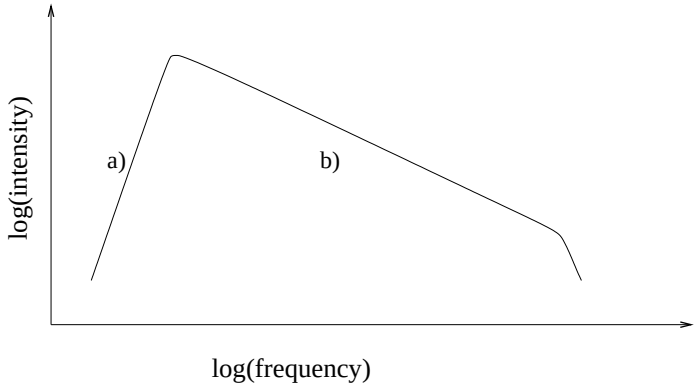

Figure 1.5: Schematic of the synchrotron radiation spectrum. Region a) corresponds to the self-absorbed region with a spectral slope of 5/2. Region b) corresponds to the optically thin emission region of slope α.

Synchrotron radiation is several orders of magnitude down in energy from the population of relativistic electrons generating it: it is presumed responsible for much of the

radio emission in the universe, but can go up to the X-ray. This means it is not of much interest to us on its own, but as a process it can generate a seed photon field for the inverse Compton scattering of photons to very high energies.

1.3.3 Curvature radiation

A close cousin of synchrotron radiation, this is the resultant electromagnetic radiation when a charged particle follows a curved magnetic field line. Where synchrotron radiation is a result of the motion of a charged particle to a perpendicular magnetic field, curvature radiation is the result of the charged particle following a magnetic field that deviates from a straight line. As the charged particle experiences an acceleration by following the curved trajectory electromagnetic radiation is given out. The environment needed for this type of radiation is one of an intense magnetic field ($> 10^8$ G) with extreme curvature, such as in a pulsar magnetosphere.

1.3.4 The inverse Compton effect

This is merely the Compton effect seen from a different perspective: a high energy electron transfers some to all of its momentum to a low energy photon. The exact cross-section for this process is dependent on the relative energies of the photon field and the scattering electron. If $\gamma\hbar\omega \ll m_e c^2$ then the Thompson scattering cross-section can be used (simplifying calculations no end), if not then the quantum relativistic cross-section provided by the Klein-Nishina formula [65] must be used, which tends to decrease the interaction cross-section for increasing energy. Taking the simple picture it can be shown [65] that the frequency of photons upscattered by ultra-relativistic photons is $\nu \approx \gamma^2 \nu_0$, where ν_0 is the frequency of the photon before scattering. To produce a TeV photon an electron with a Lorentz factor of $\gamma \approx 1000$ would need a seed photon field of X-rays with energies in the hundreds of keV, such as would be found in an X-ray binary or an active galactic nucleus.

The inverse Compton spectrum is a complex function of the primary electron spectrum and of the ambient photon energy density, so is a non-trivial function to calculate. Figure 1.6 gives a schematic of the inverse Compton emission spectrum for an incident isotropic photon field at a single frequency ν_0, following the scheme of [65], taking the calculations of [16]. The important feature to note from this diagram is that the maximum photon energy is due to a head on collision and corresponds to a new frequency of $\nu_{\max} = 4\gamma^2\nu_0$, where γ is the Lorentz factor and ν_0 is the frequency of the unscattered

photon.

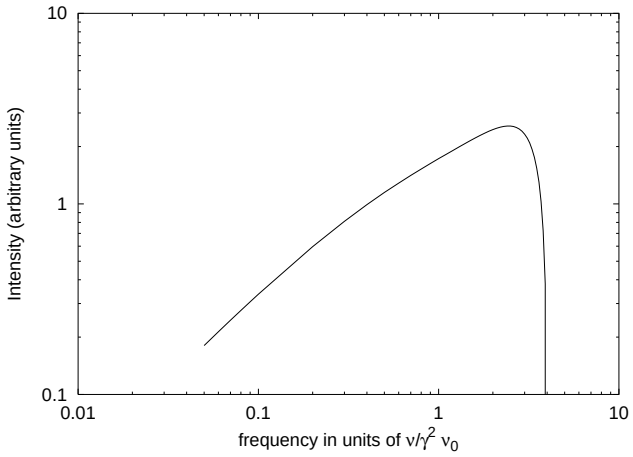

Figure 1.6: The emission spectrum due to the inverse Compton scattering of an isotropic monochromatic photon field; ν_0 corresponds to the frequency of the unscattered radiation. Following the scheme of [65]

1.3.5 Neutral pion decay

The previous methods for the generation of high energy γ-rays have mostly concentrated on processes involving electrons. This is because the cross-section for processes involving the acceleration of charged particles have a mass dependence; electrons, being less massive particles, are accelerated more easily and so come to dominate these processes. Hadronic material is more likely to create high energy photons due to direct interactions with an ambient medium. Collisions between high energy nucleons generate pions. These come in three variants and are generated in roughly equal numbers: the neutral π^0 and the charged $\pi^{\pm}$. It is the neutral π^0 which decays rapidly into two photons that would be responsible for generating a flux of high energy γ-rays. These γ-rays would be useful in identifying the sites of cosmic-ray acceleration; as the paths of the charged cosmic-rays are deflected by the galactic magnetic field they no longer point back to the source, but photons being neutral particles do not suffer these digressions from a straight line. Pion production is a feature of the interaction of high energy cosmic-rays when they enter the atmosphere, but more will be said in chapter 2.3 on that matter.

1.4 The attenuation of VHE photons from astrophysical sources

The attenuation of VHE photons from astrophysical sources is down to pair production, as this process has the dominant cross-section for photons with energies over $\sim 1\,\mathrm{MeV}$ (see figure 1.1). As stated earlier, the spontaneous decay of a single photon to an electron/positron pair is forbidden due to energy/momentum conservation considerations. The loss of photons due to pair production then depends on something being there to interact with.

1.4.1 Pair production from interactions with the ambient medium

The radiation length is the distance travelled to lose all but 1/e energy. For a 1 TeV photon this corresponds to a column density of about $\sim 37\,\mathrm{g\,cm^{-2}}$ [79]. The Earth's atmosphere is over a $1000\,\mathrm{g\,cm^{-2}}$ by sea level, which is nice from the viewpoint of not being bombarded with TeV photons, but means that VHE γ-ray astronomy has to exploit indirect methods to detect TeV photons from the ground. The column density to the centre of the galaxy from the Earth, assuming the average density is 1 hydrogen atom per cubic centimetre and a distance of 8.5 kpc, is about $0.04\,\mathrm{g\,cm^{-2}}$. As we can see, there is very little attenuation of VHE photons on interstellar (or intergalactic) matter. The amount of matter within an accreting system, however, can place a restriction on the production site of observable TeV emission.

1.4.2 Photon photon pair production

Mimicking a reverse electron-positron annihilation is photon-photon pair production. The threshold energy for this process is found from [65]

$$E_2 = \frac{2m^2c^4}{E_1(1-\cos\theta)} \tag{1.4}$$

where E_1 and E_2 are the energies of the respective photons and θ is the angle between them. The threshold for the process occurs for a head on collision ($\theta = \pi$), which happens when $E_1E_2 \geq 0.26 \times 10^{12}\,\mathrm{eV}^2$. Table 1.1 gives values for the kind of photon fields that VHE γ-rays could meet in their travels, column 2 giving the energies associated with those photons and column 3 giving the threshold energy needed for a VHE photon to pair produce. The observable aspects of VHE γ-rays can provide important insights to astrophysical problems. The spectrum of γ-rays from extra-galactic objects can tell of

the distribution of the infra-red background, important to star formation models. The signature of orbital modulation (or lack thereof) can provide information about the site of VHE γ-ray production in X-ray binaries (see chapter 5 for more information).

	E_1 (eV)	E_2 (eV)
Microwave background	6×10^{-4}	4×10^{14}
Starlight	2	10^{11}
X-ray	10^3	10^8

Table 1.1: Threshold energies for photon-photon pair production. From [65].

In a strong magnetic field a VHE photon can pair produce from a virtual photon. A field strength component of $> 10^6$ G perpendicular to the photon's momentum is needed for this process to occur [94]. This only really becomes important when looking at the proximity of a source of VHE γ-rays to a neutron star.

1.5 Observing energetic radiation

The energy loss processes described earlier dictate the design of instruments used for observing high energy radiation, or perhaps more accurately it is the design of the instrument that dictates which energy ranges the instrument is sensitive to, by allowing particular energy loss processes to give recordable information. The atmosphere is opaque to much of the electromagnetic spectrum: radiation outside of the visible, a few infra-red bands and the radio regime will not penetrate to ground level. X-rays are attenuated by photo-electric absorption with the atoms and molecules of the atmosphere and the γ-rays suffer from the higher energy loss processes detailed earlier in the chapter. In order to directly detect radiation from the higher energy processes it becomes necessary for instruments to be located above the atmosphere and exploiting the very energy loss processes that prevent the photons reaching the ground in the first place.

1.5.1 Going above the atmosphere

The very early days of X-ray and γ-ray astronomy saw sources being detected through rocket soundings and high altitude balloon flights. These provided only short observation times, but even they were enough to demonstrate that there was a rich source of objects in the universe at these wavelengths. The fields of X-ray and γ-ray astronomy really took off

when satellites in stable orbits were able to take long exposure observations and provide long term monitoring of time varying phenomena. There have been numerous satellites launched to examine the sky in the X-ray and low to high energy γ-ray regime (10's of keV up to 10's of GeV), far too many to summarise here, I direct the interested reader to the historical introduction of [65] instead. Data from the EGRET [100], BATSE [81], RXTE [96] and GINGA [74] instruments have been invaluable to this work. It is sufficient to say that the presence of these satellites have made many fascinating discoveries from X-ray binaries to γ-ray bursts; from X-ray emission in the rarefied intergalactic medium, to that from the accreted material falling on to the most compact objects imaginable. Satellites have provided an invaluable insight into the universe, but they do also have shortcomings. As the energy of photons increases so their flux decreases; a γ-ray satellite like EGRET had an effective area of $700\,\mathrm{cm}^{-2}$ at $10\,\mathrm{GeV}$ [100] and would be lucky to see 6 photons a day at that energy from an object. It is very difficult to do useful astronomy on that level of flux.

Fortuitously, we will see in the next chapter that whilst the atmosphere prevents the direct observation of high energy radiation, it can be utilised as a detector of large effective area at very high energies. These ground based observations can then provide complementary data to satellite observations, and vice versa, about the highest energy processes in the universe.

1.6 Summary

This chapter has dealt with the acceleration of particles and how energy loss processes place limits on the amount of energy a particle can gain. The high energy electromagnetic radiation produced from these energy losses can be indicative of the processes at work in an astrophysical object. By utilising how photons lose energy, instruments can be designed for the detection of high energy photons, allowing useful astronomy to be done. The atmosphere, however, is an effective absorber of high energy radiation, prompting the need for satellite based observations of many sources of non-thermal radiation. In the next chapter we will see how radiation of sufficiently high energy can be detected indirectly through the exploitation of secondary light emission, produced as a consequence of the interactions of the high energy primary particles with atmospheric nuclei.

Chapter 2

Imaging atmospheric Cerenkov astronomy

2.1 Introduction

The previous chapter summarised the interaction processes available to energetic radiation and told how the atmosphere is a very efficient absorber of the high energy emission from astrophysical sources, preventing the direct detection of X-rays and γ-rays. Satellites became necessary in order to probe sources of non-thermal emission from astrophysical objects, but suffer from the problem of being expensive and having only a small effective collection area for very high energy photons. This chapter details how the atmosphere can once again become useful as a detector through the generation of light, known as Cerenkov radiation, from the secondary products created by the attenuation of the high energy primary flux in the first place. We will go on to see how this Cerenkov radiation can give a ground based detector a large effective collection area for VHE photons, thereby allowing useful astronomical observations to be made, and will summarise some of the telescopes that have capitalised on this branch of astronomy.

2.2 Cerenkov radiation

The faint emission of a bluish-white light from transparent substances in the vicinity of strong radioactive sources had been observed by many workers in the field of radioactivity before Frank and Tamm provided a theoretical treatment in 1937, with Ginzberg subsequently adding a quantum mechanical treatment and naming the effect Cerenkov radiation, after the exhaustive series of experiments by Cherenkov into the effect from

1934-1938. Much has been written of the history of the discovery, so I direct the interested reader to [52] and references therein. The best way to get an image of the effect in action is to picture the blue glow from the deep water pools surrounding nuclear reactors operating at high power that so often appear as publicity photos from the nuclear power stations.

2.2.1 The effect

Figure 2.1 shows the effects of a charged particle passing through a dielectric medium. The transition of the charged particle appears to the atoms of the medium as a time varying electric field. The atomic electrons will become displaced to one side of the heavier nuclei in response to this field - polarising in the direction of the charged particle. At low velocity ($v < c$) there is a complete symmetry of the polarization field surrounding the charged particle, as in figure 2.1(a). If, however, the velocity of the charged particle through the medium exceeds the phase velocity of light for that medium, as in figure 2.1(b), then no electromagnetic information can be passed on to atoms ahead of the traversing particle: whilst azimuthal symmetry is maintained it is broken along the axis of motion. Each elemental region of the track will give off a brief electromagnetic pulse as the electrons return to stable orbits, demonstrated in figure 2.2. In the case of a low velocity ($v < c$) particle, shown in figure 2.2(a), the pulses will destructively interfere, meaning there can be no resulting field at large distance and so no radiation will be produced. For the high velocity case ($v > c$, part b of figure 2.2) when the electrons in the atoms radiate their pulses it is possible for the wavelets generated along the track to be in phase, they constructively interfere and the resultant net field can seen at a distance. Figure 2.3 is a Huygens construction showing how the coherent emission arises when $v > c$. This figure also demonstrates how the radiation is only observed at a particular angle with respect to the track of the particle. The wavefront from arbitrary points p_i along the track AB combine to form a plane wave front BC. This coherence takes place when the particle travels from A to B in the same time it takes the light to travel from A to C. If the velocity of the particle is βc and the velocity of light in the medium is c/n then in a time Δt the particle will travel a distance AB $= \beta c \Delta t$ and the light a distance AC $= (c/n)\Delta t$. The opening angle for the cone of Cerenkov radiation is then just

$$\cos(\theta) = \frac{1}{\beta n} \tag{2.1}$$

From this simple relation many things can be gleaned

- for a medium of given refractive index n there is a threshold velocity ($v/c = \beta = 1/n$) below which no radiation takes place.
- There is a maximum angle of emission, $\theta = \cos^{-1}(1/n)$ which occurs when $\beta = 1$.
- The radiation occurs mainly in the visible and near visible regions of the spectrum, for which $n > 1$. Emission in the X-ray regime is impossible as $n < 1$.

It is possible to calculate the number of photons that are generated per unit path length between wavelengths λ_1 and λ_2 [15]

$$\frac{\mathrm{d}N}{\mathrm{d}x} = 2\pi\alpha z^2 \int_{\lambda_1}^{\lambda_2} \left(1 - \frac{1}{(\beta n(\lambda))^2}\frac{1}{\lambda^2}.\mathrm{d}\lambda\right) \tag{2.2}$$

with α being the fine structure constant ($\approx 1/137$) and z being the particle charge.

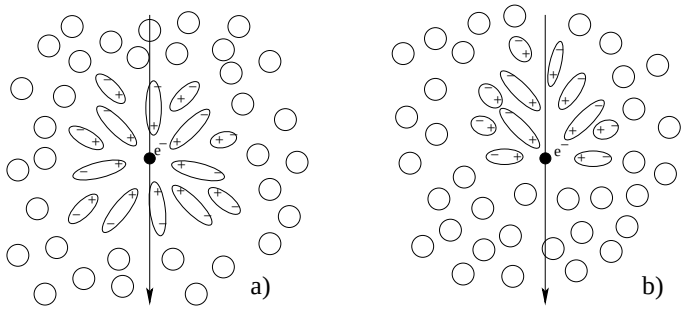

Figure 2.1: The polarisation set up in a dielectric medium by the passage of a charged particle when a) $v < c$ and b) $v > c$. Adapted from [52].

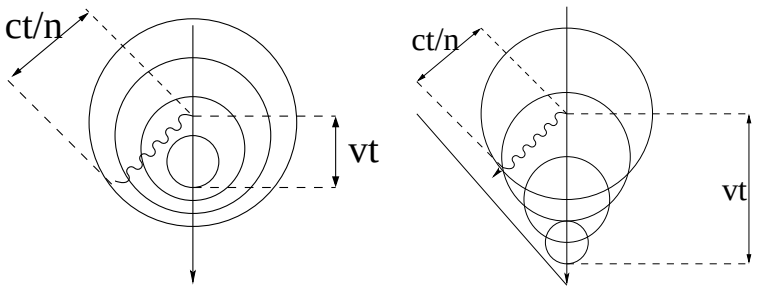

(a) $v < c$ (b) $v > c$

Figure 2.2: The interference between wavefronts centred on the passage of a charged particle through a dielectric. The interference is (a) destructive when $v < c$ and (b) constructive when $v > c$.

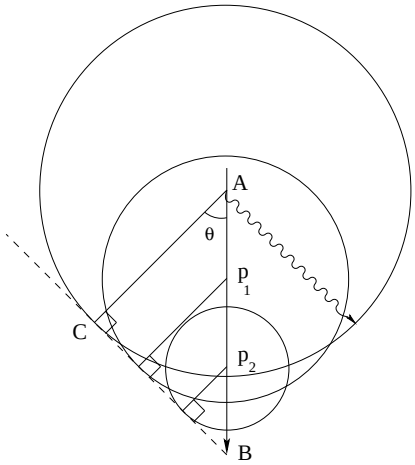

Figure 2.3: Huygens construction illustrating the coherence and emission angle for Cerenkov light.

The generation of Cerenkov light is analogous to the 'sonic boom' V-shaped shock wave produced when travelling through the air at speeds greater than the speed of sound; or perhaps a better visualisation is that of the bow wave from a ship moving through water faster than the speed of the surface waves.

2.2.2 The atmosphere as a Cerenkov medium

Blackett first suggested in 1948 that there should be a small contribution to the light of the night sky from Cerenkov radiation, of the order $\sim 10^{-4}$ of the total night sky light. Such a small intensity of light is not easily detectable, but by picking out momentary bursts of light against the night sky background using photomultiplier tubes and fast electronics Galbraith and Jelley in 1953 [52] were able to correlate Cerenkov light with large cosmic-ray showers and a new astronomy was born.

The index of refraction for air is small compared to that of solids and liquids like water and glass. This means that the threshold energy a particle needs to generate Cerenkov radiation is higher, the light intensity is much lower and the emission angle smaller. The atmosphere is still a viable emission medium for Cerenkov radiation. Taking a standard value of the refractive index for air at sea level as $n = 1.00029$ at standard temperature and pressure (STP) we see that the threshold energy for Cerenkov emission by electrons in air is $\sim 21\,\mathrm{MeV}$ with an opening angle of 1.38°. All that is necessary now is for a process to create a population of relativistic charged particles in sufficient numbers to generate a detectable amount of Cerenkov light.

2.3 Extensive air showers

The generation of Cerenkov light requires the presence of highly relativistic particles travelling faster than the speed of light in a medium. The impact of very high energy radiation on the upper atmosphere can provide that population of relativistic particles, allowing us to probe some of the highest energy physical processes from the relative comfort of the ground. Through energy losses a very high energy primary particle can share that energy into a large number of merely high energy secondary particles. An extensive air shower (EAS) is a cascade of sub-atomic particles passing through the atmosphere. They are generated by either of two mechanisms: an electromagnetic based shower due to the interaction of high energy photons and electrons; or hadronic based ones due to the interactions of the heavy nuclei component of cosmic-rays. The distinguishing features of both of these forms of air showers are discussed further below.

2.3.1 γ-ray initiated showers: electromagnetic based showers

When a photon has $> 1\,\mathrm{MeV}$ of energy it is able to produce an $e^{\pm}$ (electron/positron) pair when it interacts with the electromagnetic field of a target nucleus. As a γ-ray enters the atmosphere a lot of target nuclei present themselves (the mean interaction length for a $1\,\mathrm{TeV}$ photon is $\sim 37\,\mathrm{g\,cm^{-2}}$ [79] and the atmosphere corresponds to $\simeq 26$ radiation lengths upon reaching sea level from space). This $e^{\pm}$ pair will then radiate bremsstrahlung photons, which, provided they are of sufficient energy, will in turn create more $e^{\pm}$ pairs and so on producing a cascade of charged particles travelling through the atmosphere at relativistic speeds. This process can not continue indefinitely, at each interaction the energy imparted by the initial photon becomes spread over a greater number of particles. Once the energy of an electron drops below the critical energy the energy losses due to ionisation over take the energy losses due to bremsstrahlung. Once this threshold is reached ($\sim 84\,\mathrm{MeV}$ for an electron in air) the air shower dies off quickly.

The propogation of an electromagnetic air shower can be simply approximated according to the following system. In this discussion the radiation length x_0 is the distance travelled to lose all but 1/e energy and the interaction length is the distance travelled whereby $\exp(-x/x_0) = 1/2$. Considering only the pair production and bremsstrahlung components (with both having similar interaction lengths due to their similarity from a QED perspective) by an atmospheric depth corresponding to n interaction lengths each primary will have produced 2^n secondary particles with the energy of the initial particle

(E_0) having been shared out among the secondaries such that

$$\langle E \rangle = \frac{E_0}{2^n}$$

where $\langle E \rangle$ is the average energy of a secondary particle. It is then possible to calculate the penetration depth of the shower maximum in terms of the primary energy E_0, the interaction length x_0 and the critical energy E_c

$$x_{\max} = x_0 \ln\left(\frac{E_0}{E_c}\right). \tag{2.3}$$

More sophisticated methodologies also introduce ionisation losses for each interaction length to gain a more accurate reflection of the development of the air shower. From these calculations it is worked out that the height of shower maximum occurs approximately 10 km above sea level for a 1 TeV shower.

2.3.2 Cosmic-ray induced air showers: hadronic based showers

A far more abundant source of air showers is the nucleonic component of cosmic radiation. Composed chiefly of protons, but with representatives of all nuclei, these cosmic-rays outnumber TeV γ-radiation 1000:1. When a nucleon enters the atmosphere it will react with atmospheric nuclei via the strong force. This interaction has a larger path length of $\sim 80\,\mathrm{g\,cm^{-2}}$, when compared to the interaction length for a photon. The offspring of this union is a series of pions, maybe a few kaons and the fragments of the initial interacting particles. Pions come in three varieties: the neutral π^0 and the charged $\pi^{\pm}$. The differing pions are produced in roughly equal numbers (until you get to low energies where charge conservation favours π^+'s) so we see that approximately a third of the primary cosmic-ray energy is deposited to each of the channels. The π^0's quickly decay ($\tau_{1/2} = 0.8 \times 10^{-16}$ s in the rest frame [76]) into 2 γ-rays which proceed to create electromagnetic showers as described earlier. The charged pions can either further interact with atmospheric nuclei or decay themselves ($\tau_{1/2} = 2.6 \times 10^{-8}$ s in the rest frame [76]) into muons and neutrinos. Neutrinos are weakly interacting neutral particles and so need take no further part in our discussion. Whilst muons will then decay into electrons and neutrinos, their velocity is generally such that relativistic time dilation will mean that their 2.2 μs rest frame lifetime will allow a large component of their number to reach sea-level (and below). This can be a useful discriminant for particle detectors by sampling the muon rich content of a cosmic-ray air shower in comparison to that of a γ-ray air shower (cosmic-ray generated muons are higher by $\sim$ an order of magnitude for a 30 TeV primary).

As each hadronic based interaction can create many daughter particles, this kind of air shower can impart a large amount of transverse momentum to the secondary particles of the air shower. This spreads the particles over a much larger lateral distance than in an electromagnetic based shower. This characteristic comes in useful when characterising the observable aspects of the different air showers and differentiating between them.

2.4 Atmospheric Cerenkov radiation

2.4.1 The generation of photons

The index of refraction is the important quantity for Cerenkov radiation. It defines the threshold energy particles need for emission; the angle of emission for the Cerenkov light; and it affects the number of photons generated, as seen in equation 2.2. The index of refraction for air is actually a complex function of pressure, temperature, water vapour content and wavelength [15], but for the purposes of simplification it can be approximated as being proportional to air density. Writing the refractive index as $n = 1 + \eta$ allows us to approximate the change of refractive index with altitude h as

$$\eta(h) = \eta_0 \exp\left(-\frac{h}{H_0}\right) \tag{2.4}$$

where η_0 is the value at ground level and H_0 is the scale height for an exponential atmosphere. Since $n(\lambda) - 1$ varies by only 5% over the wavelength range 300 to 600 nm [15], which is the wavelength range typically covered by PMTs, a wavelength independent index of refraction is another useful simplification that can be made. Assuming a constant index of refraction over the wavelength range for PMTs means that we can write the number of photons generated as a function of distance travelled by the charged particle, equation 2.2, as

$$\frac{\mathrm{d}N}{\mathrm{d}x} = 764 \sin^2(\theta) \text{ photons cm}^{-1}$$

where $z = 1$ as the charged particles under consideration are electrons. The number of photons generated is then sensitive to the Cerenkov emission angle.

Since the index of refraction changes as a function of altitude it can be seen that the angle of Cerenkov emission changes as a function of altitude as well. This affects the distribution of photons within the Cerenkov light pool when it reaches the ground. We can use the relations we have calculated earlier this chapter to calculate the maximum radius of the Cerenkov light pool. Consider a single electron moving vertically in the

atmosphere and neglect any scattering of the electron and any scattering or refraction of the light. The maximum angle for the Cerenkov emission is when $\beta = 1$, therefore

$$\cos(\theta_{\max}) = (1/n) = (1+\eta)^{-1} \approx 1 - \eta$$

by expanding out and approximating for $\cos(\theta)$ we see that

$$\theta_{\max} \approx \sqrt{2\eta}$$

Light generated at a height h with an angle θ will strike the ground at a distance r from where the electron strikes the ground (the impact point)

$$\begin{aligned} r &= h\theta = h \times \sqrt{2\eta(h)} \\ &= \sqrt{2\eta_0} \times h \times \exp\left(-\frac{h}{2H_0}\right) \\ &= kh \exp\left(-\frac{h}{2H_0}\right) \end{aligned}$$

Finding the maximum radius for emission height, $\mathrm{d}r/\mathrm{d}h = 0$, gives $h_{\max} = 2H_0$. Following the scheme of Jelley [52], $H_0 = 7.1\,\mathrm{km}$, the angle of emission is $\simeq 0.5^\circ$ and therefore the maximum radius of the Cerenkov light cone is $\sim 120\,\mathrm{m}$. At this height there are roughly 6 Cerenkov photons being produced per metre travelled. The actual shower maximum, i.e. the point where the number of particles in the shower peaks, is closer to 10 km above sea level; the angle of emission at this height is $\sim 0.7^\circ$ and there are more like 11 Cerenkov photons being emitted per metre travelled for each relativistic charged particle. Scattering of both the emitting particles and the Cerenkov light as well as the change in emission angle with increasing penetration of the atmosphere means that light is spread fairly evenly across the pool, rather than just producing an annulus of light. This change of angle does produce an interesting focusing effect for γ-ray showers which produce much of their light higher up in the atmosphere, demonstrated in figure 2.4. The lateral distribution of light on reaching the ground is characterised as following a central peak connecting to a relatively flat region leading out to a rim at about 120 m, beyond which the light distribution falls off rapidly. The central peak is due to penetrating particles reaching the ground, it becomes less pronounced with decreasing energy and increasing zenith angle as the path length to the observer becomes larger. The rim (or 'shoulder') feature position hardly varies with primary particle energy as it is a feature defined by the refractive index of the atmosphere.

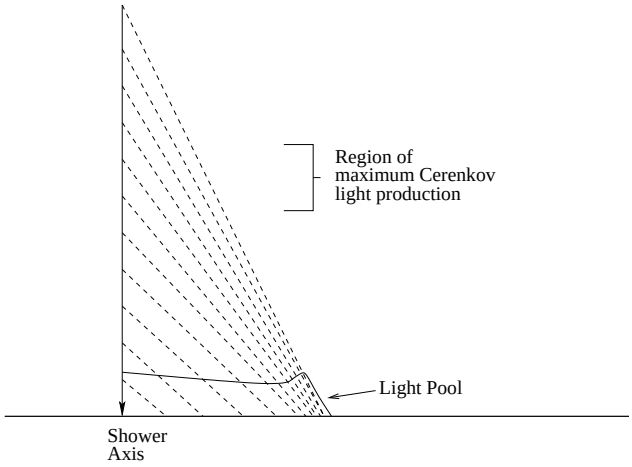

Figure 2.4: The focusing of Cerenkov light emitted from a γ-ray initiated light shower, caused by the change of refractive index with altitude. The individual Cerenkov light cones at each altitude combine to produce a 'shoulder' to the photon density within the light pool. Obviously this diagram is not to scale.

2.4.2 The attenuation of photons

What the atmosphere provides it also taketh away. Some of the Cerenkov photons that are generated in the EAS will also be attenuated by the atmosphere in their journey to the detector. It is important to know the amount of attenuation that the Cerenkov photons experience. There needs to be enough Cerenkov photons to trigger the detector in the first place. The Cerenkov light is also calorimetric, the number of Cerenkov photons is proportional to the number of particles in the air shower, which in turn are related to the energy of the primary particle. If one needs to know the energy of the primary particle it is necessary to know how much light will reach the detector. The attenuation of light is down to two processes: absorption and scattering. Absorption is a loss process, whereby the photons are removed from the medium they are travelling through. Scattering merely changes the path a photon is travelling along, but if that path is changed so the photon goes out of the line of sight it can be considered as lost from an observer's point of view. Multiple scattering can mean the photon re-enters the line of sight, but as the extra distance travelled increases the time taken between the photon's origin and the observer and since the Cerenkov technique relies on timing as a discriminatory part of the trigger, multiple scattering is usually neglected. Both processes are related to the amount of material traversed, which is related to the density of a medium. In the atmosphere the overwhelming reason for density variation in the atmosphere is related to cloud formation.

Absorption

By far the most noticeable variation in count rate is when a cloud passes through the field of view, as figure 3.2 shows. Due to the warmer infra-red brightness temperature of cloud to that of the clear sky the strength of emission in 'atmospheric windows' can be used to trace the water vapour column density. This means that with radiometers of sufficient accuracy cloud can be monitored in all stages of development, even the sub-visual cirrus that is naked to the human eye could still have an effect on the count rate of an atmospheric Cerenkov telescope. Chapter 3 details the use of an infra-red radiometer in monitoring the performance of the University of Durham Mark 6 imaging atmospheric Cerenkov telescope.

Scattering

Scattering of photons in the atmosphere can be split in to two categories. Firstly there is Rayleigh scattering due to the molecular component of the atmosphere and secondly there is Mie scattering due to the aerosol component of the atmosphere.

Rayleigh scattering

Rayleigh scattering occurs when light is scattered by a particle smaller than the wavelength of light being scattered. It is described (for unpolarised light) by a simple normalised phase function of scattering angle γ

$$P_R(\gamma) = \frac{3}{16\pi}\frac{2}{2+\delta}\left[(1+\delta) + (1-\delta)cos^2(\gamma)\right] \tag{2.5}$$

with δ being the depolarisation factor due to anisotropic molecules ($\delta \sim 0.0029$ for the atmosphere) which means that the scattering is relatively uniform in all directions. Rayleigh scattering is proportional to λ^{-4}, so it is more pronounced for shorter wavelengths. This is why we see blue skies and red sunsets. As Rayleigh scattering can be easily described and the molecular distribution of the atmosphere is reasonably well understood it is relatively straightforward to model the Rayleigh scattered component of Cerenkov light.

Mie scattering

When the scattering particle is of order of the same size as the wavelength of light being scattered then Mie scattering is the dominant process. Unlike Rayleigh scattering this is a very complicated process that depends on the size distribution, composition and

the shape of the scattering particles. The scattering is asymmetric with a forward peak, which means that in light measurements with short integration times (like Cerenkov astronomy) Mie scattering tends to dominate over Rayleigh scattering. Mie scattering does not have the pronounced wavelength dependence of Rayleigh scattering either, going as λ^{-1}, which is why we see clouds as white. Another complication is that the scattering phase function can also depend on the water vapour concentration of the atmosphere as this affects the size and shape of aerosols.

2.4.3 Effective collection area of an atmospheric Cerenkov detector

An air shower can be sampled by a detector placed anywhere within the Cerenkov light pool. This means an atmospheric Cerenkov telescope has a large effective area, which helps combat the small flux of VHE γ-rays. In order to convert the observed rate of γ-ray showers to a flux from the source it is necessary to know the effective area over which γ-ray showers are distributed on the ground. The effective collection area at a particular energy is calculated by simulating γ-rays falling at random positions over a sufficiently large area (A_0). This is typically a circle of 300 m in simulations for the Mark 6 telescope. All areas are defined in a plane perpendicular to the optic axis of the telescope. By recording the number of showers that trigger the telescope and pass the selection criteria the effective area at a given energy is given by

$$A(E) = A_0 \frac{\text{number passing selection at } E}{\text{number simulated at } E} \tag{2.6}$$

where the selection criteria are those required for the shower to trigger the detector package on a telescope (the trigger requirements for the Mark 6 telescope are described in chapter 3). The collection area goes to zero for very low energies as there is not enough light to trigger the telescope. At high energies a limit to the distance of the centre of the light pool is imposed as the light distribution falls off rapidly after the 'shoulder' of the light pool.

2.4.4 Threshold energy of an atmospheric Cerenkov detector

As stated earlier, the amount of Cerenkov light produced in an air shower is proportional to the energy of the particle that caused that air shower. There is a minimum amount of light that needs to be recorded by a Cerenkov telescope for an event not to be considered a random fluctuation of the night sky background, i.e. there is a threshold of signal to noise that needs to be crossed. This threshold gives the minimum energy a γ-ray photon

has to have in order to trigger the telescope. The Poisson fluctuation of the night sky background, $N_{\rm nsb}$, is related to

$$N_{\rm nsb} \propto \sqrt{\Omega A \tau \eta \phi_{\rm nsb}}$$

where $\phi_{\rm nsb}$ is the flux of night sky background photons ($\sim 10^{12}\,{\rm photons\,cm^{-2}\,s^{-1}\,sr^{-1}}$), Ω is the solid angle subtended by the detector, A is the area of the flux collector (mirror area), τ is the integration time of the detector electronics and η is the quantum efficiency of the photodetector. One of the methods of reducing the night sky background is to match the integration time of the electronics to the short timescale (10's of nanoseconds) that the Cerenkov light front is expected to last and have the solid angle subtended by the detector close to the size of the Cerenkov light angle. This means that whilst there is a lot of night sky background about, the Cerenkov photons effectively arrive all at once and can therefore outnumber the night sky background over a short enough timescale. The photons of Cerenkov light are fairly evenly distributed across the pool, this means the signal of the Cerenkov pulse will therefore be related to the number of them caught by the flux collector and the quantum efficiency of the photodetector, $S \propto \eta A$. The minimum energy of the γ-ray needed to give a readable signal is then found via

$$E_\gamma \propto \left(\frac{S}{N}\right) \propto \sqrt{\frac{\Omega \tau \phi}{\eta A}}.$$

The chief weapon in reducing the threshold energy of an atmospheric Cerenkov telescope is therefore down to the mirror area of the detector built.

The effective threshold energy of a telescope is a useful quantity for comparing the responses of different detectors and for estimating the flux of γ-rays above a pre-determined threshold energy. An ideal detector is taken as having a constant collection area above the threshold energy and zero below it. Whilst there is no universally agreed upon absolute method for calculating the threshold energy [71, 6] it can be defined as the energy that maximises the relation $E^{-\alpha}A(E)$. The differential spectral slope for cosmic-rays, with $\alpha \simeq 2.6$, is a well measured quantity and provides an abundant signal from any position on the Earth, so can be useful for modelling the telescope response. If there is a standard candle object of VHE γ rays in the field of view, such as the Crab nebula for northern hemisphere observatories (and having a differential slope of $\alpha \simeq 2.4$ [102]), this can be a useful quantity for comparison, but only for observatories that share that object in the night sky. The effective collection area is taken as the area that an idealised detector would have in order to match the triggering rate of the real telescope. It is prudent to

avoid the region below the threshold energy when attempting to determine energy spectra due to the difficulties of modelling the hardware trigger.

2.5 γ-hadron separation

As stated earlier, the number of air showers due to charged nucleons outnumber those due to γ-rays by a thousand to one. This represents a massive background signal and a huge obstacle to VHE γ-ray astronomy, it is therefore imperative to exploit the inherent differences between air showers of different origins. One technique employed to overcome this was to exploit the differing paths the primary particles take on their trip to Earth. The charge of a cosmic-ray causes its path to be deflected by the galactic magnetic field, their arrival directions become randomised and the cosmic-ray signal will be isotropic across the sky. However, as the γ-ray is a neutral particle its path will not be affected by the magnetic field and the trajectories point straight back to the source. Given a long enough exposure (on and off source) the γ-ray signal will present itself as an excess number of events in the direction of a suspected source. This method, unfortunately, takes a *long* time, months worth of observations will still only lead to a marginal result due to the low flux of VHE γ-rays and the small duty cycle of a Cerenkov telescope. If the source of γ-rays exhibits a periodic modulation of the signal this can be used as an extra source of information in detecting an object. Whilst many claims were made from this method of analysis, the results were unconvincing and unreproducible. It was not until the advent of accurate codes simulating air showers and the introduction of arrays of photomultipliers in a camera form that TeV γ-ray astronomy really started to come of age.

2.5.1 Hillas parameters

Figure 2.5 demonstrates the distribution of light as seen from a γ-ray initiated air shower and from a proton initiated air shower. The light from the γ-ray air shower in figure 2.5(a) is seen to be distributed fairly evenly across the ground: this is in stark contrast to the 'blotchy' appearance of the light from the proton based air shower in figure 2.5(b). The transverse momentum imparted to the secondary particles acts to spread what small amount of light (relative to that of a γ-ray of comparable energy) is generated from a cosmic-ray air shower. When imaged in a camera, the light from an air shower can be used as a powerful discriminatory tool. Figure 2.6 shows the important parameters used

in defining the shape of an image in the camera. These are known as the Hillas parameters from the work of Hillas [45, 46]. The *width* of an image is the length of the semi-minor axis of the image and is sensitive to the lateral spread of the shower. The *length* of an image is then the length of the semi-major axis and a description of the longitudinal spread of the image. If the γ-ray image were viewed directly at zenith it would appear as a circle, but sources are rarely at zenith and this necessity is indeed a virtue. The γ-ray image is projected as an ellipse in the camera with the long axis of the ellipse pointing back to the source position. A γ-ray image can then be defined on its *ellipticity*. The *miss* of an image is the perpendicular distance between the major axis and the centre of the field of view, it is a measure of the orientation of the image and is sensitive to the arrival direction of the candidate event. The *distance* measures the separation of the centroid of the image to the centre of the field of view and can be used as a measure of the distance of the telescope from the point on the ground where the shower core would have landed, known as the impact parameter. When combined with the value of *miss* the pointing angle α is obtained. The angle, α, between the long axis of the ellipse and the source position in the camera is a very powerful way of removing the cosmic-ray background. The isotropic cosmic-ray background should have a random distribution of pointing angles, whereas the γ-ray showers, coming from a point source, will have an excess of events clustered at small α from the source position in the camera. In much the same way that the trails in a meteor shower point back to a common origin on the sky, so the γ-ray signals point toward their source.

Below $\sim 40\,\mathrm{m}$ from the impact point there are fluctuations produced by penetrating particles reaching the ground and after the shoulder of the light pool, $\sim 120\,\mathrm{m}$ from the impact point, the light distribution tails off rapidly. In between these limits the light distribution is roughly constant and so a good measure for the energy of the primary particle. With this in mind it is necessary to impose upper and lower bounds on the value *distance* for measuring the energy, as the *distance* of the image centroid from the source position gives a measure of the distance to the impact point of the air shower. Giving a lower bound to the *distance* of the image will also mean it has a certain amount of *ellipticity* to enable image cuts to work. An upper bound to *distance* prevents distortion of the α distribution which arises as the image gets closer and closer to the edge of the camera, as the image moves further out then any light falling outside of the camera will not register as part of the image and the shape of the light distribution will give an α perpendicular (favouring a value of $\sim 90^\circ$) to the source. The *size*, or *brightness*, of an

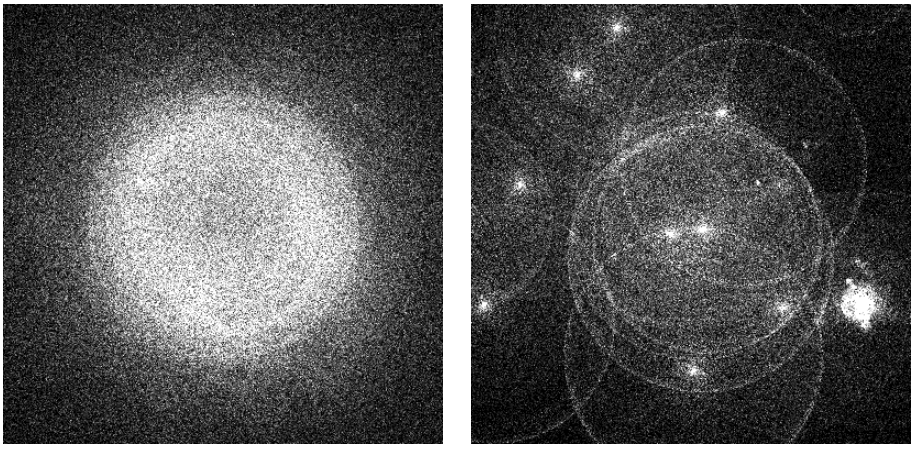

(a) a 300 GeV γ-ray primary (b) a 1 TeV proton primary

Figure 2.5: The lateral distribution of Cerenkov light from air showers. The image on the left is for a 300 GeV γ-ray and on the right for a 1 TeV proton. The area displayed for each image covers $400 \times 400\,\mathrm{m}^2$ with the shower core at the centre. The simulations were produced with CORSIKA 4.50 without any atmospheric extinction. Note that extinction would reduce the rings seen in the lateral distribution of proton showers which are produced high in the atmosphere, but the bright spots are from particles reaching the ground and would not be affected by extinction. Created by K. Bernlöhr and can be found on the web at http://www.mpi-hd.mpg.de/hfm/CosmicRay/ChLight/ChLat.html

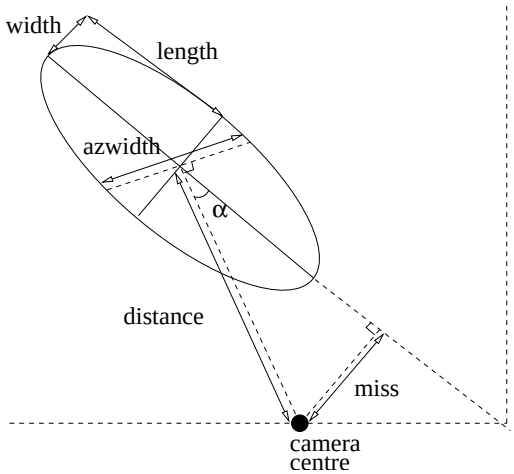

Figure 2.6: The Hillas parameters used in discriminating γ-ray generated air shower images. The angle, α, between the long axis of the ellipse and the source position in the camera is very powerful way of removing the cosmic-ray background.

image is a description of the amount of light contained within the image and is another useful quantity as it gives a measure of the energy of the primary particle. The amount of light generated in an air shower being proportional to the energy of the primary particle as seen in section 2.3.1. If a measure of the spectral slope of an object is required it is neccesary to know how the image *brightness* correlates with the energy of the primary particle. The amount of light contained within the two brightest pixels of an image as compared to the total amount of light in the whole image has also been used as a discriminator, known as *concentration*, with γ-ray signals being more concentrated than cosmic-ray ones.

The design of the University of Durham atmospheric Cerenkov telescopes allowed for an extra parameter, known as D_{dist}, to be at disposal when cutting data to find γ-ray images. By employing three detector elements at a small, fixed distance apart means that a more uniform Cerenkov light pool (of the kind that γ-ray showers produce) is needed to trigger the detector and an attempt to stereoscopically determine the height that most of the Cerenkov light was produced in the atmosphere can be made by examining the angular separation of the images of the shower produced in the three cameras. As the cosmic-rays penetrate further into the atmosphere the height of shower maximum will consequently be shifted down relative to *gamma*-rays. A description of the three detector trigger of the University of Durham telescopes is given in 3.

2.6 Imaging atmospheric Cerenkov telescope installations

Atmospheric Cerenkov telescopes come in many guises from single dish designs through multiple telescope arrays to converted solar heliostats. By far the most successful variant is the imaging atmospheric Cerenkov telescope (IACT) which utilises a camera of photodetector elements to image the light from an air shower and suppress background events by using the inherent differences in the air shower. Segmented dishes composed of many individual mirror facets are generally used to collect the Cerenkov photons. Making a single large mirror is an expensive and painstaking process and not easy to replace if damaged. Since Cerenkov telescopes are not surrounded in domes they can be quite exposed to the elements and so run the risk of damage, or at least deterioration. The mirrors can be arranged either in a parabolic design for good timing resolution, or in a Davies-Cotton design for better off-axis imaging. The converted solar heliostats offer a very large area mirror, providing them with a very low energy threshold, but have

added complexities from the night sky background and the trigger conditions that make them a very challenging prospect technically [79]. The following discussion describes the chequered history of some of the major players with a distinctly Durham perspective.

2.6.1 High altitude telescopes

The University of Durham group first operated Cerenkov telescopes out of Dugway, Utah. Arguably, the most successful of these early observations was the coincident detection of emission from the low mass X-ray binary Hercules X-1 by the Durham telescopes and the Whipple telescope [24]. Hercules X-1 is an object that has brought much speculation to the field of VHE γ-rays and X-ray binaries with the advent of imaging telescopes [89], a field pioneered by the Whipple group.

The Whipple IACT is the archetype of the field. It pioneered the use of imaging cameras for γ-hadron separation, a technique that led to the first significant detection of the standard candle in VHE γ-ray astronomy - the Crab Nebula [106]. A high resolution imaging camera gave a $5\,\sigma$ detection of the Crab nebula in 1 hour [102]. The telescope is located at an altitude of 2300 m atop Mt Hopkins in Arizona. It consists of a series of mirrors mounted in a Davies-Cotton configuration to make a single 10 metre dish and has an energy threshold of ~ 250 GeV. Further details can be gleaned in [22].

A single dish telescope suffers background signals due to the effects of local muons in the atmosphere, being a by-product of air showers surviving to ground level, as discussed earlier in the chapter. A single muon at ground level will cast an annulus of Cerenkov light (provided its kinetic energy is above 4 GeV remember) that will trigger a single dish telescope. These muon rings can be used as a means of calibrating the camera of an imaging atmospheric Cerenkov telescope, but are very difficult to pick out from the sea of images that an observing run will bring up. The effect of a single muon travelling through the camera itself can not be compensated for. By using a 3 dish telescope, a design philosophy of the Durham group, these effects can be eliminated. The muon annulus will not light up all 3 dishes and a single muon travelling through the detector of a single dish will not trouble the detectors on the other two dishes. The details of the three fold spatial trigger will be explained further in chapter 3.

2.6.2 Sea-level telescopes

In 1986 the Durham group moved its base of operations to the Bohena Cosmic Ray Observatory near Narrabri, New South Wales, Australia, the temptation being that the

galactic centre is only really viewable through southern hemisphere skies. Also located in Australia is the CANGAROO (Collaboration of Australia and Nippon for a Gamma Ray Observatory in the Outback) project, operating out of Woomera. CANGAROO I was a 3.8 m diameter telescope and CANGAROO II a 7 m telescope, built as single dishes like the Whipple telescope. There is a considerable difference in energy threshold between the Whipple and CANGAROO telescopes, CANGAROO I having a ~ 1 TeV energy threshold and CANGAROO II a ~ 500 GeV threshold. Whilst the difference in mirror area explains most of this difference (see section 2.4.4) there is also a subtle effect at work here. There is a quite a difference in altitude between the CANGAROO and Whipple telescopes, with Woomera being just 160 m above sea level (a.s.l.); this causes the Cerenkov light pool to be spread over a wider area, reducing the density of Cerenkov photons on the ground and making it more difficult to go over the threshold of the night sky background; it also means that there is more atmosphere to traverse and therefore more attenuation of the Cerenkov light, further reducing the light density. The Durham site at Narrabri is also only ~ 0.2 km above sea level, but the design philosophy of the Durham telescopes aimed to compensate for this loss of sensitivity. By requiring a three-fold spatial trigger, explained further in 3.1, the photomultipliers can be run at a higher gain, in an attempt to make them more sensitive to the lower light levels.

2.6.3 Stereoscopic arrays

The Durham group also operated another high altitude telescope on La Palma (28.75 N, 17.89 W, 2200 m a.s.l.) in the Canary Islands for two observing seasons in 1988-89. La Palma has since become the home of the HEGRA (High Energy Gamma Ray Astronomy) group, a project that utilises multiple telescopes in a stereoscopic design. The spacing of the HEGRA telescopes allows for much better sampling of the uniformity of a γ-ray initiated light pool compared to the more uneven distribution of light from a hadronic primary, by having 5 identical telescopes arranged on a square grid of 100 m side with one telescope in the centre. It also allows for a better reconstruction of the depth of maximum of the air shower, another means of discriminating between air shower types due to the more penetrating nature of cosmic-rays. A third benefit of this method is that a shower position can be reconstructed on an event by event basis allowing for a more accurate mapping of γ-ray source positions [3].

2.7 Summary

In this chapter we have seen how highly relativistic charged particles can produce Cerenkov radiation. We have explored how high energy photons and cosmic-rays generate extensive air showers of ultra-relativistic charged particles within the atmosphere and how simple detectors can pick out the resultant Cerenkov light emission. We saw how many particles were generated, how deep into the atmosphere the shower maximum penetrates and how much Cerenkov light is emitted is a function of the composition and initial energy of the primary particle: photons interacting earlier in the atmosphere and generating a higher Cerenkov light yield than a cosmic-ray of comparable energy. We have seen how imaging of the Cerenkov light pool is a useful discrimination technique in removing the much larger cosmic-ray background. Next we look at one of the telescopes built to exploit the imaging atmospheric Cerenkov technique in more detail.

Chapter 3

The University of Durham Mark 6 telescope

3.1 Introduction

The University of Durham operated a series of atmospheric Cerenkov telescopes at the Bohena cosmic-ray research station situated just outside Narrabri, New South Wales, Australia (30.32° S, 149.57° E) culminating in the Mark 6 telescope, a description of which follows. The Durham telescope design philosophy was strongly based on a four-fold coincidence principle: three spatial elements and one time based. Viewing the Cerenkov light with three separate flux collectors removes the background due to the effects of local muons in the atmosphere and the PMTs that a single dish telescope experiences. Another advantage is that spatially well separated detectors sampling a Cerenkov light pool can provide a better discrimination between the smoother distribution of the light within the pool given by a γ-ray induced air shower to the fluctuating nature of a hadronic primary based air shower [105], the fluctuations occuring on a scale of order $\sim$ 10 metres. It was the aim to exploit this feature by mounting three large flux collectors on a single alt-azimuth mount. Having a large mirror surface increases the amount of Cerenkov light caught by the telescope and by operating a multiple reflector telescope and using fast coincidence techniques it is possible, for a fixed rate of accidental triggers, to run at a higher detector gain and so achieve a lower energy threshold. This is of particular importance as the telescopes were operated near to sea level and so lose the natural advantage of a reduced energy threshold which applies to mountain altitude instruments.

3.2 The University of Durham Mark 6 imaging atmospheric Cerenkov telescope.

The University of Durham Mark 6 imaging atmospheric Cerenkov telescope (hereafter Mark 6) operated from 1996 to 1999 and was the last of a series to follow the Durham philosophy, see [6] for a full description of the telescope. The event selection for the Mark 6 telescope needed signals from the following in order to generate a trigger:

- The left/right flux collectors. These were each viewed by 19 hexagonal PMTs. An event selection is triggered whenever a signal was detected from a pair of PMTs at similar positions in the left/right detectors.
- The central flux collector. Viewed by a camera including 91 imaging pixels covering a similar area of sky as the left/right PMT matrices and a further 18 guard ring elements. For an event to be selected it was required that any adjacent 2 of the 7 camera pixels which corresponded to a signal in the left/right flux collectors fired.

These conditions needed to be met within a hardware controlled $\sim 10\,\mathrm{ns}$ coincidence window.

3.2.1 The large area flux collectors

The Mark 6 telescope consisted of three $42\,\mathrm{m}^2$ parabolic mirrors, constructed of 24 segments each. The mirrors were manufactured from an aluminium honeycomb material: Aeroweb 3003, having a cell size of 0.8 cm, a foil thickness of 0.06 mm and an overall web thickness of 50 mm. The honeycomb is bonded to a dural backbone and surrounded by a dural frame by a Redux 420A/B (Ciba-Geigy) adhesive. The reflecting surface is Alanod 410G special aluminium sheet of 0.5 mm thickness, anodised during manufacture to have a specular reflection $\geq 75\%$ over a wavelength range of 350 to 700 nm (falling to $\sim 60\%$ by 280 nm). This design meant that the mirrors were lightweight, of low cost and easy to manufacture in large numbers. A mirror focal length of 7.0 m and an aperture f/1.0 to give an image scale compatible with a camera of 91 elements each with a 0.25° diameter was specified. The reflectivity of a sample of the front surface material did not significantly deteriorate from exposure to an industrially polluted atmosphere over a period of 24 months and the mirrors from the Mark 3 telescope showed no signs of significant deterioration after ten years' worth of exposure to the elements, demonstrating the longevity of the mirrors.

A disadvantage of aluminium mirrors is that they are radiatively well coupled to the night sky. On cold, humid nights the surface temperature of the mirrors can drop below the dew point, meaning that the mirrors would mist up and severely reduce the reflectivity of the mirrors. It was found that spraying the mirrors with a solution of water and commercial rinse-aid at the start of an evening's run when the environmental conditions suggested that misting could be a problem prevented any condensation forming by reducing the surface tension of the water drops and allowing them to run off.

3.2.2 The photodetectors

The Mark 6 central camera consisted of 91 25mm diameter Hamamatsu R1924 circular PMTs surrounded by a guard ring of 18 56mm diameter Phillips XP3422 hexagonal PMTs. The left/right trigger detector packages consisted of 19 56mm Phillips XP3422 hexagonal PMTs each. Aluminium light concentrators were mounted on the front of the detectors to concentrate the light into the central portion of the PMTs and improve their temporal response. For the left/right hexagonal triggering detectors the total amount of light was reduced by a few percent, but the rise time of the signal was reduced by 15% and the height of the signal increased by 15%, corresponding to a decrease in threshold by a similar amount. In the central camera the dead area between the 25 mm tubes amounted to 45%, but the conical reflective light guides for these tubes resulted in a 70% increase in the detected light pulse.

3.2.3 The telescope steering/pointing

The three flux collectors were supported by a custom made alt-azimuth mount. The control of the attitude of the telescope was via DC servomotors driving onto gears mounted directly on the telescope structure. Angles were sensed by absolute 14-bit digital shaft encoders with a resolution of 0.022°. Whilst the full 14-bit value was recorded for each event only the 12 most significant bits, however, were returned to the steering computer by a digital servomechanism every 100 ms for comparison of the zenith and azimuth of a source. This meant that a source could be offset from the camera centre by up to 0.1°.

The position of the telescope was also monitored by a co-axially mounted CCD observing guide stars in a $2^\circ \times 2^\circ$ box around the source. This allowed the pointing of the telescope to be determined more accurately in the offline data analysis, which is discussed in more detail in section 3.4.6.

3.2.4 Timing and clocks

A rubidium atomic oscillator provided a frequency standard for the whole of the Narrabri site. An Efratom model FRK-L Rb oscillator, providing a stable 10 MHz reference signal, was used for this purpose. The drift rate was regularly monitored and measured by comparison to the signal from a GPS receiver, providing a daily absolute comparison with the local time standard. All events were timestamped to a relative accuracy of 1 μs and with an absolute accuracy of $\leq 10\,\mu$s.

3.2.5 Environmental monitoring

The Mark 6 was equipped with extensive monitoring equipment to give details of wind speed, screen level atmospheric pressure and air temperature, mirror temperature and the temperatures inside the detector packages and laser system. The PMTs, electronics and laser calibration system were susceptible to variations in the ambient temperature and so the PMTs and electronics were always warmed prior to observing runs and thermostatically maintained at a high temperature. The mirror temperature monitor meant the mirrors could be sprayed to prevent misting were the mirror temperature to fall below dew point.

3.3 Observing modes

There are four different strategies that can be utilised when observing sources of VHE γ-radiation.

3.3.1 Tracking

Tracking mode follows a source through the sky, giving the maximum amount of on-source data and hence γ-rays for a given exposure. This mode, therefore, is only useful for a source where periodic variations in signal strength can be expected; or when a robust enough method for selecting γ-ray events and rejecting background events has established there is no need for a control sample.

3.3.2 Chopping

For an unconfirmed or weak source a background dataset provides a control sample for comparison purposes. The background field is offset from the on-source field by a set

amount in Right Ascension equal to the duration of each on/off segment in minutes. This allows the telescope to track through the same region of sky for each segment and hopefully record under identical operating conditions. The Mark 6 data chopped in 15 minute intervals. This avoided overlap between the two fields due to the 2° field of view of the camera, but ensured similarity between the two fields of sky. The off-source field is always selected to be of a similar brightness to the on-source field (see section 3.4.5 on padding as to why this is important). Fifteen minutes is also short enough to minimise secular variations in count rate due to changing conditions (e.g. sky clarity, temperature, etc). Observations are made in cycles of on-off-off-on or off-on-on-off in attempt to counteract biases due to changing conditions.

3.3.3 Drift

A drift scan allows a source to transit through the field of view as the telescope maintains a constant azimuth and zenith position. Observing equal angular regions either side of the source gives a control sample. A detection is then an excess of Cerenkov showers coincident with the source position. This method may be useful for surveying large regions of space, such as the galactic centre, perhaps for transient events, but it is susceptible to changing sky and instrumental conditions.

3.3.4 Wobble mode

This strategy aims to maximise the on-source observation by estimating the background signal and thus eliminating the need for off-source scans. The γ-ray source is offset in declination from the telescope axis. A region offset by the same declination, but in the opposite direction, then provides an area of sky with which to estimate the background signal. The offset declination is switched around after a set interval of time to prevent any systematic difference being present between the γ-ray source and the extrapolated background source.

3.4 Data calibration and processing

Raw PMT data cannot be used to accurately measure image parameters in data analysis. It is necessary to know the gains of each PMT and the amount of contamination from background light in order to accurately relate the digitised output to the observed Cerenkov photon density. The PMT high voltage supplies were set such that the output

from each tube is similar when exposed to the same amount of light, but this approach is limited by certain restrictions on PMT performance and noise fluctuations. This means it is not possible to completely flat-field a camera and so the relative performance of each tube needs to be monitored throughout an observation.

3.4.1 PMT absolute calibration

The absolute calibration of the electronics and PMTs was initially performed using a 'pill'. This consists of a radioactive ^{241}Am source contained within a small piece of plastic scintillator. The 'pill' produces a ~ 300 photon flash of ~ 3 ns duration at a rate of about 1 kHz. It was placed a fixed distance from the face of the PMT in complete darkness and the pulse area spectrum is recorded, which when combined with a knowledge of the emission characteristics of the light pulser allowed the absolute gain of each PMT to be calculated.

The absolute calibration of the PMTs provides necessary information for determining the energy threshold of the telescope, but the method has a major drawback. The amount of light produced by the pulser is so small that the calibration can only be performed in absolutely dark conditions in order to measure the signal over the noise. As a result, calibration can not be performed continuously over an observation. Since the tube gain is dependent on background light illumination, a method for measuring tube gain which allows for monitoring of the night sky background as well is necessary.

3.4.2 PMT relative calibration

Throughout an observing run a nitrogen laser was randomly fired at a plastic scintillator at an average rate of 50 min^{-1}. This 3 ns pulse of 337 nm radiation was converted to a pulse of 400 ± 20 nm radiation in the scintillator, which was then transmitted by means of a plastic fibre optic cable to the centre of each of the three mirrors. Once there it was diffused by an opal diffuser to produce a pulse of light that was uniform over the face of the detector package. A single PMT was placed in a collimator next to the camera so that it only views the light pulse produced by the laser and no light reflected by the mirrors. Signals from this PMT then provide a simple and reliable method of identifying the laser's random calibration triggers.

This procedure allowed the PMT gain to be measured to $\pm 2\%$ for each 15 minute data segment. This can only be a relative measure of the gain, however, as the number of photons varies per laser flash.

3.4.3 PMT pedestal calibration

In the absence of a Cerenkov signal a PMT will record the random, statistically fluctuating signal from the night sky background. In order that a small Cerenkov signal can be measured in the presence of a large negative background fluctuation the electronics units measuring the PMT signals were provided with a DC offset. This offset is known as the pedestal and is subtracted from the data prior to analysis. Events recorded by a random trigger (that is separate from the laser random trigger) are unlikely to contain Cerenkov photons. The mean of the distribution of the randomly triggered events for each tube therefore provides a value for the pedestal of that tube for each segment.

3.4.4 PMT sky noise measurement

An estimation of the sky noise for each tube comes from the standard deviation of the distribution used to identify the pedestal values. A measure of the noise in a tube is important since negative fluctuations can act to cancel out a Cerenkov signal. The imaging technique relies on the shape of the light distribution in the camera in order to discriminate between γ-ray and background cosmic-ray events. A pixel is determined to be a part of the image if the signal contained within it is greater than some multiple of the tube noise. For each event the tube with the largest corrected pulse size ($\mathrm{QT_{max}}$) is identified; the pixels for each event are then defined to be one of the following

- a pixel is defined as an 'image' pixel if the corrected pulse size is $> 37.5\%$ of $\mathrm{QT_{max}}$ and $> 4.25\,\sigma$;
- a pixel is defined as a 'border' pixel if the corrected pulse size is $> 17.5\%$ of $\mathrm{QT_{max}}$ and $> 2.25\,\sigma$ and if it is next to an 'image' tube;
- Otherwise the pixel is set to zero;

where σ is the tube's rms noise. As the noise in a tube increases with brightness, so will the likelihood of a random negative fluctuation cancelling out a Cerenkov signal in a tube. If the camera is viewing a bright field then the chances are that some of the tubes that would otherwise be recorded as border pixels will fail to meet the threshold criteria and so be rejected, resulting in a reduction of the number of tubes in an image and correspondingly a reduction in the *width* and *length* of an image. This can be particularly bad when viewing an object in the chopped mode when there is a systematic difference in the brightness of the on-source and off-source background field, since it could lead to a

systematic difference in the number of events retained after cutting, possibly even leading to a false detection of a source. It is for this reason that software padding (see 3.4.5) is introduced.

3.4.5 Padding

The behaviour of the PMT varies with the level of background illumination; in particular, the size and rate of noise pulses increases with background light brightness. As the response of a PMT to noise increases so will the likelihood that noise fluctuations will cancel out a Cerenkov signal. This may lead to systematic differences between the number of events retained in on- and off-source observations due to the difference in star field brightnesses. Software padding is a process that adds randomly generated noise to the darker pixel of an on/off pair until the noise levels match. The technique seems to be very efficient at removing bias induced by background starlight without losing sensitivity to Cerenkov light [23, 91].

3.4.6 CCD

As an independent means of verifying the telescope position an SBIG ST-4 CCD camera was co-axially mounted to provide positional information by monitoring guide stars in a $2^\circ \times 2^\circ$ field of view. A 5 second full frame exposure was recorded at the start of each observation and then frames of typically 3 second integration time were updated throughout the run. Guide stars of magnitude $m_\mathrm{v} \sim 8$ can then be used to provide absolute position sensing to better than 0.008°.

Measuring the extinction of star light has also been touted as a method of monitoring sky clarity and therefore the atmospheric attenuation of Cerenkov light. This method has some drawbacks which are discussed in section 3.5.1.

3.4.7 Quality control

To be considered as suitable for analysis, data must satisfy the criterion that the weather be deemed clear and stable; there are no obvious electronics problems in the data acquisition system; and the difference in the number of events between corresponding on- and off-source segments be $\leq 2.5\,\sigma$ (where σ is calculated via equation 4.1) to avoid any systematic bias in the data sample, e.g. from a cloud in the field of view for one segment. A γ-ray signal is very unlikely to show up as a significant excess in a raw data set and so

the on- and off-source number of counts should be similar, within the limits of Poissonian counting statistics. Data taken at large zenith angles ($> 45°$) may be analysed, but is unlikely to respond to the same treatment as data from small zenith angles due to various effects, such as the increase in path length of a shower.

3.4.8 Barycentring

In analyses where timing parameters are important, such as searches for periodic emission, it is necessary to measure the arrival time of photons to a fixed position in space. This accounts for effects due to the motion of the telescope on Earth and the motion of the Earth through space. To do this a three stage correction must be applied:

i) translation of the event times to the centre of the Earth;

ii) translation of the event times to the centre of gravity of the solar system;

iii) and application of relativistic corrections.

The first stage compensates for the Doppler effect of the rotation of the surface of the Earth and corrects for the absolute position of the observatory. These corrections can alter pulse arrival times by up to 21 ms (the time taken for light to travel a distance comparable to the radius of the Earth). Translation to the solar system barycentre accounts for the same effect due to the Earth's motion around the sun and around the Earth/Moon system barycentre. The corrections are based on the JPL DE200 Earth ephemeris [95] and can be up to 500 s. The relativistic correction is necessitated by the fact that the Earth moves in an elliptical orbit deep within the gravitational potential well of the Sun. Whilst this is not a large correction in comparison to the others, $\simeq 3$ ms at most, it can be significant when millisecond pulsar candidates are considered.

3.4.9 Focusing of event times

A similar focusing of event times in order to compensate for the orbital motion of binary systems can be necessary. The angular velocities in binary systems can be very large, resulting in significant Doppler effects due to high velocities of candidate systems along the line of sight. Corrections are applied based upon orbital ephemerides obtained at other wavelengths (mostly in the X-ray regime) and assume that the site of VHE emission is coincident with the site of emission at the other wavelength - if this has not been established then the focusing of event arrival times should not be performed.

3.5 Monitoring sky clarity

3.5.1 Motivation

Measuring the clarity of the sky gives important information on the transport of photons from the air shower production site to the telescope. It is important to know whether changes in count rate are due to variability in a source or variability in observing conditions; be they night to night variations in aerosol content of the atmosphere affecting the optical depth or merely the effect of a cloud moving across the field of view. With the desire for the next generation of atmospheric Cerenkov telescope facilities to have an unprecedented energy resolution to enable spectroscopic studies of sources it becomes even more important to have a clear idea of the clarity of the sky. A number of sky monitoring possibilities exist. The performance of the γ-ray telescope to the ever present cosmic-ray background is one such way [62], but has the disadvantage of depending on the performance of the Cerenkov detector itself and can be difficult to quantify. Monitoring the brightness of a star in the field of view of the telescope is a passive and independent method employed by many ground based γ-ray telescope installations and routine at optical observatories. This technique also has many drawbacks, there is not necessarily a star of appropriate brightness in the field of view: measurements of faint stars using inexpensive CCDs tend to be noisy, giving an imprecise estimate of atmospheric clarity; and bright stars ($m_{\mathrm{v}} \sim 3$ or more) are a source of unwelcome background noise in the PMTs. This method can also lead to an overestimate of the amount of Cerenkov light produced, particularly when extrapolating down to sea level, due to differing assumptions on the vertical structure of the absorbing layers [15]. One example of a bad assumption is to take the density of aerosols as proportional to air density. Figure 3.1 shows the differing transmission profiles that can be generated based on different assumed aerosol structure models. The aerosol-air proportionality leads to an overestimate by 4-8% of the Cerenkov light even if the star light extinction is taken into account. The reason for this is that the Cerenkov light is produced, say, halfway through the atmosphere, implying 50% of the starlight extinction, but in fact some 80-90% of the aerosol extinction takes place below the average Cerenkov light production height.

Probing the infrared has now become an established method for detecting cloud and establishing sky clarity in a quantifiable and reproducible way, see [8, 35, 19, 36, 99] for examples employing pyroelectric, thermopile, radiometric and spectroscopic instruments. Gases emit radiation through discrete lines and bands, whereas solids and liquids emit

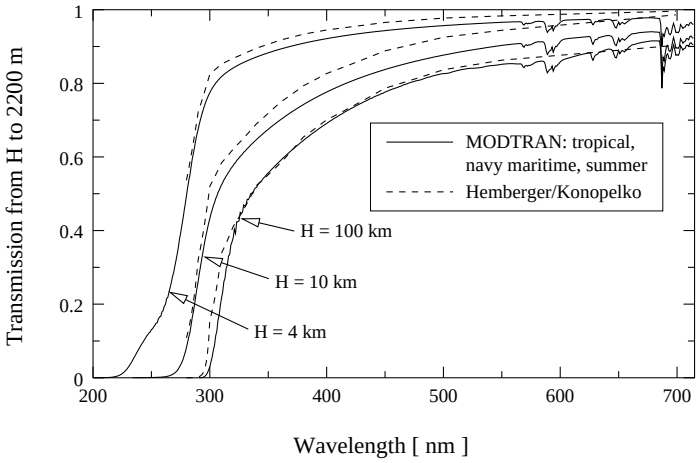

Figure 3.1: Comparison of atmospheric transmission as calculated with MODTRAN v 3.5 using the tropical profile and navy maritime summer haze model (unbroken line) and in a transmission model with aerosol absorption proportional to atmospheric density (dashed line). Note that although both transmission models have almost the same transmission for stellar light, the transmission from typical Cerenkov emission altitudes differs significantly. Figure taken from [15].

a blackbody spectrum. By observing in a 'window' region devoid of atmospheric gas emission lines it is possible to detect the build up of cloud. Clouds show up as a noticeably warmer infra-red signal due to their greater efficiency as a blackbody emitter than the clear sky. In fact, whilst most gases exhibit only characteristic lines of emission water vapour also has a continuum emission, attributed to weak hydrogen bonds forming between the water molecules [49]. The amount of water vapour forming these bonds is related to the density of the water vapour and so the greater efficiency of emission and the different temperature lapse rate (see section 6.3.1) means regions of high water vapour density have a higher brightness temperature than that of a clear sky. This means that an instrument of sufficient resolution, observing the atmosphere in an appropriate waveband, could detect all stages of cloud development.

There is an atmospheric transmission window between 8 and 14 microns. This region of transparency in the atmosphere is affected by 3 atmospheric constituents. It is between the shoulders of emission lines from CO_2 at 15 microns and H_2O at 7 microns and contains the O_3 emission line at 9.6 microns. CO_2 has a constant mixing ratio through the atmosphere and so is invariant as far as IR emission is concerned. O_3 is found mostly in the stratosphere where it has a seasonal variation in concentration; ground level ozone is

highly variable, but is generally found in areas of high industry and particulate emissions such as cities, which are not good places for the siting of telescopes, and so ground level ozone can be considered as negligible at a good IACT site. This means that H_2O is then the atmospheric constituent that is most likely to affect the 8 to 14 micron emission, as the water vapour concentration is variable on a daily basis and has a continuum emission contribution dependent on its density. H_2O is also the prime constituent in obscuration of the Cerenkov light (due to cloud formation) so there is good reason to monitor the atmosphere in the 8 to 14 micron region.

3.5.2 Infra-red radiometers

A Heimann KT 17 model radiometer operating in the 8 to 14 μm range was employed on the Mark 6 telescope to measure sky conditions throughout observations. As stated earlier, the 8 to 14 μm region was chosen since it is in an atmospheric transmission window situated between the shoulders of the H_2O 7 μm and CO_2 15 μm bands and only contains the O_3 9.6μm feature, allowing a quantifiable measurement up to the altitudes associated with Cerenkov emission, but is responsive to the amount of water vapour present in the air due to water vapour's continuum emission. These model radiometers use a pyroelectric element employing the chopped radiation method in order to operate without the need for cooling the element.

The chopped radiation method

The chopped radiation technique alternates the signal going onto a radiometer element between a target and a reference signal. Why is this necessary? The answer to this is two-fold.

- To operate pyroelectric detectors. Infrared detectors of the pyroelectric type must chop the radiation because they respond to radiation differences only and not to absolute radiation intensities. Pyroelectrics are the best uncooled detectors available in terms of detectivity, fast response, reliability and stability.

- To eliminate thermal drift. Apart from infrared radiation from the source the pyrometer will also pick up radiation emitted by the detector enclosure, which corresponds to the pyrometer's housing temperature. This gives rise to a bias on the output signal of the detector and subsequently to thermal drift whenever the temperature of the housing changes.

A pyrometer utilising the chopped radiation method evaluates two subsequent signals

$$\begin{aligned} S_1 &= S_{\text{target}} + bias \\ S_2 &= S_{\text{reference}} + bias \\ S_\delta = S_1 - S_2 &= S_{\text{target}} - S_{\text{reference}}. \end{aligned}$$

During the short chopping cycles, normally in the millisecond range, the temperature of the pyrometer's housing and therefore the *bias* do not change. The *bias* is thus eliminated and substituted by a reference signal which can be easily measured and controlled over the permissible ambient temperature range.

The chopping itself is accomplished by an optical chopper. Essentially these are mechanical blades driven by a suitable electromagnetic device, such as an electric motor, which periodically interrupts the radiation from the measured target and exposes the detector to the internal blackbody reference radiation source.

3.5.3 The KT 17

The Heimann model KT 17 mid-infra-red radiometer is sensitive in the 8 to 14 μm wavelength region. It had a Germanium lens giving the unit a 2° field of view. It was co-axially mounted on the Mark 6 telescope as a method of determining sky clarity and to give an independent cloud monitoring system. Figure 3.2 shows the correlation between sky brightness temperature and the count rate of the Mark 6 telescope in the presence of cloud. The passage of a cloud across the field of view resulted in a very marked drop in count rate for the telescope and a large increase in brightness temperature detected by the KT 17.

3.5.4 The KT 19

Following on from where the KT 17 range left off, a Heitronics KT19.82A detector was purchased. This has a model K6 Germanium lens with 2° field of view. The unit has the capability to output temperature readings through analogue and digital ports. The digital output is via RS232. The temperature measurement is claimed accurate and linear in the range -50 to 1000°C with the possibility of going down to -60°C. This lower temperature limit was found to be inadequate from observations taken at the HEGRA array site between the 19th and 26th of September 2000, during which the KT 19 spent much of the time below the lower temperature limit. When the the sky was murky

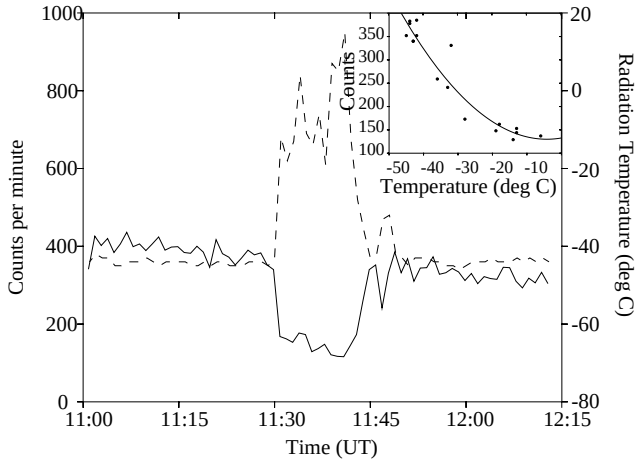

Figure 3.2: The correlation between the background counting rate of the Mark 6 telescope (solid line, left y-axis) and the radiative temperature of the sky (broken line, right y-axis). The main figure shows the variation of the telescope counting rate and radiative temperature with time. The inset figure shows the variation of the count rate with measured sky radiative temperature. Figure taken from [19].

enough to produce a high enough brightness temperature to be observable by the KT 19 the correlation between sky temperature and telescope count rate is readily apparent, as seen in figure 3.3. Follow up observations of winter skies in Durham also found the unit unable to give readings for very clear skies.

Low temperature measurement calibration

The calibration of the KT 19 is only performed down to 30°C by the manufacturer and the lower temperature behaviour is assumed to be linear below that, down to the lower recommended temperature limit of −50°C. The KT 19 can read lower temperatures, but the response is non-linear and the signal degrades very quickly. Clear sky brightness temperatures down to −86°C are conceivable, following the Idso scheme of chapter 6.2.2, in high latitude areas such as Durham, where the unit is being tested. For this reason the KT 19 was modified to read temperatures down to a manufacturer implied −75°C. To test the accuracy of this claim an attempt was made to measure the low temperature response of the KT 19. Unfortunately there are no standardised blackbody sources that operate at these low temperatures and so a makeshift alternative had to be found. Frozen carbon dioxide (dry-ice) sublimates at −78.5°C; when this dry-ice is placed in a liquid the resulting heating curve can provide a series of temperature measurement points for

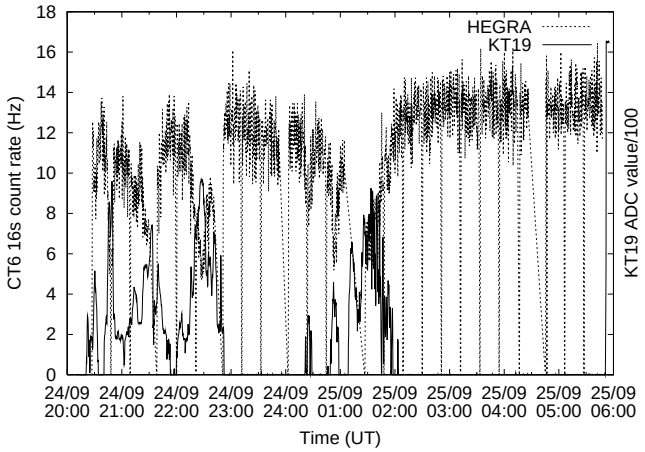

Figure 3.3: Measurements of sky brightness temperature (thick line) and telescope count rates (dashed line taken at the HEGRA array on La Palma on the night of 24th September 2000. The count rate is taken every 16 seconds for CT6, which the KT 19 was mounted on.

testing the radiometer. Ethanol was the liquid chosen since it has a freezing point below $-100°$C, so is in no danger of freezing; it is a fairly innocuous substance as long as you avoid ingesting it; and there is a plentiful supply of both from the first year lab cloud chamber experiment. A metal can (such as an old [washed] bean tin) painted black makes a good approximation to a blackbody radiator. Such a can was filled with the alcohol and dry-ice mixture and the resulting temperature curve is plotted in figure 3.4. The temperature of the alcohol/dry-ice mixture was measured by an alcohol thermometer capable of going down to -100°C. Unfortunately it was difficult to maintain a temperature below $\sim -58°$C. The linearity of the KT 19 down to its scale temperature of -50°C can be seen, although the absolute accuracy of that value cannot be confirmed, due to the uncertain nature of the calibration blackbody.

3.6 Summary

The design and operating philosophy of the University of Durham Mark 6 imaging atmospheric Cerenkov telescope has been given. The telescope consisted of three 42 m^2 parabolic reflectors mounted on a single alt-azimuth mount. The trigger required a simultaneous signal from each of three detector packages facing the mirrors within a close (~ 10 ns) time window. The telescope and the surrounding environment were constantly monitored for calibration purposes, including the use of infrared radiometers to monitor

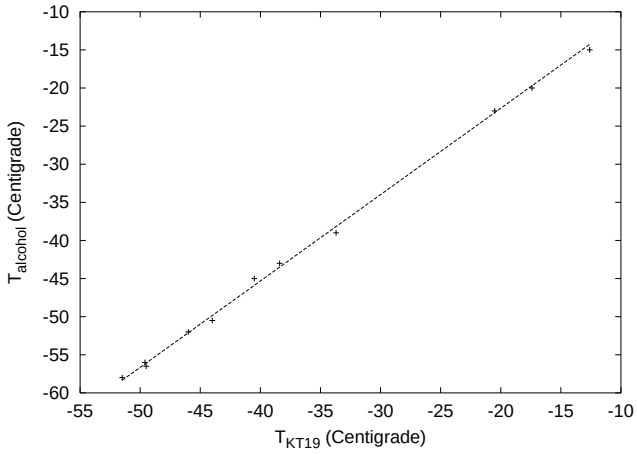

Figure 3.4: The temperature inferred by the KT 19 looking at a low temperature blackbody, compared to the recorded temperature of the dry ice in alcohol solution that is generating that temperature. The dashed line is a linear fit to the points.

the atmosphere in a quanitifiable and reproducible manner.

Chapter 4

Data Analysis Methods

4.1 Introduction

After the data has been calibrated and pre-processed according to the methods outlined in chapter 3.4 and the atmospheric conditions have been ascertained as clear and stable enough to allow further analysis it falls on the following methods to assign a statistical significance to any signal that may be found in the data. A statistical test is a rule that states for which values of random data, x, a given hypothesis (often called the null hypothesis, H_0) should be rejected. Rejecting H_0 if it is true is called an error of the first kind. The probability of this error to occur is called the significance level of the test, α, which is often chosen to be equal to some pre-defined value. It can also happen that H_0 is false and that the true hypothesis is given by some alternative, H_1. If H_0 is accepted in such a case this is called an error of the second kind. The probability for this to occur, β, depends on the alternative hypothesis, H_1, and $1 - \beta$ is called the power of the test to reject H_1.

4.2 Detecting a signal

It is the first priority to determine if there is a signal of VHE γ-rays from an object being observed. A γ-ray signal is determined as an excess number of events in the direction of the target source over that of an isotropic background of cosmic-ray events, i.e.

$$N_{\mathrm{xs}} = N_{\mathrm{on}} - N_{\mathrm{off}}$$

where N_{on} are the number of events on-source and N_{off} are the number of events off-source. The null hypothesis is that the number of excess events is just a statistical fluctuation of

the cosmic-ray background signal. Assuming that the number of air showers recorded by a telescope follows a Poisson distribution, the significance of any excess number of events between an on-source and off-source observation can be defined as [64]

$$\alpha = \frac{N_{\text{on}} - N_{\text{off}}}{\sqrt{N_{\text{on}} + N_{\text{off}}}} \tag{4.1}$$

provided that the on-source and off-source observations cover the same amount of time. As the flux of background cosmic-rays far exceeds the flux of γ-rays, achieving a significant excess of on-source events is a difficult challenge in a raw dataset: a significance in excess of 5 standard deviations ($\alpha \geq 5$) is the threshold generally used to identify a reliable detection [79].

Using timing information unique to the source of γ-rays was a widely used technique for signal detection in the early days of Cerenkov astronomy and some tests used in the search for a periodic modulation of a γ-ray signal are given in section 4.3. Not all sources exhibit a periodic modulation, though, and so the imaging technique was a real boon to the field of VHE γ-ray astronomy, allowing the detection of steady state and time varying (but non-periodic) sources like the Crab nebula and Blazars respectively. Table 4.1 provides the image parameter cuts employed in the analysis of data from Centaurus X-3, which will be met in chapter 5. An explaination of image cuts are given in chapter 2.5.1.

Parameter	Ranges	Ranges	Ranges	Ranges
size	800-1200	1200-1500	1500-2000	2000-10000
distance		$0.35^\circ - 0.85^\circ$		
eccentricity		$0.35 - 0.85$		
width	$< 0.20^\circ$	$< 0.23^\circ$	$< 0.28^\circ$	$< 0.32^\circ$
concentration	< 0.50	< 1.0	< 0.40	< 1.0
D_{dist}	$< 0.18^\circ$	$< 0.16^\circ$	$< 0.10^\circ$	$< 0.07^\circ$

Table 4.1: Full image parameter cut values for the Cen. X-3 data. The significance of a γ-ray signal is calculated using the excess number of counts (on-source − off-source) for events surviving these image cuts and having an $\alpha < 30^\circ$. Parameter *size* is given in digital counts.

The next requirement is to calculate the flux from an object, an important requirement for understanding the source energetics. The flux from a source is calculated from

$$F_\gamma = \frac{N_\gamma}{A_{\text{eff}} t_{\text{on}}} \tag{4.2}$$

where N_γ are the number of γ-ray events, $A_{\rm eff}$ is the effective collection area of the telescope and $t_{\rm on}$ is the amount of time spent on source. The number of γ-ray events is estimated from $N_{\rm xs} = \eta N_\gamma$, with η being the fraction of γ-ray events remaining in a dataset after any cuts to the data, to maximise the signal significance, have been made. Monte Carlo simulations put this fraction at $\sim 20\%$ of the γ-rays retained after rejection of $\geq 99\%$ of cosmic-ray events for the Mark 6 telescope [6]. If a significant excess of on-source events is not found then equation 4.2 can be used to calculate the upper limit of emission from a source; this being defined as the flux of γ-rays required to give an excess of $3\,\sigma$ from the dataset.

The effective collection area of a Cerenkov telescope is related to the energy of an event, the altitude of the detector, the Cerenkov light pool size and the triggering probability. It is then a good idea to estimate the absolute flux of γ-rays above a pre-determined energy threshold for a Cerenkov telescope to allow for comparison with other results. There is no consensus on the precise definition of threshold energy among the TeV community [71]. The scheme followed by the Durham group is to match the trigger rate of the telescope to Monte Carlo simulations of showers with energies in the range 100 GeV to 10^5 GeV for a source with a power law index of -2.6, corresponding to the differential spectral slope of local cosmic-rays. This yielded a threshold energy for the Mark 6 of 250 GeV for a telescope inclined at 20° to the zenith [6]. This has since been revised to 700 GeV for a telescope inclined at 30° to the zenith as a result of improved simulations of the telescope performance carried out by [75]. This is quite a large change in the estimate of the threshold energy, resulting from improved measurements being used in the modelling of the telescope, the atmospheric model used in the simulations (see chapter 6 as to how different atmospheric models affect the calculated effective collection area for a Cerenkov telescope) and through correctly cleaning the simulated data (see chapter sec:3,cal,noise).

4.3 Detecting a periodic signal: Frequentist Methods

The very small signal to noise ratio for VHE γ-rays makes a Fourier analysis difficult and has led to alternative methods being employed in searching for periodic signals. The first step in a period analysis is to reduce the data to a function of the period to exploit the circular, repetitive nature of a period P.

4.3.1 Epoch folding

The time of the ith event, t_i, from some arbitrary starting point t_0 will just be a certain number of cycles $n_i \times P$ from that starting point, the phase of that event time within the cycle is then just the non-integer part of the number of cycles. The phase of an event can then be seen to vary between $0 \rightarrow 1$ in terms of cycles, or you can picture it in terms of angles on a circle such that $0 \leq \phi \leq 2\pi$ where

$$\phi_i = \frac{2\pi t_i}{P} \bmod 2\pi$$

If there are any noticeable period derivatives ($\dot{P}, \ddot{P}$) the phases should be calculated by a Taylor expansion of the time series. Superimposing the series of times modulo the period will mean any recurring features will sum together to hopefully appear noticeable over the random background. This then allows us to compare the obtained signal to theoretical distributions.

The null hypothesis adopted is to test a signal against that of a uniform distribution of phase values, the kind of distribution one would expect if there was no periodic nature to a signal, just a random distribution of event times. This is because light curves can come in all manner of shapes and distributions, be they broad or narrow, sinusoidal or square. Any tests can and will be biased towards the kind of light curve being tested for. A non-periodic, uniform distribution, however, will always tend to the flat and so be easy to describe. By being able to reject a uniform distribution to a high degree of confidence is good evidence that a periodic signal is indeed present and the tricky problem of identifying the nature of that periodic distribution can begin. A false rejection of the null hypothesis can occur if the candidate pulse period of a source is a significant fraction of the duration of a time series. This is because a set of residual phases is automatically built up when the time series is folded. This problem can be avoided by truncating the time series to a length corresponding to the largest possible integer number of cycles.

4.3.2 Histograms and the χ^2 test

The simplest test to perform is to further arrange the time series in a histogram consisting of k phase bins each of width $\Delta\phi$ such that $k\Delta\phi = 2\pi$. A random time series will give a Poisson distribution of the number of events in the bins with a mean number per bin of $\lambda = N/k$, where N is the total number of events. The goodness of fit of the evaluated

signal to that of a constant, uniform signal is then

$$S = \sum_{j=1}^{k} \frac{(n_j - \lambda)^2}{\lambda}$$

where n_j are the number of events in the jth bin. S is distributed as χ^2 with $k-1$ degrees of freedom. For a perfectly even distribution $S = 0$, but as we are dealing with real distributions then S will tend to k for a random set of phases (as $n_j = \lambda \pm \sqrt{\lambda}$) so that a significant deviation from uniformity (i.e. evidence for a periodic signal) will correspond to $S \gg k$.

The histogram test suffers from several drawbacks. Firstly, the test is most sensitive to light curves with features of order $\Delta\phi \simeq 2\pi/k$. This means that the test is sensitive to the number of bins employed in the test. The ideal number of bins to be used depends on the shape of the light curve - which is often an unknown quantity. The stepwise nature of binning events in a histogram also means that the test is more sensitive to light curves with narrow features that serve to emphasise the distance to the mean value that is expected from a uniform distribution than the smoother, broader features of a sinusoid would, say. There is also the problem that fitting a large residual number of phases into a single bin can have a large effect on the resulting χ^2 value. The bin origin should be chosen such that as much of the peak of the phase distribution as possible lies within a single bin. If the light curve is split across two bins then the significance of a signal is decreased. As the absolute value of the phase is rarely known it is not always possible to fit the light curve in this way and any movement of the phase origin leads to an increase in the degrees of freedom associated with the test, which again serves to decrease the significance of any result.

The χ^2 test does not distinguish between a chaotic jumble of differing bin heights, to that of a smooth rise and fall that could be expected from a genuine light curve. A way around this is to apply a run test to the distribution of bin heights. A way of looking at this is to imagine flipping a coin 20 times. If the coin arrives heads up 10 times and tails up 10 times this is quite typical of a random behaviour, but if the coin lands heads up 10 times in a row and then tails up 10 times in a row this is less typical of a random process at work. One can then test the contiguous distribution of a series of histogram bins, by defining whether following bin values increase or decrease, to see how consistent the numbers are with a uniform distribution. In order to get a reliable estimate, the test needs to be applied on histograms containing at least 10 bins. A light curve will not necessarily follow a smooth distribution and may well contain multiple peaks, but if a

histogram has a saw-tooth up-down nature it could be that too low a harmonic of the period is being tested at.

4.3.3 The Rayleigh test

The Rayleigh test can overcome many of the difficulties inherent to the binning of data. Details of this test can be found in [69]. The time series is once more reduced to a series of phase values. Imagine the pulse phase interval $0 \rightarrow 2\pi$ corresponding to a circle (i.e. it wraps back round on itself every 2π). The individual phase values correspond to a direction on a circle. A resultant vector can be constructed by summing a series of vectors each of a unit arbitrary length and with a direction given by the phase value. If a particular value of phase is favoured by the distribution then the resultant vector will be large and have a pointing angle in the direction of that phase; conversely, if the distribution is random the individual vectors will act to cancel each other out and the resultant vector should be small. The horizontal and vertical components of the individual vectors are given by

$$\begin{aligned} x_i &= \cos(\phi_i) \\ y_i &= \sin(\phi_i) \end{aligned}$$

respectively and the resultant vector by

$$R^2 = \left(\frac{1}{n}\sum_{i=1}^{n}\cos(\phi_i)\right)^2 + \left(\frac{1}{n}\sum_{i=1}^{n}\sin(\phi_i)\right)^2 \tag{4.3}$$

The value $2nR^2$ is then distributed as χ^2 with two degrees of freedom and the asymptotic probability for $(nR^2 > k) = \exp(-k)$. For small numbers of events ($n < 50$) an approximate expression for the probability is needed [68].

The Rayleigh test is most sensitive to single peaked light curves, as any further peaks will add up out of phase and act to decrease the size of the Rayleigh vector (and therefore increase the resemblance to a uniform distribution). If a light curve has a bi-modal distribution with the interpulse being π out phase then folding at the half period will cause the peaks to add up in phase once more. This makes it important to test at both the period and the half-period if any bi-modality can be expected from the light curve, the only problem with this being that by increasing the number of tests performed the overall significance of a result will correspondingly go down.

Higher harmonics: the Z_m test

This test has been refined in an attempt to cope with multiple peaked light curves and those with significant power in the higher harmonics. This involves evaluating [50]

$$R_m^2 = \frac{2}{n}\sum_{j=1}^{m}\left[\left(\frac{1}{n}\sum_{i=1}^{n}\cos(j\phi_i)\right)^2 + \left(\frac{1}{n}\sum_{i=1}^{n}\sin(j\phi_i)\right)^2\right]$$

where m is the number of harmonics to be included. R_m^2 is distributed as χ^2 with $2m$ degrees of freedom. The Rayleigh test is then a special case of this family when $m = 1$, i.e. testing at the fundamental harmonic.

4.3.4 Testing a range of periods: the Fourier interval

Tests need to be performed over a range of periods rather than just at a single value. This can allow for any uncertainties in the expected period, due to uncertainties in the ephemeris for periods measured at other wavelengths (e.g. X-ray, radio), for any Doppler shift that may be introduced (such as orbital motion in a binary system), due to an irregular nature of the pulse period history, etc. The number of times a test is applied will affect the signficance of any result: the more times something is tested for the more likely it is to arise by chance, after all. It is necessary, therefore, to minimise the number of period values needed to be tested at in order to maximise the significance of a result, within reason.

In a time series of finite length there is a minimum difference between period values below which candidate periods are virtually indistinguishable, in the Rayleigh test testing two periods very close together will yield correlated resultant vectors. It is necessary then to know the minimum separation in period values needed in order to be getting truly independent tests. Let the first test period be P_1, the next independent test period be P_2 and the incremental step in period be δP. The phase of the last event in a time series of duration T is given by $\phi = T/P_1$; this phase will change with each incremental step to $\phi' = T/(P_1 + \delta P)$ until at P_2 the phase has moved round by one complete cycle and the new period is independent of the original period. The difference $\delta P = P_2 - P_1$ is known as the Fourier interval and can be found from

$$\begin{aligned} \frac{T}{P_1} - 1 &= \frac{T}{P_2} \\ \Rightarrow TP_2 - P_1P_2 &= TP_1 \\ \Rightarrow T(\delta P) &= P_1P_2 \end{aligned}$$

For $P \ll T$ then $P_1 P_2 \simeq P_1^2$ and the Fourier interval reduces to

$$\delta P = \frac{P_1^2}{T} \tag{4.4}$$

Whilst the Fourier interval represents the spacing between independent tests of the period, the maximum Rayleigh power (minimum Rayleigh probability) can still lie anywhere between the two values and so it is good practice to sample the period a given number of times between the independent periods. A value of three times per Fourier interval has been found to be best for the broad light curves that the Rayleigh test is best suited to searching for [50, 80]. It is important to account for this oversampling factor in the calculation of the number of trials performed when assessing the significance of any Rayleigh power found.

4.4 Detecting a periodic signal: Bayesian inference

One of the failings of the frequentist statistics previously summarised is the inability to deal with so called 'nuisance parameters' such as the uncertainty in the absolute phase of the time series or in the number of bins needed to describe the light curve. One of the strengths of a Bayesian analysis is to deal with nuisance parameters by integrating them out, a process known as marginalising. This comes about from the fundamental difference between Bayesian and frequentist thinking. A frequentist search assumes that a hypothesis is true and looks to see how well the observed data fits that hypothesis; a Bayesian looks to see which of a class of alternative hypotheses fits the observed data best.

In Bayesian inference the viability of each member of a set of hypotheses (H_i) is assessed in view of some observed data (D) by calculating the probability of each hypothesis, given the data and in light of any background information (I). The background information should, at the very least, specify the relation between the hypotheses and give some logical connection between the data and each of the hypotheses. The basic rules for the manipulation of Bayesian probabilities are the sum rule,

$$p(H_i|I) + p(\overline{H_i}|I) = 1$$

which signifies that should H_i prove false then an alternative hypothesis (or one of a series of alternative hypotheses) *must* be true; and the product rule

$$p(H_i, D|I) = p(H_i|I)p(D|H_i, I) = p(D|I)p(H_i|D, I).$$

The most important calculating rule in Bayesian inference - Bayes theorem - is found by equating the two right hand sides of the product rule to yield

$$p(H_i|D,I) = p(H_i|I)\frac{p(D|H_i,I)}{p(D|I)}. \tag{4.5}$$

The probabilities for the hypotheses in the absence of data, $p(H|I)$, are called the prior probabilities and the probabilities including the information from data, $p(H_i|D,I)$, are the posterior probabilities. The quantity $p(D|H_i,I)$ is the sampling probability for D, or the likelihood for H_i. The $p(D|I)$ is called the prior predictive probability and is the global likelihood for the entire class of hypotheses and acts as a normalisation constant.

4.4.1 Parameter estimation

The models used in astrophysics generally consider sets of hypotheses that are defined by the possible values of a continuous parameter rather than by discrete numbers. In this case one is examining probability densities as opposed to dealing with single probability values. If we have the background information for a parameterised model M with one parameter θ then $p(\theta|M)$ is the prior density for θ and $p(\theta|M).\mathrm{d}\theta$ is the prior probability that the true value of the parameter lies between θ and $\theta + \mathrm{d}\theta$. The global likelihood for model M can be calculated from

$$p(D|M) = \int p(\theta|M)p(D|\theta,M).\mathrm{d}\theta.$$

Models that contain more than one parameter can then be solved for using multiple integrals and this is how nuisance parameters can be dealt with.

Nuisance parameters

Whilst a model will often have many parameters, the attention will mostly be concentrated on a subset of those parameters; for example, testing data for a periodic signal independent of the concerns about the signal's amplitude, shape or phase. These nuisance parameters can be taken account of by merely integrating them out. If model M has two parameters θ and ϕ, but θ is the only parameter of interest it is a consequence of the sum and product rules that

$$p(\theta|D,M) = \int p(\theta,\phi|D,M).\mathrm{d}\phi.$$

The procedure of integrating out nuisance parameters is known as marginalisation and $p(\theta|D,M)$ is called the marginal posterior density distribution for θ. Marginalisation

also has the added bonus of acting as a kind of Ockham's Razor. Due to the need for integrating over the extra parameter space in more complicated models unless the data has a compelling effect on the likelihood ratio for a complicated model the simpler solution will always be favoured.

4.4.2 Model comparison

There is often more than one model available to explain a phenomenon, indeed Bayesian statistics requires that there be at least two competing models, even if this is just the case of saying the data is i) periodic or ii) non-periodic. It is perhaps easier to consider the ratio of the probabilities between two conflicting models rather than the probabilities directly. The odds ratio in favour of model M_i over M_j is

$$\begin{aligned} O_{ij} &= \frac{p(M_i|D,I)}{p(M_j|D,I)} \\ &= \frac{p(M_i|I)}{p(M_j|I)}\frac{p(D|M_i)}{p(D|M_j)} \end{aligned}$$

This means we can concentrate on the easier to define probabilities of how likely a model is to be true in light of all models and how likely the data is to fit each model, without having to worry about the more vague definition of the probability of the data arising in light of all models, which is the normalisation constant in Bayes theorem (equation 4.5). We can recover the probability for each model by inverting the odds ratio to give

$$p(M_i|D,I) = \frac{O_{i1}}{\sum_{j=1}^{N_{mod}} O_{j1}} \tag{4.6}$$

where N_{mod} is total number of models considered and $O_{11} = 1$.

4.4.3 The Gregory and Loredo method

The Gregory and Loredo method, detailed in [42] is a Bayesian treatment of determining whether a periodic signal exists in a dataset without any prior knowledge of the period or light curve shape. The method compares a constant model for the signal against members of a class of models with periodic structure. It assumes that any periodic structure in a signal can be represented by a stepwise function resembling a histogram with m phase bins per period. Using a sufficient number of bins can represent a lightcurve of essentially arbitrary shape. In this respect the method resembles the histogram technique of section 4.3.2, but with the ability to marginalise over the uncertainty in phase and bin number that afflicts that method.

The analysis relies on calculating the multiplicity

$$W = \frac{N!}{n_1!n_2!\ldots n_m!} \tag{4.7}$$

where N is the total number of events, $n_j(\omega, \phi)$ are the number of events falling into the jth of m phase bins, given the frequency ω and phase ϕ. The multiplicity, then, describes the number of ways that the binned data can be distributed. It is then just a matter of taking into account the prior probabilities for the period and phase range, light curve shape and event rate in order to allow a comparison to all of the models in order to see whether the data is distributed most like a random, uniform distribution of phase times or most like that of a periodic distribution.

Likelihood function for arrival time data

Let $r(t)$ describe the rate of events. The data are the arrival times, $D = t_i$ for each of N events ($i = 1$ to N) over an observing interval of total duration T. By dividing the observation into small time intervals we can work out the likelihood function for D from the Poisson distribution

$$p_n(t) = \frac{[r(t)\Delta t]^n \exp[-r(t)\Delta t]}{n!}.$$

Assuming that the rate does not vary substantially across the interval Δt the likelihood for an event D in the interval Δt is

$$p(D|r, I) = \Delta t^N \left(\prod_{i=1}^{N} r(t_i)\right) \exp\left(-\int_T r(t)\mathrm{d}t\right). \tag{4.8}$$

It then becomes a matter of evaluating the likelihoods for a constant event rate model to that of the periodic stepwise models.

The simplest model will have a constant rate of events, such that $r(t_i) = A$. The likelihood function for this model is then just

$$p(D|A, M_1) = \Delta t^N A^N \exp(-AT).$$

The models for a periodic signal are stepwise functions with a constant rate in each of m bins per period ($m \geq 2$). This is not a single model, but a class of models each with a different value of m. Each model M_m then has $m + 2$ parameters: a frequency ω (or period depending on your point of view); a phase ϕ specifying the location of the bins; and m sets of r_j values specifying the rate in each bin ($j = 1$ to m). It is perhaps better to express the r_j values as a function of a time averaged rate

$$A = \frac{1}{m}\sum_{j=1}^{m} r_j$$

with the light curve shape being described by a fraction of the total rate per period in each phase bin

$$f_j = \frac{r_j}{mA}$$

with the full set of f_j values denoted by $\mathbf{f}$ for brevity. The likelihood function then reduces to

$$P(D|\omega, \phi, A, \mathbf{f}, M_m) = \Delta t^N (mA)^N e^{-AT} \left(\prod_{j=1}^{m} f_j^{n_j} \right)$$

which in fact reduces to the uniform model if m is chosen to be 1, as expected.

Priors for periodic model parameters

Assuming there is no prior information linking the frequency, phase and light curve shape so that the priors for ω, ϕ and $\mathbf{r}$ are all independent of one another and that there is no prior information linking the shape of the light curve to its average value, the joint prior will be of the form

$$p(\omega, \phi, A, \mathbf{f}|M_m) = p(\omega|M_m)p(\phi|M_m)p(A|M_m)p(\mathbf{f}|M_m).$$

The prior densities are

- $p(\phi|M_m) = 1/2\pi$, this assumes any starting phase is equally likely allowing different observers with differing origins of time to reach the same conclusion.
- A similar invariance argument leads to $p(\omega|M_m) = \frac{1}{\omega ln(\omega_{hi}/\omega_{low})}$, where $[\omega_{hi}, \omega_{low}]$ is the least informative prior for the range of ω. This prior is form invariant, allowing investigators working in terms of frequency ω to reach the same conclusions as those working in terms of period P.
- $p(A|M_m) = 1/A_{max}$, this assumes that the average rate A does not change during the observation and any value of A from $A = 0$ to $A = A_{max}$ is possible.
- Subject to the constraint $\sum f_j = 1$ the fraction of the total rate in any bin can take any value between 0 and 1 with equal probability so
  $p(\mathbf{f}|M_m) = (m-1)!\delta(1 - \sum_{j=1}^{m} f_j)$, where δ denotes the dirac δ-function.

Priors for model comparisons

It is necessary to assign prior probabilities to each model in order to be able to carry out model comparison calculations. As the presence or absence of a periodic modulation is

equally likely a priori we can assign equal prior probabilities of 1/2 to each class. As the non-periodic class only contains the constant rate model ($m = 1$) this yields

$$p(M_1|I) = \frac{1}{2}.$$

The periodic class, on the other hand, consists of a finite number ($m = 2$ to $m_{\max}$) of stepwise models. Each member of this class is equally probable a priori, so the probability of 1/2 assigned to the periodic class is spread evenly across the $\nu = m-1$ stepwise models, so

$$p(M_m|I) = \frac{1}{2\nu}.$$

Whilst the prior probability of each model is equal, the need to integrate over an ever larger number of bins to gain the posterior probability allows Ockham's razor of simpler (fewer bin) models being favoured.

Odds ratio for periodic signal detection

Now that the priors and likelihoods have been worked out it is time to use this information in working out if a periodic signal is present. The probability for a model can be calculated from the odds ratios (section 4.4.2). The probability for the non-periodic model is

$$p(M_1|D, I) = \frac{1}{1 + \sum_{m=2}^{m_{\max}} O_{m1}}$$

and the probability for a periodic signal is the sum of the probabilities for the ν stepwise models

$$p(m > 1|D, I) = \frac{\sum_{m=2}^{m_{\max}} O_{m1}}{1 + \sum_{m=2}^{m_{\max}} O_{m1}}.$$

The ratio of these two equations gives the odds ratio, O_{per}, in favour of the hypothesis that the signal is periodic

$$O_{per} = \sum_{m=2}^{m_{\max}} O_{m1}. \tag{4.9}$$

When O_{per} is greater than 1 there is evidence for a periodic signal, with the magnitude of O_{per} indicating the strength of the evidence.

To calculate the individual odds ratios we need to calculate the global likelihoods $[p(D|M_m)]$ by integrating the prior and the likelihood for each model. The global likelihood for the non-periodic model is

$$\begin{aligned} p(D|M_1) &= \int_0^{A_{max}} p(A|M_1)p(D|M_1, A, I).\mathrm{dA} \\ &= \frac{\Delta t^N}{A_{max}} \int_0^{A_{max}} A^N \exp(-AT).\mathrm{d}A \\ &= \frac{At^N \gamma(N+1, A_{max}T)}{A_{max}T^{N+1}} \end{aligned}$$

where $\gamma(n,x)$ denotes the incomplete gamma function $\gamma(n,x) = \int_0^x y^{n-1}\exp(-y).\mathrm{d}y$. For the sort of data looked at in this work the period and phase of any periodic modulation is unknown. The global likelihood is then given by

$$p(D|M_m) = \frac{\Delta t^N (m-1)!N!\gamma(N+1, A_{max}T)}{2\pi A_{max}(N+m-1)!T^{N+1}\ln(\omega_{hi}/\omega_{low})}\int_{\omega_{low}}^{\omega_{hi}}\frac{\mathrm{d}\omega}{\omega}\int_0^{2\pi}\frac{m^N}{W_m(\omega,\phi)}.\mathrm{d}\phi.$$

Thankfully most of these terms cancel out when calculating the odds ratio for a specific model leaving

$$O_{m1} = \frac{1}{2\pi\nu\ln(\omega_{hi}/\omega_{low})}\frac{N!(m-1)!}{(N+m-1)!}\int_{\omega_{low}}^{\omega_{hi}}\frac{\mathrm{d}\omega}{\omega}\int_0^{2\pi}\frac{m^N}{W_m(\omega,\phi)}.\mathrm{d}\phi.$$

This can be worked out numerically and a recipe for the method is given in [42]. The Ockham factor $1/\ln(\omega_{hi}/\omega_{low})$, penalising the calculation for having an unknown frequency by marginalising over a range of frequencies, is akin to having to adjust the significance of a frequentist search by the number of independent trials searched. The difference is that where the frequentist significance is scaled linearly by the number of period values searched, the Bayesian method is only penalised by the actual range in period searched and not the number of individual values searched in that range.

The distribution O_{m1} vs m can provide valuable information on the underlying light curve for a periodic signal. The distributions for two differing light curve types are plotted in figure 4.1. Figure 4.1(a) is for a stepwise curve with seven bins, which the Bayesian test is able to identify correctly. Figure 4.1(b) is for a sinusoidal light curve. The broad, smooth shape of the sinusoid means that no particular model is significantly more likely than any of its competitors. The probability is then distributed over several model definitions. This echoes the way that the epoch folding and histogram method favoured narrow light curve types over broad, smooth light curve types.

If the odds ratio given by equation 4.9 gives reasonable evidence for a periodic signal being present, i.e. $O_{per} > 1$, then an estimation of the period can be made. When the period is known a priori (maybe from observations at another wavelength), but the shape of the light curve is unknown then the odds ratio in favour of the periodic class at that period, $O_{per}(\omega)$, can be made through equation 4.9 by using $p(D|\omega, M_m)$ in the place of $p(D|M_m)$. This is used to generate the periodogram of figure 4.2. This figure shows a periodogram for a simulated dataset of time-tagged events consisting of a periodic element in a uniform background. There are 1161 events in total, 129 of which belong to the periodic class. The periodic component has a lightcurve that covers 10% of the cycle and is periodic every 2.399 seconds, with a rate of 1 event being expected every

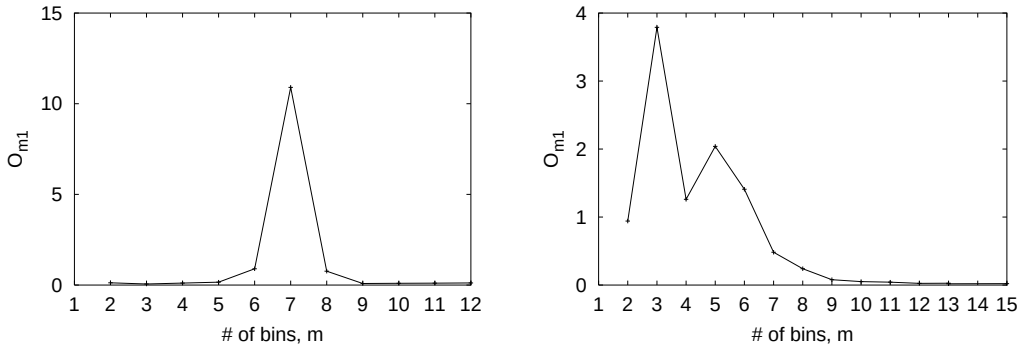

(a) 7 bin stepwise

(b) Sinusoidal

Figure 4.1: The odds ratios O_{m1} (in favour of an m bin stepwise model M_m over a uniform model M_1) vs m for two different underlying light curve types. The left hand figure is for a light curve containing a narrow, step feature of width $2\pi/7$ in phase; the right hand figure is for a smooth, broad sinusoidal light curve. From [42].

cycle. The entire simulated observation lasts ~ 325 seconds. The Gregory & Loredo test was performed for $2 \leq m \leq 20$ bins. Also plotted for comparison are the results from a Rayleigh test of the same dataset for comparison, with the chance probability for the Rayleigh result being given on the right-hand y-axis. Both methods select the correct value for the period, but it is the 'noise fluctuations' that are of the most interest. By taking account of the degrees of freedom from the start the Bayesian analysis creates an offset, suppressing the 'noisy' peaks below a value of 1, and so it is clear that there is only a single significant peak.

4.5 Summary

This chapter has dealt with the methods used to attach significance to, or draw inference from, data taken with IACTs. These methods generally take a null hypothesis that there is no γ-ray signal present and try to disprove this.

There are many methodologies that may be followed in order to test the hypothesis that a periodic signal is present in a dataset, the exact method that is chosen is very much dependent on the known, or more often unknown, characteristics of the light curve. The histogram test, whilst being deceptively simple, suffers from drawbacks in its sensitivity to the shape of a light curve and the value of the phase origin. Testing for unknown

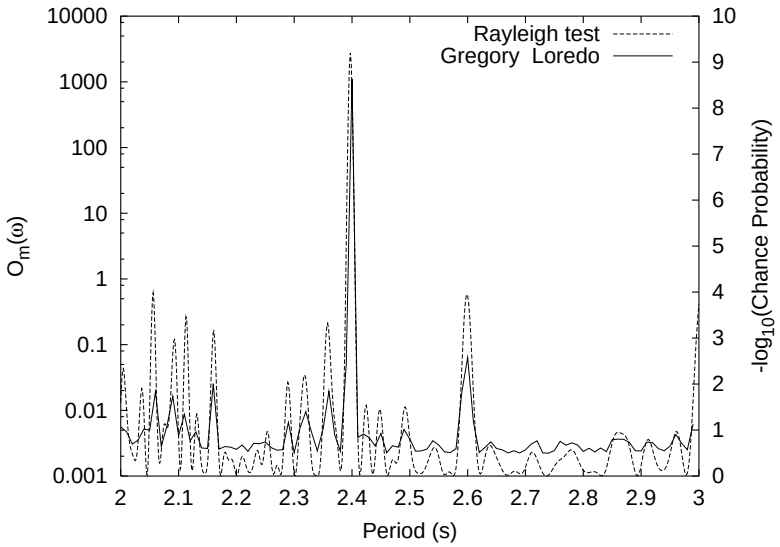

Figure 4.2: Odds ratio in favour of a period value, $O_m(\omega)$, as a function of period value for a simulated dataset of event times containing a uniform and periodic component. The periodic component is based at 2.399 s. Also plotted are the results of a Rayleigh test on the same dataset, with the -log$_{10}$(chance probability) of the peak occuring plotted on the right-hand y-axis.

values gives an increase to the degrees of freedom and being detrimental to the overall significance of a value for the period. This test is then best used when trying to fit a known light curve, one that has been measured at lower wavelengths, e.g. X-ray. The Rayleigh test is a good all round test to use, by not introducing the degrees of freedom that the binning of data can introduce, but it can fail when there are multiple features present in a light curve. This drawback can be overcome through the expansion of the Rayleigh test to higher harmonics.

The drawbacks to frequentist statistical methods usually come when dealing with nuisance parameters and when accounting for the number of trials performed in a test. A Bayesian way of thinking allows the marginalising of nuisance parameters and attempts to self-normalise for the number of trials at the start. This is due to the difference in thinking behind the two methodologies and whilst a Bayesian analysis may not assign a significance in the same manner that a frequentist test will, it allows important inferences to be made about a dataset.

Chapter 5

Centaurus X-3

5.1 Introduction

X-ray binaries are systems that consist of a compact object accreting matter from a main sequence star. The simple picture of these systems come in two main varieties: low mass X-ray binaries have a low mass companion star that has filled its Roche Lobe and is transferring mass to the compact object; a high mass X-ray binary has a high mass companion star and is accreting mass from the wind of the companion star. To demonstrate the fact that things are never simple Centaurus X-3 (Cen. X-3 from now on) is a high mass X-ray binary, but its luminosity is high enough to indicate the presence of an appreciable accretion disc indicating there is mass transfer from the companion star filling its Roche lobe.

Whilst X-ray binaries were a very fruitful source of TeV γ-ray detections in the early 1980's [25], these observations were carried out by non-imaging Cerenkov telescopes which had rather poor sensitivity and so γ-ray signals were extracted mostly on the basis of timing analyses, searching for modulation based at a pulsar period. Following the succesful use of an imaging camera to detect the Crab nebula as a steady source of VHE γ-rays [106], the reliability of the timing analysis results were questioned [107] with the non-detection of the first X-ray binary source Hercules X-1 with the Whipple IACT [89]. In fact Centaurus X-3 is the only X-ray binary to have a claimed detection as a faint, but persistent source of $E > 400\,\mathrm{GeV}$ γ-rays in the decade or so since imaging became an established technique [26, 30].

5.1.1 Centaurus X-3

Centaurus X-3 has been one of the prominent galactic sources of hard radiation since its discovery as one of the first cosmic X-ray sources [31], and was the first X-ray pulsar to be discovered in a binary system [40, 93]. All the basic parameters of this high mass X-ray binary have been well measured (for reviews see [54, 73]).

The orbital period of the system is $P_{\rm orb} \approx 2.1\,$days. The orbital period is decaying, probably due to tidal dissipation. The pulsar has a spin period $P_0 \approx 4.8\,$s, but the pulse period history of this object has a complex nature, shown in figure 5.1, with fluctuations on a general trend to shorter periods (i.e. 'spinning-up' of the neutron star due to angular momentum transfer from accreted material). The X-ray source has a deep eclipse between orbital phases $-0.12 \leq \phi \leq 0.12$. The X-ray luminosity of the pulsar reaches $L_{\rm X} \sim 10^{38}\,{\rm erg\,s^{-1}}$ in the 'high' state, but this is variable by up to a factor of 8 between the high and low states [108, 20]. This high luminosity and the trend for a spinning up of the neutron star imply disc-fed accretion in the Cen X-3 system rather than wind-fed accretion alone. The material accreted onto the neutron star originates from the optical companion [85, 60].

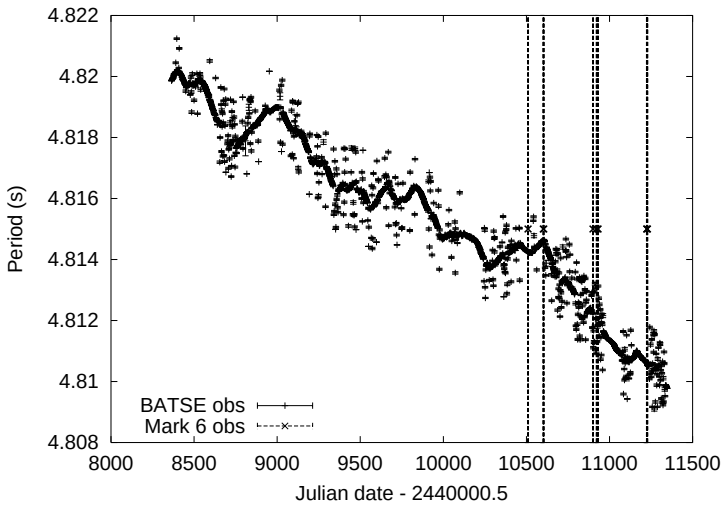

Figure 5.1: Pulse period history for Cen. X-3 as measured by BATSE. The dates of Mark 6 observations of Cen X-3 are marked by dashed lines also.

The optical companion (V779 Cen) was discovered by Krzeminski [59] and has been identified as an evolved O-type star with surface temperature $T \geq 3 \times 10^4\,$K at a distance $\sim 8\,$kpc from the Sun, and a bolometric magnitude of $M_{\rm bol} \sim -9$ [48]. The masses of the stars in this binary are estimated as $M_{\rm n} \simeq 1.2\,M_\odot$ and $M_{\rm O-star} \simeq 20\,{\rm M}_\odot$ [7]. The value

of the orbital period suggests the separation between the centres of the stars to be $a = 1.3 \times 10^{12}$ cm and the radius of the massive star filling its Roche lobe $R_{\rm O} = 8.6 \times 10^{11}$ cm [32, 7].

5.2 Previous high energy observations

5.2.1 Very High Energy γ-rays ($E \geq 100\,\mathbf{GeV}$)

Early observations

The early detections of sporadic VHE γ-ray signals from Cen. X-3 by the University of Durham [18] and the Potchefstroom groups [78] in the 80's were made with non-imaging Cerenkov telescopes and relied on timing analyses to produce a significant detection. Evidence for pulsed emission showed it to have sporadic, short timescale outbursts clustered around orbital phases in the region $\phi \sim 0.7$ to 0.8.

The Mark 6 observations

Cen. X-3 was observed by the Mark 6 between 1997 and 1999. The dates for which data passed threshold criteria for analysis (as described in chapter 3.4.7) along with the number of events that survive the image parameter cuts (given in table 4.1) for both the on- and off-source segments are given in table 5.1. The excess (γ-ray) signal has been found in the on-source data during each of the 3 years of observations, corresponding to an overall excess of 578 events for a total of 108 360 s of on-source data. The α-plot for the Cen. X-3 data following full image paramter cuts is given in figure 5.2 and shows an excess of on-source events for $\alpha < 30^{\circ}$.

The estimated mean γ-ray flux of $F(> 400\,\mathrm{GeV}) \simeq 2.8 \times 10^{-11}\,\mathrm{cm^{-2}s^{-1}}$ for the 3 year period, at a significance level for the entire data set of 4.7σ given in [30], has needed to be revised slightly. The increase in the estimate of the threshold energy for the Mark 6 telescope has already been discussed in chapter 4.2. Closer inspection of the data from this study also showed problems with one of the imaging PMTs for the nights of the 1st and 4th of June 1997, with tube 3C9 giving a permanent reading of 500 digital counts. After cleaning for this 'hot-pixel' the significance of the detection fell to 4.34 σ and the revised flux is

$$F(> 850\,\mathrm{GeV}) = (2.7 \pm 1.4_{\rm sys} \pm 0.6_{\rm stat}) \times 10^{-11}\,\mathrm{cm^{-2}s^{-1}}$$

Date	Number of scans	Events		Signal
	ON source	ON	OFF	significance
1997 March 1	4	446	401	1.55
1997 March 3	7	572	515	1.73
1997 March 4	4	383	319	2.42
1997 June 1	5	265	256	0.39
1997 June 2	6	455	383	2.49
1997 June 4	5	200	185	0.76
1997 June 5	5	323	295	1.13
1997 June 7	5	394	377	0.61
1997 total	41	3038	2731	4.04
1998 March 27	6	689	628	1.68
1998 March 29	7	661	589	2.04
1998 March 30	4	364	373	-0.33
1998 April 17	2	182	178	0.21
1998 April 19	4	339	336	0.12
1998 April 26	2	59	56	0.28
1998 April 27	11	473	441	1.06
1998 April 28	7	272	293	-0.88
1998 April 29	3	151	126	1.50
1998 total	46	3190	3020	2.16
1999 February 13	5	431	451	-0.67
1999 February 15	6	78	66	1.00
1999 February 16	11	923	902	0.49
1999 February 17	12	922	889	0.78
1999 February 20	3	206	212	-0.29
1999 February 21	5	355	294	2.39
1999 total	42	2915	2814	1.33
Total	129	9143	8565	4.34

Table 5.1: Observing log for observations of Centaurus X-3 taken with the Mark 6 telescope. The numbers of scans are after passing the $2.5\,\sigma$ test between on-source and off-source pairs. The numbers of events are after full image parameter cuts have been applied. Signal signficance is calculated from equation 4.1. The data for the nights of the 1st and 4th of June 1997 have had to be corrected for a 'hot-pixel' (see discussion in text).

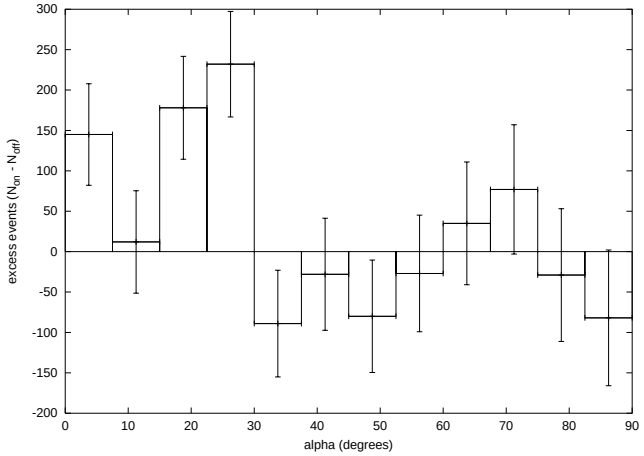

Figure 5.2: The α plot for the fully cut Cen. X-3 data from all observations. The excess γ-ray events cover a wide range of α below 30°.

assuming an effective collection area for the telescope of $A_{\text{eff}} \simeq 10^9\,\text{cm}^2$. Chapter 6 contains a discussion on how differing assumptions on the atmospheric models used in simulations of IACTs can affect the calculated effective collection area for a telescope and in turn how that changes the flux value calculated from the Cen. X-3 data set. The threshold energy is higher in the calculations for Cen. X-3 as the data is cut slightly higher in the *brightness* parameter to take into account the effects of a bright star close to the field of view.

Tests searching for modulation of the VHE signal at the X-ray period were made. The X-ray period was gained from either the BATSE[1] or RXTE ASM[2] publically available data. On some days values for the period were unavailable, either because the source was in eclipse or the X-ray flux was insufficient for the satellite instruments, so a value for the period was inferred by fitting a straight line through the nearest available dates that did have values for the period. No significant modulations in the combined on-source data with either the 2.1 d orbital period or 4.8 s pulsar period of the binary were found, but these data were analyzed after application of hard image cut procedures [30] which we shall see in section 5.4.2 can be very counter productive in a periodicity search. The lack of any evidence for a periodic signal would render the generation of a light curve on arbitrary parameters so a light curve was never produced in the analysis.

[1] http://www.batse.msfc.nasa.gov/batse

[2] http://xte.mit.edu/

5.2.2 High Energy γ-rays ($E \geq 100\,\mathrm{MeV}$)

The EGRET instrument detected Cen. X-3 as an emitter of HE γ-rays with a flux of $F(> 100\,\mathrm{MeV}) = (9.2 \pm 2.3) \times 10^{-7}$ photons $\mathrm{cm}^{-2}\,\mathrm{s}^{-1}$, significant at a $5\,\sigma$ level, during two weeks of observations in October 1994 [104]. There was no orbital modulation of the signal, with 68 of the 264 HE γ-rays being recorded during the pulsar eclipse region $|\phi| \leq 0.12$. The timing analysis showed a modulation of the HE signal with the BATSE inferred X-ray spin period by employing the H-test statistic [51] giving a chance probability of 1.6×10^{-3} after allowing for the degrees of freedom. The low number of events meant that generating a light curve for the HE γ-ray signal was not a practical proposition. The γ-ray signal was not found in the data of any other observing period, suggesting a variability of the HE γ-ray source on a time scale of several months.

5.2.3 X-ray

Centaurus X-3 is a strong X-ray source and so has been well studied by many X-ray satellite and rocket experiments. The emission is characterised by two states. The high/soft state is when the flux of low energy X-rays (typically 1 to 10 keV) resembles a blackbody curve and this is attributed to thermal emission from the accretion disc of the system. The low/hard state is when the spectrum is dominated by the higher energy bins and the spectral shape is that of a power law. Quasi-periodic oscillations have also been seen in the X-ray data from the Ginga [97] and RXTE [53] satellites, which have been interpreted as photon bubble oscillations [57], but are also observational features of microquasars.

The Burst And Transient Source Experiment (BATSE [81]) instrument onboard the Compton Gamma Ray Observatory (CGRO) provided near continuous measurements of the spin period between April 1991 and June 2000. The values were averaged over the 2 day orbit of Cen. X-3 provided the signal from Cen. X-3 was strong enough. Alternating extended episodes of rapid spin-up and spin-down superimposed on the long term trend for a spinning-up of the pulsar are clear from these data (see figure 5.1), showing the importance of having contemporary data at different wavelengths in the search for pulsar modulation in VHE γ-ray data. The light curve is usually single peaked, but is known to exhibit double peaked behaviour during the low/hard phase with the dominant peak being dependent on energy [101, 74, 20].

5.3 Models of high energy emission for X-ray binaries

Figure 5.3 sketches the various postulated emission regions in an X-ray binary and the wavelengths of radiation associated with those regions. Over the years many models have been envisaged as possible regions for the emission of high and very high energy γ-rays. All of these models have an intimate connection to the compact object itself, but at varying distances from this object due to observational constraints and the need to take into account the attenuation of the γ-ray population due to pair production on the thermal UV/X-ray photon fields present in the system. The more popular models are summarised here, starting from the compact object itself and working outwards from there.

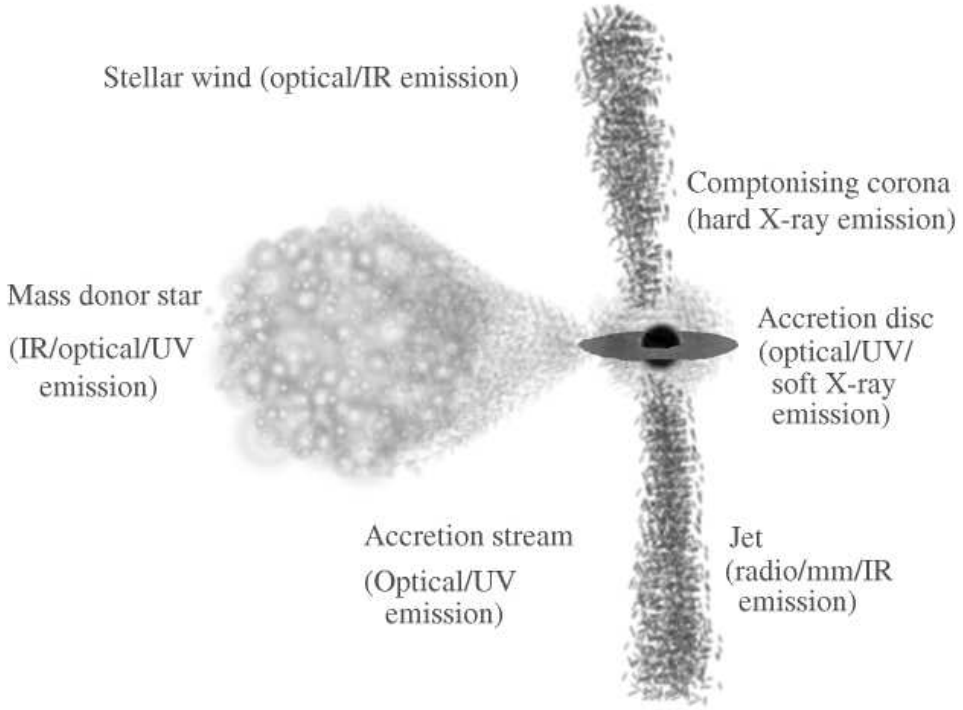

Figure 5.3: The various known emission regions present in an X-ray binary and their characteristic radiation. [37] has a more in depth discussion of these regions.

The compact object in an X-ray binary can take the form of a neutron star or a black hole. The compact object itself can only be the source of γ-radiation if it is a highly magnetic neutron star channeling accreted matter toward the magnetic poles. If the magnetic poles of the neutron star are not aligned with the rotation axis then the emission region can be seen to 'flick' across the line of sight leading to a periodic pulse of

emission in the now familiar pulsar model.

5.3.1 Emission from a pulsar

Figure 5.4 shows the two main contenders for HE emission from a pulsar. These models are known as the Polar Cap (PC) [43] and Outer Gap (OG) [90] models respectively after the region from which the emission is expected to come.

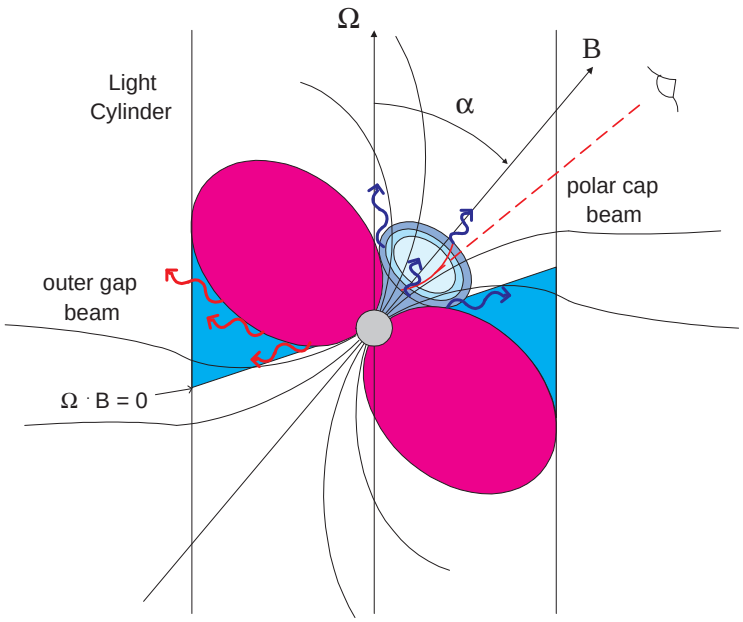

Figure 5.4: Pictorial representation of the Polar Cap and Outer Gap emission regions for pulsars. Obtained from http://cossc.gsfc.nasa.gov/images/epo/gallery/pulsars/

- The Polar Cap

  The strong magnetic field of a neutron star experiences a great amount of curvature at the magnetic pole. Charged particles following a trajectory along these field lines will radiate high energy emission as stated in chapter 1.3.3. The γ-ray spectra arise primarily from curvature radiation and are softened by synchrotron radiation from $e^{\pm}$ cascades generated from $\gamma\gamma$ annihilation [43].

- The Outer Gap

  A charge depleted gap can exist in the region where the magnetic field configuration changes from closed field lines to open field lines, generating a large potential difference across this area. An electromagnetic cascade can then result when the curvature radiation from close to the pulsar pair produces with the thermal X-ray

photons coming from the neutron star. The $e^{\pm}$ then radiate synchrotron radiation which can be inverse Compton scattered to VHE γ-rays [90].

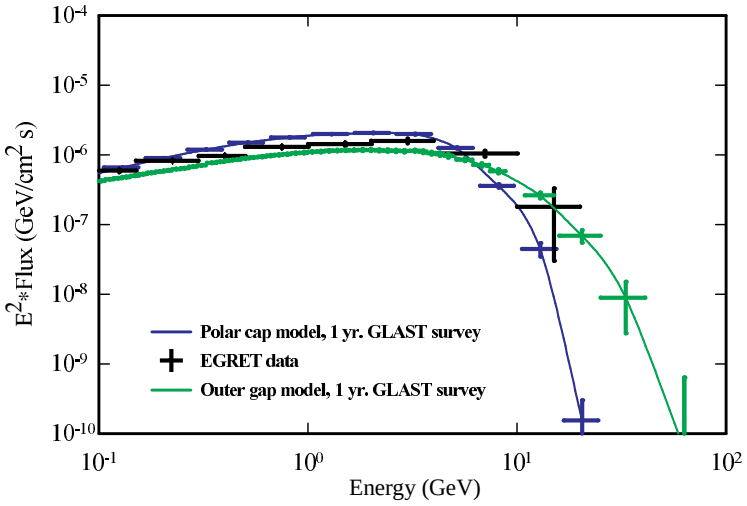

Figure 5.5: Discriminating between the pulsar γ-ray emission models. The spectrum of emission from the pulsar polar cap tails off more quickly than that from the outer gap. Also plotted are the data points from EGRET observations of γ-ray pulsars. Obtained from http://cossc.gsfc.nasa.gov/images/epo/gallery/pulsars/

The spectra from both of these models are expected to tail off in the 10 to 30 GeV region as shown in figure 5.5, with the Outer Gap model radiation surviving to higher energies than the Polar Cap. The ability to measure the spectra of pulsar emission in this region would be a major factor in discriminating between the two emission models. Whilst this energy limit is well below the present capabilities of IACTs, the Outer Gap model emission also predicts a component of emission peaking at around 1 TeV [90] due to the synchrotron self Compton mechanism from the $e^{\pm}$ pairs upscattering the 10^{-2} eV (IR) photons from the low end of the synchrotron spectrum, this should be detectable by IACTs.

5.3.2 Emission away from the compact object

The early observations of TeV radiation from X-ray binaries gave evidence that the site for VHE emission was not coincident with the site of X-ray emission:

(a) There was evidence for a frequency shift of γ-ray pulsations relative to the X-ray pulsations. This was most noticeably observed by three independent groups

observing a 0.16% offset of the VHE period to the X-ray period in Hercules X-1 charted over a three month period in 1986 [61, 88, 34].

(b) There were episodes of emission observed whilst the X-ray source was in eclipse, for example from Hercules X-1 [41] and Vela X-1 [77].

Most models for the generation of high energy radiation invoke a 'particle beam' from the neutron star interacting with gas of a sufficient density for π^0 production and their subsequent decay producing a γ-ray flux. This is also used to explain the episodic nature of pulsed VHE radiation seen from X-ray binaries, as the pressure from such a particle beam would act to heat and dissipate the target. The dense targets have been envisioned as 'clouds' or shocks in the radiatively driven companion star supersonic wind [1, 2]. If there is a tendency for VHE emission to show up at characteristic phases a more permanent target such as an accretion wake [87], or the limb of the companion star [67] (see figure 5.6) is invoked. These models for emission predict a hard spectrum of VHE radiation from X-ray binaries due to significant absorption on the thermal optical/UV photons produced either by the compact γ-ray source or from the radiation field of the companion star.

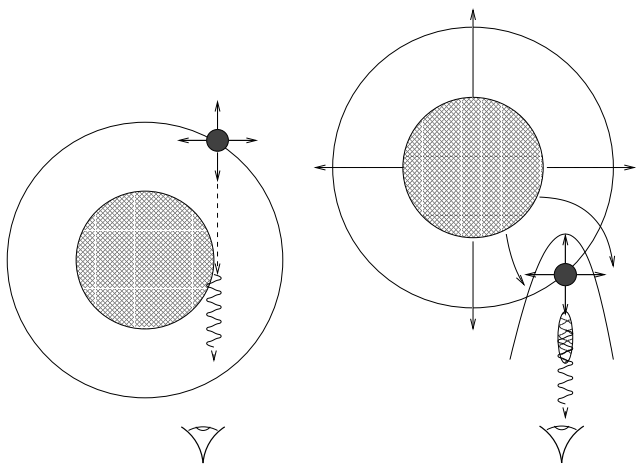

(a) Companion Limb (b) Accretion Wake

Figure 5.6: Generating γ-rays in an X-ray binary from a particle beam. 5.6(a) shows the beam interacting with the limb of the companion star. Emission is then expected close to eclipse phase. 5.6(b) shows the beam interacting with an accretion wake. The γ-ray site is then expected to trail the X-ray site.

5.4 Timing analysis of Mark 6 data for Cen. X-3.

5.4.1 Orbital Modulation

Bednarek [11] shows that the radiation field of V779 Cen should have a very marked effect on the propagation of γ-rays within the Cen. X-3 system. The optical depth for $\gamma\gamma$ annihilation varies from $\tau_{\gamma\gamma} \sim 10$ deep in eclipse ($|\phi| \leq 0.12$) to $\tau_{\gamma\gamma} < 1$ outside eclipse ($|\phi| \sim 0.5$). Mid X-ray eclipse is taken as corresponding to phase $\phi = 0$. If the γ-ray signal from X-ray binaries does not demonstrate any orbital modulation then it is a strong indication that the γ-ray source is displaced from the X-ray source on a spatial scale comparable with, or more likely exceeding, the size of the binary system ($\sim 10^{12}$ cm).

For calculations of the orbital phase the ephemeris of Nagase et al. [74] was used. This is in good agreement with the ephemeris of Kelley et al. [55] that was used in the earlier analyses of Cen. X-3 [26, 30], with only a 4% difference in the obtained orbital phase value by the 1999 data, but being more contemporary are more accurate and appropriate for this analysis. Since the length of observations varies from night to night and may reach several hours (i.e. a significant fraction of the ~ 2 day orbital period) the data for nights with a large (≥ 5) number of on-source segments were split into sequences of 3-4 on-source segments. This allows variations on a timescale of 1.5-2 hours ($\sim 4\%$ of the orbit) to be plotted. Figure 5.7 displays the VHE γ-ray signal with respect to orbital phase, after full image parameter cuts have been applied, as a function of γ-rays per cosmic-ray. This allows an assessment of the strength of a possible γ-ray signal independent of the daily variations of the performance of the telescope. The image parameter cuts are given in table 4.1 and are identical to those in [30]. Note that there is a deficit in the number of observations in the phase range $-0.5 \leq \phi \leq -0.3$. For all other phases the γ-ray signal is distributed quite homogeneously.

5.4.2 Pulsar spin modulation

The previous timing analysis [30] of the Cen. X-3 data set found no evidence for modulation of the VHE γ-ray signal at the pulsar period in either the total data set or on a night by night basis. The tests were performed over a narrow range of period values (2-3 Fourier intervals) around the BATSE determined X-ray period after focusing the event times to the site of X-ray emission (see chapter 3.4.9 for information on focusing). The lack of a positive detection of periodicity is not surprising for several reasons.

The lack of orbital modulation of the HE and VHE γ-ray signal is an indication that

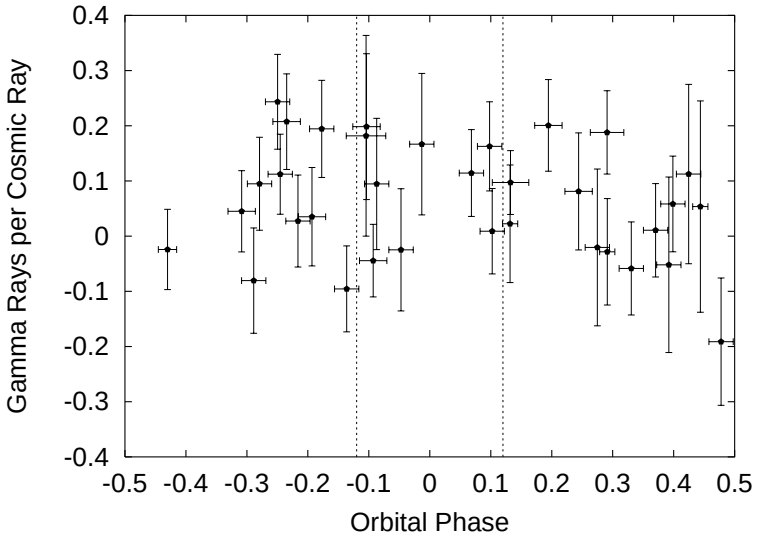

Figure 5.7: The numbers of γ-rays per cosmic-ray with respect to orbital phase for the Mark 6 telescope Cen. X-3 data set after full image parameter cuts have been applied. The eclipse phase is marked by dashed lines with mid-eclipse being phase 0. If the γ-ray source is coincident with the X-ray source a significant orbital modulation should be observable.

the site of γ-ray production is not coincident with the site of X-ray production. This means that whilst any pulsed signal could be modulated at the X-ray frequency, it could be significantly Doppler shifted from the characteristic X-ray frequency. Searching a narrow band of periods around the X-ray period would mean that any true modulation of the γ-ray signal could be missed. Focusing of the event times to the site of X-ray production would not be a good idea either.

This work therefore conducted a search for a periodic γ-ray signal in a wider bandpass around the X-ray period $P_0 \simeq 4.81\,\mathrm{s}$. The search was conducted both around the period, $4.79 \leq P \leq 4.83$ seconds, and the half period, $2.395 \leq P/2 \leq 2.415$ seconds, due to the insensitivity of the Rayleigh test to light curves with a double peak separated by π in phase and knowing that the Cen. X-3 X-ray light curve occasionally shows such bimodal behaviour. The time range tested corresponds to a Doppler shift of up to $v \sim 1200\,\mathrm{km\,s^{-1}}$ after the theoretical expectations of [2]. This compares to the orbital speed of the pulsar of $414\,\mathrm{km\,s^{-1}}$ [7] and the speed of the wind driven by the optical companion at $v_{\mathrm{wind}} \sim 1000\,\mathrm{km\,s^{-1}}$ [32]. The event times were not focused to the pulsar position; given the wide range in period searched any significant modulation found could easily be compared with

the Doppler shifted period of the X-ray pulsar at the known orbital phase.

The periodicity tests were applied to each night's data individually. As the source of VHE γ-rays is unlikely to be associated with the X-ray site due to the lack of orbital modulation, it is quite possible that the γ-ray emission site is not contained and therefore pulsed emission could be for short timescales only, perhaps corresponding to bursts or 'flares' of emission. Signal coherence [63] was assumed within a night's observation, but not between nights for much the same reasons; there is no established long term phase coherence at TeV energies for Cen. X-3 and the X-ray period fluctuates randomly as seen from the BATSE data (figure 5.1). Any flaring behaviour of Cen. X-3 is unlikely to last longer than the time that a night long observation would cover - a typical observation of Cen. X-3 lasts for $\Delta t_{\rm obs} \sim 3$ hours. The chosen range of trial periods then corresponds to $\sim 18 - 19$ Fourier intervals around the fundamental harmonic and about twice that for the half period search.

A search through all of the full image parameter cut data yielded no significant sign of modulation either at the main period or at the second harmonic. This is the result one could expect, indeed no evidence of a periodic signal from an X-ray binary has been seen since the advent of imaging. This, however, does not conclusively prove there is no actual periodic modulation to the signal.

The need for soft cutting

One also has to consider the robustness of the test statistic being applied to the data. The statistical significance of a d.c. signal in the data, calculated through equation 4.1, is maximised by cutting the raw data set to reduce the background signal. Any cuts made to the data will affect the number of both background, $N_B^{\rm cut} = F_B N_B$, and γ-ray events, $N_G^{\rm cut} = F_G N_G$, where F_B and F_G are the respective fraction of events surviving cuts. Cutting data on air shower image parameters is a useful technique for background signal suppression as F_G can be $\gg F_B$. The cuts made, however, do need to be harsh in order to get the best signal to noise ratio as $\sigma \propto F_B^{-1/2}$. The harsh nature of the cuts will inevitably lead to a loss of γ-ray events from a dataset. Simulations of the Mark 6 telescope indicate that after rejecting $> 99\%$ of cosmic-ray background events only $\sim 20\%$ of the γ-ray events are retained [6]. In a search for d.c. emission this is acceptable, since merely increasing the observing time will lead to an increase in the number of γ-rays in a dataset. In a periodicity search – especially if the episodes of pulsed emission are short term and when combined with a low flux of VHE γ-rays – any loss of γ-ray events could prove fatal to a

positive detection. The mean flux from Cen. X-3 is just $\simeq 2.7 \times 10^{-11}$ photons cm^{-2} s^{-1}. Combine this flux with the effective area of the telescope and if only 20% of the events survive beyond cutting then there could only be $\sim$ 30 pulsed γ-rays at most from an average night of 1.5 hours of on-source data (given the very unlikely assumption that the signal is 100% pulsed). This is far less than the 40 to 50 events needed for a successful practical application of the Rayleigh test, given the impact of statistical fluctuations.

Whilst it is reasonable to reduce the number of cosmic-ray events in a dataset, the priority in a periodicity search is to maintain the maximum number of γ-ray events. In order to achieve this the image parameter cuts were relaxed:

- The range of α was extended such that $\alpha \leq 45^{\circ}$. This process reduces the number of cosmic-ray events by a factor of ~ 3 from the raw data set, but does not significantly affect the number of γ-ray events. It also takes into account the very wide α plots seen in Mark 6 data, see figure 5.2, a feature that may be connected to geomagnetic field effects on the propogation of extensive air showers [28, 29].

- The cut on *concentration* was dropped. The blur from the Mark 6 mirrors is such that this cut has no significance on simulated datasets [75] and whilst there is an increase in significance for observed data there is no sound basis for including this cut.

- The cut on $D_{\rm dist}$ was dropped. It is this cut that is harshest on the γ-ray candidate events. Due to the very stringent limits used to gain any increase in significance for d.c. observations up to 60% of γ-ray events are removed [94].

The *distance* and image shape cuts (*width*, *eccentricity*) were kept, as these cuts are very effective at reducing the cosmic-ray signal (by a factor of 8-10) whilst removing very few γ-ray events. There was one further sub-division of this 'soft-cut' dataset by discriminating on the *brightness* of events; taking one dataset having events with *brightness* $\geq$ 800 and another of *brightness* $\geq$ 1500 only. This effectively increases the energy threshold of the telescope by a factor of $\sim$ 2, therefore it is only efficient in the analysis if the γ-ray spectrum is much harder than that of the cosmic-rays. This idea stems from the theoretical predictions that the γ-ray spectra from X-ray binaries will be hard due to significant absorption on thermal optical/UV photons from either the companion object [11] or the compact γ-ray source itself [1, 2]. As expected the use of raw and soft cut data does not give any direct evidence of emission, as evidenced by their α-plots in figure 5.8(a)

and figure 5.8(b) respectively, as there is no significant excess at low values of α; but it is the effect on the timing analyses that is of interest.

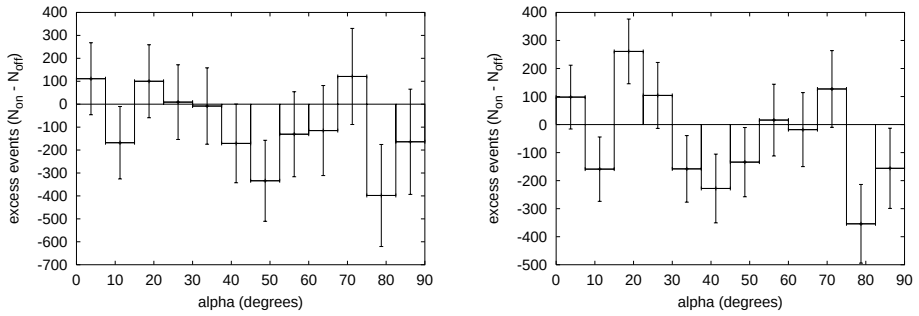

(a) raw data (b) soft cut data

Figure 5.8: α plots for raw and soft cut Cen. X-3 data.

Only one night of observation gave a strong Rayleigh power peak, being present in a soft cut *brightness* $\geq$ 1500 data subset. The observation taken on 21/2/99 gave a peak of 13.5 corresponding to a chance probability of 1.4×10^{-6} at a period of 2.399868 seconds. This is blue-shifted by 0.37% from the nominal second harmonic of the BATSE deduced spin period ($P_0/2$ = 2.408785 seconds after correcting to an orbital phase of $\phi \simeq -0.235$ for the time of observation). This implies a motion of the γ-ray source (if true) at a velocity of $\sim 1100\,\mathrm{km\,s^{-1}}$ with respect to the neutron star. Figure 5.9 shows the periodograms obtained for the fully-cut, soft-cut with *brightness* $\geq$ 800 and soft-cut with *brightness* $\geq$ 1500 data sets respectively. The progression of the signal from a complete absence in the fully cut data to a weak signal in the soft-cut dataset to a strong signal in the dataset cut assuming a hard spectrum for the γ-ray signal can be clearly seen. Unfortunately, preparing the datasets with so many assumptions comes at a price: widening the period range gave 19 Fourier intervals at the first harmonic and twice that at the second harmonic; the factor 3 oversampling between the Fourier intervals; and the preparation of three differently cut data sets for each of the 23 days. This means the number of trials for the Rayleigh analysis is $N_{\mathrm{trials}} \leq 11\,800$ which takes the probability of the Rayleigh peak arising by chance from 1.4×10^{-6} up to 0.01652, or roughly 1 in 60. The multiple peaks are also faintly reminiscent of the pattern given by the combination of weak, incoherent signals or noise masquerading as a coherent signal due to the gapped nature of the chopped observation mode [63]. Whilst this is unlikely to have an effect on such a short timescale observation, this being more applicable to testing the data for

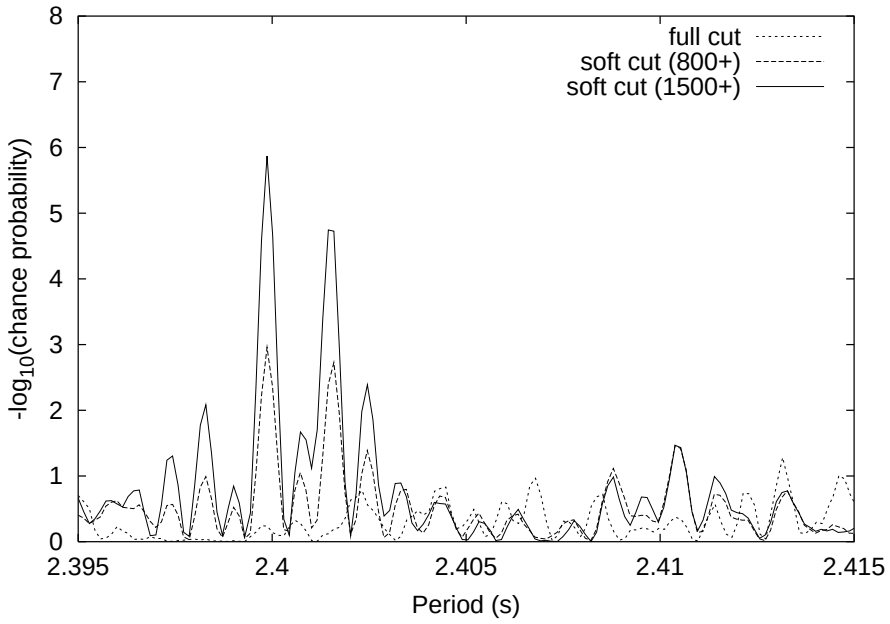

Figure 5.9: Rayleigh test periodograms for 21/2/99. The test was performed at the half period (in case of multiple peaks in the light curve) for data that had been fully cut (dotted-line); soft-cut with *brightness* $\geq$ 800 (dashed line); and soft-cut with *brightness* $\geq$ 1500 (solid line).

several nights that have been joined together, it cannot be discounted at present.

The Rayleigh test suffers from having to account for the number of trials after the test has taken place, but through a Bayesian analysis it is possible to factor these in to the analysis from the start.

Bayesian periodicity analysis

In order to gain better control of the hypothesis testing the analysis was repeated using the Gregory & Loredo Bayesian technique (see chapter 4.4.3). Through the marginalising of 'nuisance parameters' this method shares the advantage of not needing to know the absolute phase that the Rayleigh test enjoys. The Gregory & Loredo technique also automatically normalises its results to the range of period values examined, allowing as many period values within that range to be examined as necessary without affecting the overall result. The Gregory & Loredo method can also cope with gaps in the time series of the data stream [42].

The first test needed is to establish if there is reasonable evidence for a periodic signal in the first place. The light curves of accreting objects are expected to be broad

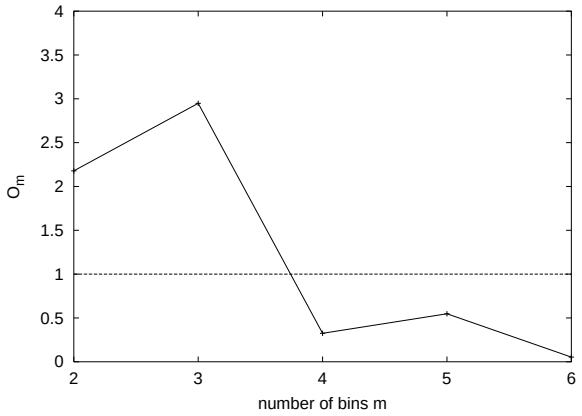

Figure 5.10: Odds ratio in favour of periodicity for an m bin model as a function of m for the data taken on the night of 21/2/99. The dashed line shows the threshold, $O_m = 1$, after which their is evidence for a periodically modulated signal.

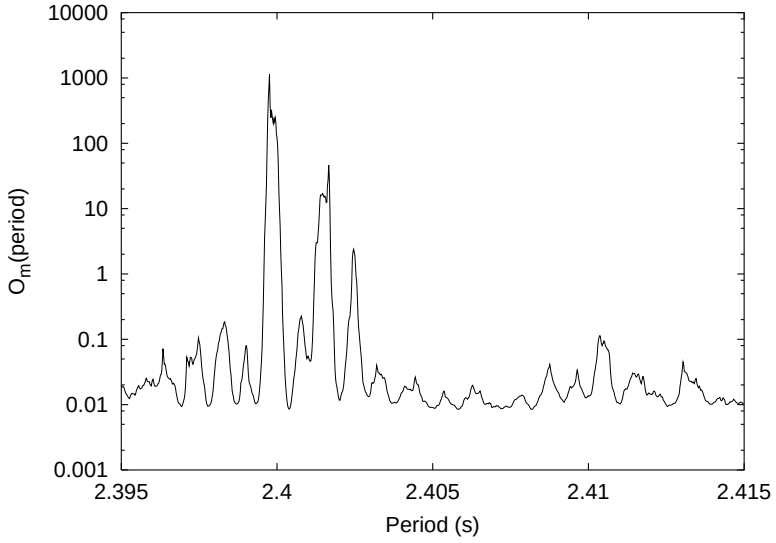

Figure 5.11: The odds ratio in favour of period P for the soft cut *brightness* ≥ 1500 data in figure 5.9. Any value $O_m(\omega) > 1$ is an indication of periodicity at that value of the period. The odds ratio value is plotted on a logscale.

and roughly sinusoidal in shape. Light curves of this shape have power in a number of stepwise models, but as figure 4.1(b) shows, one need only test up to $m = 6$ to gain the maximum likelihood of detecting periodicity. Figure 5.10 plots the odds ratio for a model of m bins as a function of m for $2 \leq m \leq 6$; this graph indeed mimics that of the sinusoidal light curve data given in figure 4.1(b), albeit at a diminished level. The overall probability in favour of a periodic model over a constant rate model is only $\sim 86\%$ (calculated from equation 4.6) after integrating over the whole 2.395 to 2.415 second period range. Whilst not conclusive this is a good indication of a modulated signal being present, especially when taking into account that the Gregory & Loredo method is not optimal for detecting pulsations from smooth light curves [42]. As such, it was worth continuing to calculate the odds ratio in favour of a particular period value P, given in figure 5.11, and compare this to the results obtained in the Rayleigh test analysis. Remembering that any value of the odds ratio above 1 is an indication of periodicity at that value of P we see the shape of the periodogram generated in the Rayleigh test analysis generated once more, again with two peaks being of particular note. The larger of the two peaks corresponds to an odds ratio of 1130 to 1 in favour of modulation at a period of 2.399760 seconds.

Two peaks?

One of the striking features of the periodograms for the data of 21/2/99 is that there are two peaks apparent in the data, close to each other, but clearly separate. The phase at the start of the observation is $\phi = -0.257$ and at the end is $\phi = -0.212$ which corresponds to a change in the unfocused pulsar period of 8.9×10^{-5} s, which is smaller than the Fourier interval for the observation (F.I. $\simeq 1.07 \times 10^{-3}$ s). The time difference between the two peaks from the Rayleigh test is 1.6×10^{-3} s and for the Gregory & Loredo method is 1.8×10^{-4} s; both of these are larger than the Doppler shift from orbital motion of the pulsar. The Gregory & Loredo analysis was performed at period intervals a factor of 10 smaller than for the Rayleigh test, as the Bayesian method is unaffected by the number of period values examined, so it is not unexpected to see a smaller difference between the period values for the peaks than in the Rayleigh test. As the two peaks are obviously not a facet of the orbital motion of the pulsar it is of interest to know if those two peaks are present all the way through the dataset, if they represent two different episodes of pulsed emission, or if they are a characteristic of the motion of the γ-ray source. The periodic tests were re-applied to a smaller section of the time series of the 21/2/99 data and allowed to slide through the whole night's observation. Since a single night of data

represents a very small sample of γ-ray events in the first place any further subdivision of a night's data means that it is difficult to gain any significant insight, but the indications are that the minor peak represents emission early on in the observation and the stronger peak represents a stronger burst of pulsed emission later on in the observation.

5.4.3 Generating a light curve

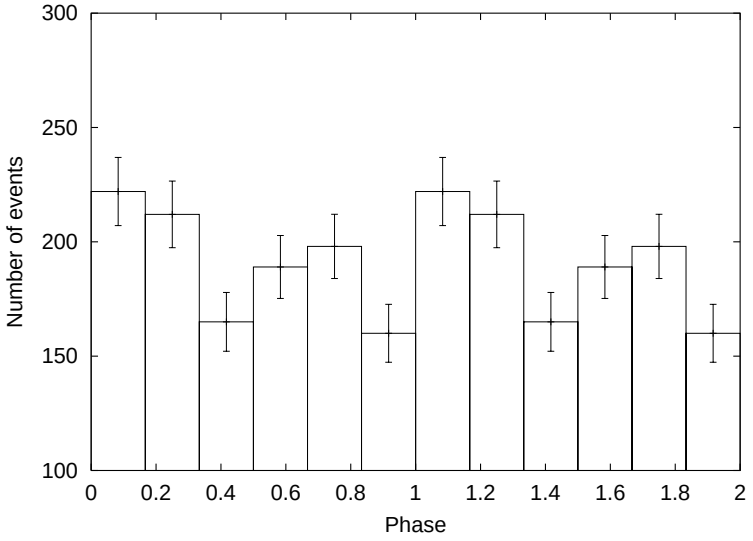

Figure 5.12: Light curve for 21/2/99 Cen. X-3 data.

Once a candidate period for pulsations has been identified a light curve can be constructed. The light curve for the 21/2/99 soft cut, *brightness* > 1500 dataset is shown in figure 5.12. The curve is folded into 6 phase bins at a period of 4.79952 seconds (corresponding to twice the best value for the Gregory & Loredo analysis) and the phases adjusted by 0.066132, which corresponds to the best value of phase found through marginalising in the Gregory & Loredo analysis. The curve gives a χ^2 value of 16.19, which gives a confidence of 99% that the data is non-uniform, although nothing can actually be said as to whether the periodicity is actually related to the pulsar. As can be seen the curve demonstrates a double peaked behaviour, though the peaks seem highly asymmetric. This is not dissimilar to the pulse profile of Cen. X-3 as seen by GINGA in certain X-ray wavebands and seems related to the appearance of the smaller interpulse [74].

5.5 Implications to X-ray binary models of high energy photon production

The results of observations of Cen. X-3 in both the high energy regime with EGRET and the very high energy regime with the Mark 6 provide stringent limits on the models of γ-ray production in this X-ray binary. The presence of a very luminous star close to the pulsar would lead to a significant absorption of the γ-ray photons on the optical/UV photons from the companion prior to escaping the system. The absence of an orbitally modulated signal from the EGRET and the Mark 6 data indicates that the γ-ray source cannot be in close proximity to the neutron star. This result can reasonably exclude any model that assumes the γ-ray flux from this object is due to the production of γ-rays directly by the pulsar or invoking the accretion disc around the neutron star directly. At the same time, however, the γ-ray source must be inherently connected to the neutron star from the general consideration of source energetics.

The γ-ray flux detected by EGRET in 1994 corresponds to a source luminosity of $L_\gamma(100\,\mathrm{MeV} \leq E \leq 10\,\mathrm{GeV}) \simeq 5 \times 10^{36}\,\mathrm{erg\,s^{-1}}$ and the mean flux of VHE radiation detected by the Mark 6 during 1997-1999 corresponds to a source luminosity $L_\gamma(> 850\,\mathrm{GeV}) \sim 10^{36}\,\mathrm{erg\,s^{-1}}$. The parent relativistic particles generating these photons must inevitably have energies of at least $10^{37}\mathrm{erg\,s^{-1}}$. The luminosity of the companion star V779 Cen is really high, corresponding to a bolometric luminosity of $L_{\mathrm{bol}} \simeq 10^{39}\mathrm{erg\,s^{-1}}$. Could the conversion of a small fraction of this luminosity into the acceleration of relativistic particles, by the generation of shocks in the supersonic radiatively driven wind for instance, be responsible? The characteristic speed of the stellar wind is $v \sim 10^3\mathrm{km\,s^{-1}}$ and the mass-loss rate $\dot{M} \sim 10^{-6} M_\odot\,\mathrm{yr^{-1}}$ means that the kinetic energy available in the wind gives a power of only $\sim 10^{35}\mathrm{erg\,s^{-1}}$.

The neutron star itself cannot be responsible and so the remaining principal option for the prime energy source for the acceleration of relativistic particles has to come from the kinetic energy of the inner accretion disc formed around the neutron star. Most of the kinetic energy of the disc ends up on the neutron star surface in the form of the thermal energy plasma responsible for the X-ray luminosity, which reaches $L_{\mathrm{X}} \geq 10^{38}\mathrm{erg\,s^{-1}}$ in the high state. It is possible, however, that a significant fraction of the accretion disc energy can be ejected from the system in the form of powerful outflows seen as jets. These are observed in the class of close X-ray binaries described as micro-quasars (see [70] for a review). An example of a microquasar containing an accreting neutron star that

produces powerful sub-relativistic jets is SS 433, with the jet kinetic energy estimated in the range $\sim 10^{39}\mathrm{erg\,s^{-1}}$ [82]. Recent work has been able to explain the low-hard states in the majority of X-ray binaries in the framework of jet models [37, 38]. The observational implications for the presence of jets in Cen. X-3 will now be explored, with full details of the modelling involved to be found in [10].

5.5.1 Spatially extended source model

Jets propagating through the dense wind driven by the companion star would create strong shocks. The subsequent acceleration of particles in these shocks could result in the creation of a γ-ray source around the region of jet propogation on large spatial scales that would be comparable with, and probably exceed, the scale size of the binary system of $l_s \sim 10^{12}\,\mathrm{cm}$. This model automatically favours a leptonic model for the generation of γ-rays since any hadronic model gives a source luminosity several orders of magnitude below the detected γ-ray luminosity and would require unreasonably large densities of material in the system to generate the observed fluxes [10]. A leptonic model would then have a scale size somewhere between $10^{12}\,\mathrm{cm} \leq l_s \leq 10^{14}\,\mathrm{cm}$ with the upper limit being given due to the fast decline of the density of the UV photon field from the O-star, which essentially reduces the efficiency of the IC γ-ray production (as $t_{\mathrm{IC}} > t_{\mathrm{esc}}$). Figure 5.13 plots the spectrum expected from a spatially extended source model. The heavy dashed line shows the spectrum escaping the source and the heavy dotted line shows the flux that would be expected if the escaping flux were generated at the pulsar orbit. The hatched regions correspond to the fluxes observed with the Mark 6 at TeV energies (calculated for differential power law indices in the range $2 \leq \alpha_\gamma \leq 3$) and the range of differential fluxes (from median to low) with EGRET at GeV energies.

The large scale size of the source suggests that the γ-ray source is quasi-stationary on time scales of ≥ 1 day and possibly even weeks. This model is unable to explain the presence of modulations of the γ-ray signal at the pulsar period, for which the source characteristic scale size needs to be $l_s < cP_0/2 \leq 5 \times 10^{-10}$ cm in order for the pulsations to be present.

5.5.2 Compact source models

If pulsations based at the pulsar period are to be explained they must be in the framework of a compact source. Whilst we have already noted that the effective source radius needs to be less than the light crossing time at the pulsar period it is also a requirement that

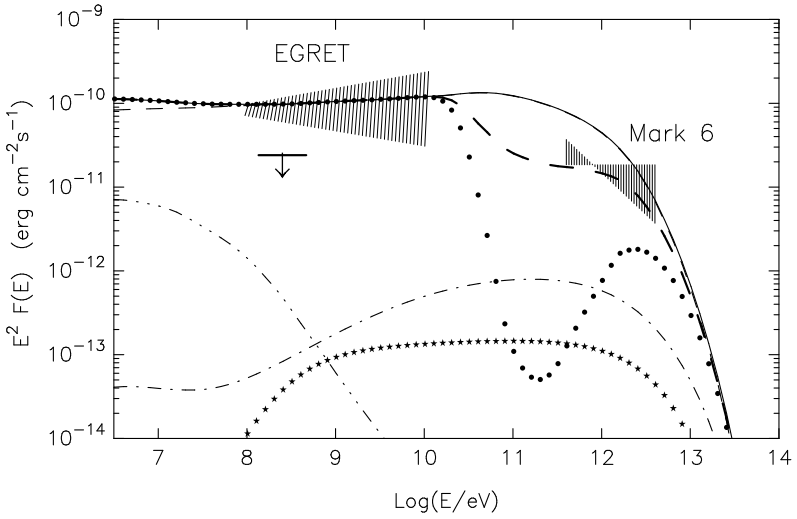

Figure 5.13: The spectra of IC γ-rays calculated for the spatially extended source. Contributions to the total unabsorbed IC radiation (solid line) due to upscattering of the UV radiation of the companion O-star (thin dashed line; distinguished only at $E < 10^8$ eV), X-ray pulsar photons (3-dot–dashed line) and synchrotron photons (dot-dashed line) are shown. The heavy dashed line shows the spectrum escaping the source. The heavy dotted line shows the fluxes that would be expected if the same unabsorbed radiation were produced at the pulsar orbit; the stars show the unabsorbed radiation of hadronic origin (see text). The hatched region at TeV energies corresponds to the average flux detected by the Mark 6 telescope during 1997 [30] calculated for differential power-law indices between $\alpha_\gamma = 2$ and 3. The range of differential fluxes, from median to low, detected by EGRET during October 1994, as well as the upper flux limit for an earlier observation period, are also shown. Taken from [10].

the energy loss time $t_{\rm loss}$ of the relativistic particles producing pulsed γ-rays should also be smaller than P_0. From the relation $W_{\rm rel} \geq L_\gamma t_{\rm loss}$ and for a loss time of $\sim 1\,$s the total particle energy density can be estimated as $\geq 10^4\,{\rm erg\,cm^{-3}}$. Such high energy densities can only be sustained in the inner accretion disc around the neutron star. The absence of orbital modulation in the γ-ray signal is an indication that the source of pulsed γ-ray emission cannot be confined and so one would expect only short episodes of pulsed emission with a rapidly evolving spectrum. Figure 5.14 shows the kind of spectra that could be associated with emission from a compact source for three different times after ejection: $t = 100\,$s (solid lines), $t = 1\,$h (dashed lines) and $t = 1\,$d (dot-dashed lines). The parent particle population responsible for figure 5.14 consists of electrons, but there are two principal types of model, leptonic and hadronic, for the production of episodic pulsed radiation. Both of these models assume that there is a compact target ('clouds', 'blobs') propagating in the jet and a powerful relativistic energy outflow, in the form of a beam of relativistic particles or an electromagnetic Poynting flux (i.e. momentum is imparted by an electromagnetic wave), that accelerates/injects relativistic particles in the source. It is worth noting that dense, compact gas clouds ($\rho \sim 10^{12}{\rm cm}^{-3}, l \sim 10^8{\rm cm}$) are responsible for the optical emission from the jets in the SS 433 system [82].

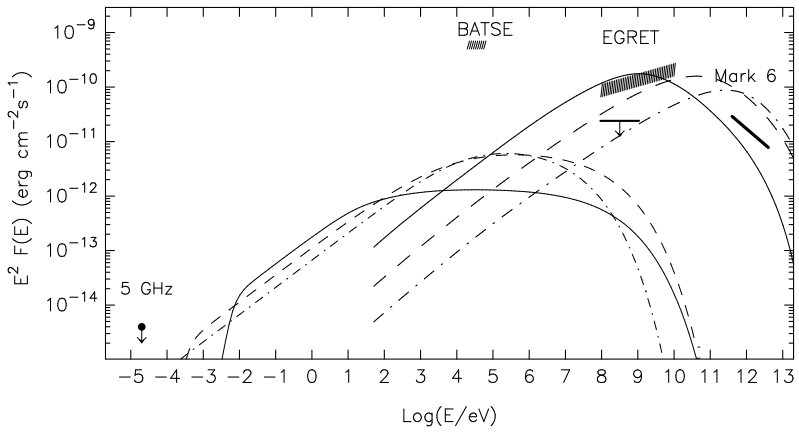

Figure 5.14: The spectra of synchrotron (thin lines) and IC (heavy lines) radiations from a compact fast cloud ('ejecta') propagating in the jet(s) of Cen. X-3 calculated for 3 different times after ejection: $t = 100\,$s (solid lines), $t = 1\,$h (dashed lines) and $t = 1\,$d (dot-dashed lines). The total injection power in shock-accelerated electrons $P_{\rm acc} = 10^{37}\,{\rm erg\,s^{-1}}$ is assumed. The heavy bar at TeV energies corresponds to the mean integral flux of TeV γ-rays detected with the Mark 6 telescope in 1997 [30] assuming a power-law differential spectrum with $\alpha = 2.6$. Taken from [10].

Hadronic beam-target model

This model follows the scheme of [1, 2] which assumes that a powerful beam of relativistic protons accelerated in the vicinity of the pulsar hits a dense plasma cloud. The gas density in the cloud needs to be really high to allow a fast timescale for energy losses by the protons: $n_{\rm gas} \geq 10^{15}{\rm cm}^{-3}$ for $t_{\rm loss} < P_0 \simeq 4.8\,{\rm s}$. A few percent of the injected proton energy will go into Coulomb heating of the cloud to temperatures of $T \sim (5-10)\times 10^4\,{\rm K}$. This results in a very high density UV radiation field in the cloud; the opacity to escaping VHE γ-rays can then be very high, resulting in a hard spectrum of γ-rays. At the same time, the resulting high pressures created by the high temperatures act to make the cloud expand. This means that the timescale of the pulsed γ-ray phase will be relatively short, of order 1 to 2 hours at most, with a rapidly evolving radiation spectrum.

Leptonic model

A leptonic compact source model cannot assume that electrons are accelerated close to the pulsar and then supplied in a relativistic beam to the cloud, as is the case for the protons in the hadronic model, because the lifetime of HE and VHE electrons in the radiation field of the companion star is much shorter than their travel time to distances $\gg 10^{12}\,{\rm cm}$, where the source of γ-radiation should be located [10]. The principal model then follows the scheme of [9], which was developed for microquasars like GRS 1915+105. This model assumes that the inner accretion disc of the compact object in the binary system sporadically ejects a pair of clouds in opposite directions to each other. These clouds are then energised by the Poynting flux from the central engine, modulated at the pulsar period. Relativistic shocks formed at the interface between the ejecta and the wind provide an efficient acceleration region for electrons, resulting in a modulated γ-ray signal Doppler shifted from the pulsar spin period, which would disappear at times $t \geq t_{\rm conf}$. An important implication of the leptonic model is that it does not require the high gas densities in the cloud that the hadronic model requires; this means that Coulomb losses of the relativistic electrons are low and so the cloud will not be heated to the very high temperatures of the hadronic model. This means that it is the UV radiation field of the companion star that becomes the dominant source of absorption to the VHE γ-ray signal. This model also predicts a fast evolution of the pulsed signal, but importantly the leptonic model also predicts very significant fluxes at later stages of flare evolution at $t \geq 1$ day, after the pulsations have disappeared.

5.6 Summary

The faint, but persistent VHE γ-ray flux from Cen. X-3 of

$$F(> 850\,\mathrm{GeV}) = (2.7 \pm 1.4_{\mathrm{sys}} \pm 0.6_{\mathrm{stat}}) \times 10^{-11}\,\mathrm{cm}^{-2}\mathrm{s}^{-1}$$

shows no evidence for the orbital modulation that would be expected if the γ-ray source were coincident with the compact object [11]. This lack of orbital modulation is also seen in HE γ-rays [104]. A need for relaxing the image parameter cuts was found in order to maintain sufficient γ-ray events in a dataset to provide a robust statistic when testing for modulation of the signal at the pulsar period was demonstrated. This soft cutting yielded an intriguing, although of low statistical significance, episode of Doppler shifted pulsed emission when combined with the theoretical premise that the VHE γ-ray spectrum will be hard in comparison to the background cosmic-ray one. As well as having an effect on the analysis strategy, the value of the spectral slope at TeV energies is an important way of distinguishing between the emission models that may be at work in X-ray binaries. In order to gain accurate spectral information it is necessary to understand the systematic uncertainties of IACTs, one of these uncertainties being the status of the atmosphere at the time of observations.

Chapter 6

Atmospheric modelling

6.1 Motivations

We have seen in chapter 3 that much effort goes into the monitoring of a Cerenkov telescope. The mechanical and electrical systems are calibrated and routinely monitored to give highly accurate information on the working condition of the telescope so that the path of the Cerenkov photons can be traced from the moment they strike a mirror, through to the time their response in a PMT is digitised and recorded. One must remember, however, that the telescope itself is just a small part of the detector package. It is merely the light bucket dipped into the Cerenkov well and we therefore need a good understanding of the most important part of the detector: the atmosphere itself. The atmosphere is the target medium for the high energy particles, the emitter of the Cerenkov photons and the transport medium for those photons. Accurate monitoring of the atmosphere is necessary from the viewpoint of temporal variability within a source and the accurate determination of fluxes and energy spectra of TeV γ-rays.

Any bulk absorber between the telescope and the air shower can affect the count rate of a telescope. This can be as obvious as a cloud passing across the field of view, which will give a very noticeable drop in the count rate itself (see figure 3.2), or a sub-visual cirrus that affects the count rate in a more subtle way (see figure 3.3). It is important to classify whether any change in count rate is due to variation within a source or due to changing observational conditions. The importance of correcting for atmospheric conditions has been recognised when studying the detailed structure of flares in observations of the blazar Mrk 421 by the Whipple collaboration [62]. Chapter 5.4.1 also demonstrated that a lack of orbital modulation to the VHE γ-ray signal in Cen. X-3 is an indicator that the

γ-ray emission site is not located within the pulsar orbit. As the orbital cycle of this object covers 2 days it is important to know that any night to night variation in signal is down to the object itself and not to different atmospheric conditions between observations. Whilst this was probed by plotting the number of γ-rays per cosmic-ray as a method of assessing the signal strength independent of the daily variations of the telescope, this assumes that the γ-ray and cosmic-ray spectral slopes are similar, an assumption not borne out with theoretical models for emission from Cen. X-3. This could introduce a systematic bias into the data and so a better method would be to plot the absolute flux of γ-rays as a function of phase.

Calculations of the flux from an object are dependent on simulations of a telescope's perfomance being made to work out the effective collection area (see chapter 2.4.3). These simulations, as we will see in section 6.4.2, require an accurate determination of the atmospheric conditions at the telescope site. An uncertainty in the magnitude of the effective collection area will give an error in the deduced flux; meanwhile, an uncertainty in the function of the collection area with energy will result in errors for the spectral slope determined for any source. An important tool for differentiating between emission models is through the comparison of theoretically modelled energy spectra with observationally obtained ones.

The monitoring of the atmosphere by mid-infrared radiometers has been discussed in chapter 3.5. Water vapour is the prime time-variable quantity in obscuration of the Cerenkov light (due to cloud formation). Monitoring of the 8 to 14 μm emission of the atmosphere is a good way of tracing the variability of the water vapour concentration in the atmosphere and provide an accurate and reproducible method of calculating the quality of data. This information can also be fed into the simulations of IACTs to enable more accurate flux and energy determinations to be made.

6.2 Correlating count rate and sky temperature

The correlation between telescope count rate and sky brightness temperature, as measured by an infra-red radiometer, has been demonstrated in figures 3.2, for the Mark 6 telescope, and 3.3, for CT 6 of the HEGRA array. The correlation can be more readily seen by focusing on one run in figure 3.3 between 22:00 and 22:42 hours, given in figure 6.1(a). This is an on-source/off-source observation which means it tracks across the same part of the sky for nearly a full hour, yielding 150 data points for analysis. The observation

covers zenith angles from $35.3° \leq \theta \leq 39.1°$ which means that the alteration of sky brightness temperature and telescope count rate due to zenith angle changes should not be important. The correlation of the KT 19 reading and the CT 6 count rate is then plotted in figure 6.1(b). The correlation co-efficient for run 20441 is $\rho = -0.896$, showing a good inverse correlation between sky brightness temperature and telescope counting rate.

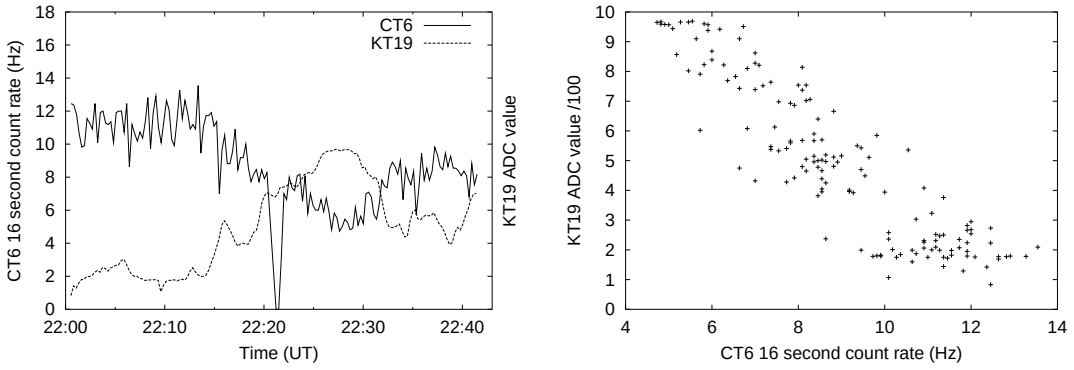

(a) (b)

Figure 6.1: HEGRA run 20441 on and off source. The count rates are the 16 second average count rates for CT 6, the sky brightness temperature was taken with a KT 19.82 infra-red radiometer. The data was taken on the night of 24/9/00. The individual values are shown in the left hand plot and their correlation in the right hand plot. The drop of the CT 6 rates to zero correspond to the changeover from on-source to off-source observing.

6.2.1 Zenith angle variation of sky brightness temperature

The brightness temperature of the atmosphere varies with the zenith angle of the patch of sky being observed; the closer to the horizon you look the warmer the atmosphere appears. This is an intuitive relation since as the thickness of the atmosphere increases with viewing angle, the amount of atmosphere contributing to the infra-red flux increases, and so the sky will appear warmer to the observer. The natural assumption, especially when describing zenith angles of $\leq 60°$ (a plane parallel atmosphere regime), is to assume that the longwave radiation scales as $\sec(\theta)$. Unfortunately the data do not completely support this assumption.

Figure 6.2 represents the change in infra-red flux (given by $F = \sigma T^4$, where $\sigma = 5.67 \times 10^{-8}\,\mathrm{W\,m^{-2}\,K^{-4}}$ is the Stefan-Boltzmann constant) with zenith angle for four days

that had clear skies (for Durham) in May 2001 as measured by the KT 19. Figure 6.2(a) shows the ratio of infra-red flux at zenith ($\theta = 0$) to the flux at some zenith angle $0^\circ \leq \theta \leq 60^\circ$ with respect to $\sec(\theta)$. Plotting the ratio of fluxes removes any dependence on systematic differences between the days and will allow for comparison between the KT 19, KT 17 and the modelled data later on, provided that the response of the detector is linear over the full temperature range experienced. It can be seen that there is a relation between infra-red flux and $\sec(\theta)$, but it is not a linear one. If we assume that

$$\frac{F(\theta)}{F(\theta = 0)} = k \sec^n(\theta) \tag{6.1}$$

where k and n are constants, then plotting

$$\begin{aligned} \ln\left(\frac{F(\theta)}{F(\theta = 0)}\right) &= n \ln(\sec(\theta)) + \ln(k) \\ y &= mx + c \end{aligned}$$

will allow us to determine the relation between infra-red flux and zenith angle. Figure 6.2(b) plots the ln(flux ratio) vs ln[$\sec(\theta)$]. The lack of an intercept shows there is no scaling factor, i.e. $k = 1$. The values for the gradient n are given in table 6.1; combined they give a mean $\overline{n} = 0.32$ with a standard deviation of $\sigma_n = 0.01$. Further measurements at different times of the year would be necessary to determine if the value of n changes with season.

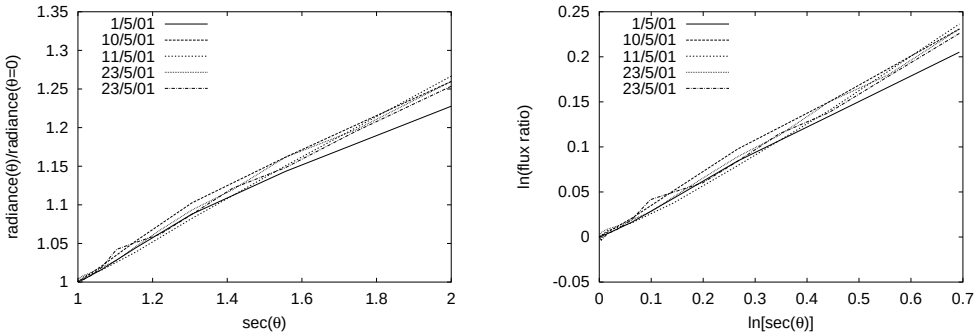

(a) (b)

Figure 6.2: The variation of infra-red flux with zenith angle.

We now have a relation that allows us to calculate the sky brightness temperature as a function of zenith angle. This, in theory, would allow us to co-axially mount a radiometer on a Cerenkov telescope and, given the knowledge of the infra-red flux at zenith, allow us

date	n
1/5/01	0.3 ± 0.003
10/5/01	0.338 ± 0.004
11/5/01	0.329 ± 0.008
23/5/01 (a)	0.330 ± 0.003
23/5/01 (b)	0.323 ± 0.004

Table 6.1: Determining n in the variation of IR flux with zenith angle

to determine the relative clarity of the sky both through a night's observing and between different nights. If we could relate the observable properties of the atmosphere to absolute properties of the atmosphere it would aid considerably when it comes to simulations of the telescope performance. The previous analysis of KT 17 data by this group involved an empirical relation of the screen level temperature and relative humidity to the 8 to 14 μm flux at zenith for an instrument with a 2 degree field of view [19, 49] a discussion of which follows.

6.2.2 The Idso model

The longwave downwelling radiation of the atmosphere has been empirically modelled many times, see [84] for a review. The infra-red emission of the atmosphere at zenith in the 8 to 14 μm band has been reduced to a function of screen level vapour pressure (p_{w0} in mb) and temperature (T_0 measured in K). An equation derived from work done by Idso [49] that describes the fraction of radiation seen by a radiometer with a 2° field of view was adopted by the Durham group [19], with a slight modification to account for the differences between an Arizona sky (where Idso performed his observations) and a Durham sky (where the KT 17 was evaluated), to give

$$F(\theta = 0) = \epsilon_a \sigma T_0^4 \tag{6.2}$$

where $F(\theta = 0)$ is the flux at zenith in W m^{-2} and

$$\epsilon_a = 0.22 + 2.98 \times 10^{-8} p_{w0}^2 \exp(3150/T_0)$$

Measuring the infra-red flux in the 8 to 14 μm band either at zenith or in conjunction with equation 6.1 would then allow the characterisation of sky clarity, provided the Idso formulation gives an accurate reflection of the infra-red flux of a clear sky at zenith. Figure 6.3 combines the sky brightness temperature measured by the KT 19 on 27/3/02 in Durham with the calculated range of temperatures that the Idso model would allow

from measurements of the screen level temperature and relative humidity as given by the Meteorological Office (Met. Office) instruments from the weather station at the Observatory in Durham. The maximum and minimum screen level temperatures for the hour are also displayed (with the values being given on the right hand y-axis). These values combined with measurements of the relative humidity give the allowable range of clear sky brightness temperatures by the Idso model (between the lines). The relative humidity was converted to screen level water vapour pressure by relating it to the saturation water vapour pressure $e_s(T)$ as given by [39]

$$e_s(T) = 2.504 \times 10^9 \exp\left(-\frac{5417}{T}\right)$$

As can be seen, the Idso model fails to give an accurate reflection of the sky brightness temperature. Whilst excursions above the Idso implied temperature could be attributed to cloud in the field of view, the Idso temperature should be thought of as a lower temperature bound, i.e. the observed brightness temperature should not go below the Idso temperature, which is quite plainly not the case from figure 6.3. This shows that whilst an empirical method for determining the sky brightness temperature is a worthy aim, there is a need for more accurate modelling of the atmosphere if any useful conclusions are to be made.

6.3 Modelling the atmosphere

The important thing for air showers is the path length travelled in $\mathrm{g\,cm^{-2}}$. This is related to the density (ρ) of material, which in turn is related to the temperature (T) and pressure (p) of the atmosphere. It is important to know how the pressure, temperature and density of the atmosphere vary with altitude.

6.3.1 Variations due to altitude

In an ideal atmosphere, assume hydrostatic equilibrium

$$\mathrm{d}p(z) = -g\rho(z)\mathrm{d}z$$

where g is the acceleration due to gravity, z the altitude, p the pressure and ρ the density. Taking g as constant all through the atmosphere and the equation of state for a perfect gas

$$\rho(z) = \frac{MM_0p(z)}{kT(z)}$$

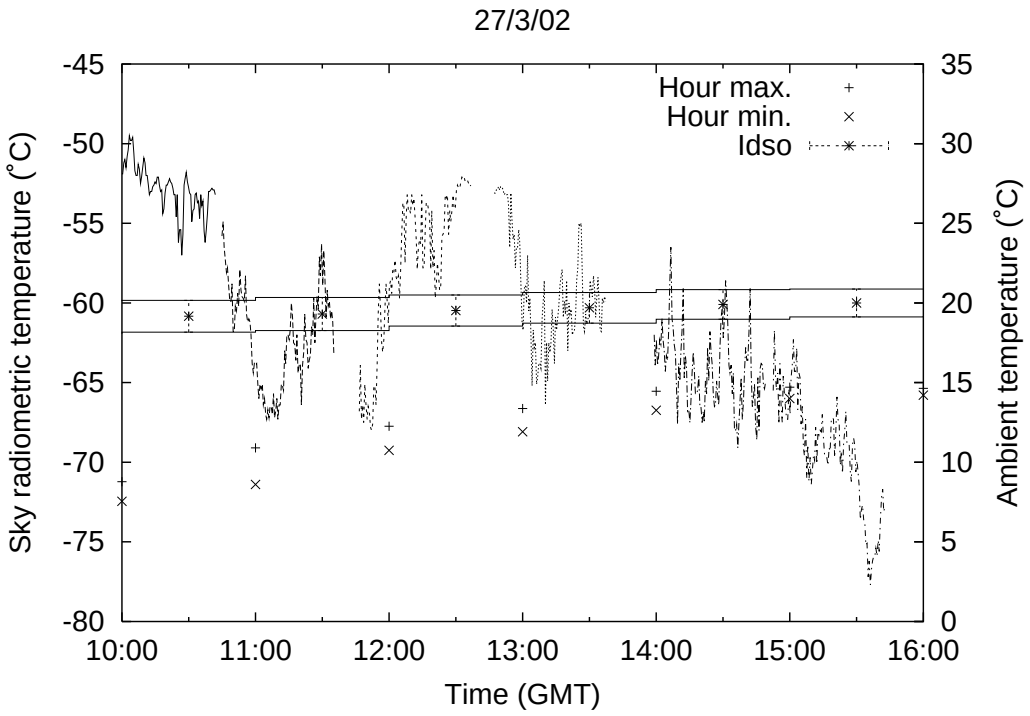

Figure 6.3: Comparing the Idso derived allowable clear sky temperature ranges with measurements made by the KT 19 in Durham on 27/3/02. The left y-axis plots the observed sky brightness temperature and the calculated range of clear sky temperatures as calculated by the Idso model adapted for Durham skies [19]. This range of temperatures is calculated from the relative humidity and the hourly maximum and minimum screen level temperatures as measured by the Met. Office weather station located at the Observatory in Durham. These temperature values are plotted on the right hand y-axis for reference.

where M_0 is the atomic mass unit, M is the average molecular weight of the atmosphere (~ 28.97) and k the Boltzmann constant, therefore

$$\frac{\mathrm{d}p}{p} = -g\frac{MM_0}{kT(z)}\mathrm{d}z = -\frac{\mathrm{d}z}{H(z)}$$

Assuming T is constant (an isothermal atmosphere) then

$$p(z) = p_0 \exp\left(-\frac{z}{H}\right) \tag{6.3}$$

where H is the scale height of the atmosphere. A similar exponential function then also exists for density.

A constant scale height for the atmosphere is reliant on the temperature of the atmosphere being constant, which is far from the case. The atmosphere can be split into several zones, each of which display different temperature behaviours. Of the four main regions only the troposphere and stratosphere are of primary importance to Cerenkov astronomy

- Troposphere (0 to 17 km). Approximately 75% of the atmospheric mass is contained within the troposphere. This region is where all of the weather happens due to vertical motion of air parcels. It is characterised by a steady, linear decline in temperature, until the tropopause is reached, which is a region of constant temperature. The altitude at which the tropopause is reached depends on latitude and season. At high latitudes ($> 60°$) this is at about 12 km and increases in altitude as you move to more tropical latitudes, where there is no discernable tropopause, just a reversal of the temperature curve as you enter the stratosphere.

- Stratosphere (17 to 50 km). The stratosphere contains the ozone layer and is also characterised by the change from vertical motion to a series of steady horizontal winds. The chemical reactions from the absorption of UV photons within the ozone layer release energy into the atmosphere and the temperature begins to increase. By 50 km the temperature can be as high as 0°C once more. At this height the temperature becomes constant again as the change over to the mesophere begins

- Mesosphere (50 to 80 km). In the mesosphere the temperature of the atmosphere begins to fall once more. This part of the atmosphere marks the end of homogeneous mixing of the elements and the start of a more heterogeneous mixing in the thermosphere.

- Thermosphere (80+ km). Contains the ionosphere. Again, a region where photo-ionisation and cosmic-ray ionisation release energy into the environment causing temperatures to rise.

Figure 6.4 shows the temperature profiles for six standard model atmospheres, covering differing latitudes and seasons (see section 6.4.1 for further details). The altitude and temperature of the tropopause will vary with season and latitude. During the summer the tropopause is $\sim$ 2 km higher at the poles, consequently allowing the temperature to lapse to a lower value. The troposphere ends at $\sim$ 17 km at the equator, a region which has very little variation between the seasons. The troposphere also does not show any distinctive region of constant temperature (tropopause) in the tropics - instead it immediately turns to the temperature rise behaviour of the stratosphere.

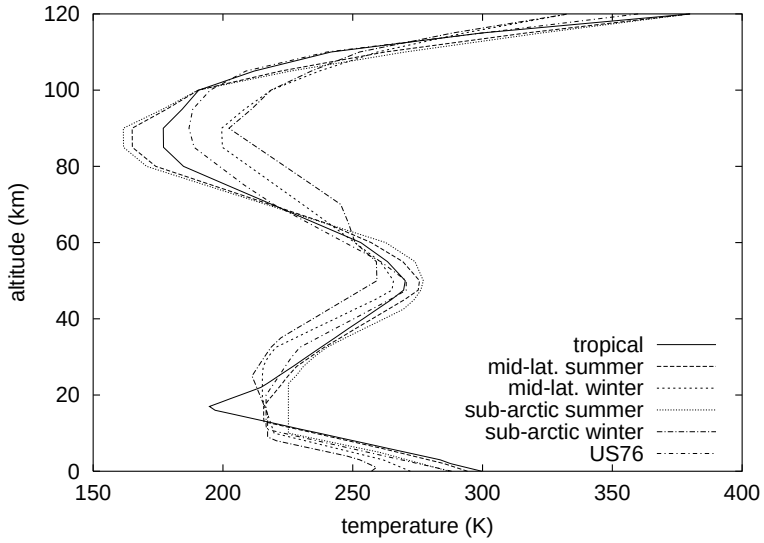

Figure 6.4: Temperature profiles for the six model atmospheres. The altitude and temperature of the tropopause can be seen to vary as a function of latitude and season for the model atmospheres, with the tropical atmosphere having no discernible region of constant temperature at the troposphere/stratosphere boundary.

6.3.2 Temperature lapse rate

The temperature is taken to decrease constantly with altitude until the tropopause is reached. Taking the atmosphere to be in hydrostatic equilibrium, transparent to all radiation and containing no liquid particles the first law of thermodynamics gives

$$C_v \mathrm{d}T + p\mathrm{d}V = \mathrm{d}q = 0. \tag{6.4}$$

Differentiate the equation of state and take $\rho = 1/V$

$$p\mathrm{d}V + V\mathrm{d}p = \frac{k}{MM_0}\mathrm{d}T. \tag{6.5}$$

For an ideal gas

$$\frac{k}{MM_0} = C_p - C_V.$$

Combining 6.4 and 6.5 gives $V\mathrm{d}p = C_p\mathrm{d}T$ and then replacing $\mathrm{d}P$ yields

$$\frac{\mathrm{d}T}{\mathrm{d}z} = -\frac{g}{C_p} = -\Gamma_a \tag{6.6}$$

and the temperature profile varies as

$$T(z) = T_0 - \Gamma_a z. \tag{6.7}$$

For the Earth's atmosphere $C_p \simeq 1000\,\mathrm{J\,kg^{-1}\,km}$ and therefore $\Gamma_a \simeq 9\,\mathrm{K\,km^{-1}}$. The latent heat released by water vapour condensing out of the air serves to raise the temperature lapse rate to $\simeq 6.5\,\mathrm{K\,km^{-1}}$. This means there are three lapse rates for the atmosphere: the effective lapse rate (ELR) which is the actual temperature change with altitude; the dry adiabatic lapse rate (DALR) which is the lapse rate for dry air; and the saturated adiabatic lapse rate (SALR) which is lower than the DALR due to the latent heat released by the condensation of water vapour. For simple modelling purposes the DALR is generally fine for parcels of air for which the relative humidity is less than 60%, above this value the SALR should be used.

6.4 MODTRAN 4

MODTRAN is a FORTRAN written code developed by the Air Force Research Lab., Space Vehicles Directorate, for calculating atmospheric radiance and transmittance. A more detailed description of the program can be found in [58]. The code calculates atmospheric transmittance, atmospheric background radiance, single-scattered solar and lunar radiance, direct solar and lunar irradiance and multiple-scattered solar and thermal radiance. This is at a spectral resolution of $2\,\mathrm{cm^{-1}}$ full-width-half-maximum (FWHM) in averaged steps of $1\,\mathrm{cm^{-1}}$ for the spectral range 0 to $50\,000\,\mathrm{cm^{-1}}$ (200 nm to infinity). There is also a high speed $15\,\mathrm{cm^{-1}}$ resolution band model option for use in UV calculations. MODTRAN uses a three parameter (pressure, temperature and line width) band model for molecular line absorption. The effects of molecular continuum-type absorption, i.e. molecular scattering, aerosol and hydrometeor absorption and scattering are all included.

Representative atmospheric aerosol, cloud and rain models are provided within the code with options to replace them with user-modelled or measured values. Spherical refraction and earth curvature (ray bending) are considered in the calculation of the slant path and attenuation amounts along the path.

The radiatively active molecules are H_2O, O_3, N_2O, CO, CH_4 and CO_2. As far as we are concerned in the mid-IR, the important ones are H_2O with an emission band at 7 μm and continuum emission, O_3 with an emission line at 9.6 μm and CO_2 with an emission line at $\sim$ 15 μm. The MODTRAN code predicted infra-red spectra have been tested against Fourier Transform infra-red Spectrometer (FTS) readings of the atmosphere and been found to agree within a few percent rms errors [58, 99].

6.4.1 Standard atmospheres

There are six reference atmospheres built in to MODTRAN: each defined by temperature, pressure, density and mixing ratios for H_2O, O_3, CH_4, CO and N_2O as a function of altitude covering 0 to 120 km in 50 layers. In addition, atmospheric constituent profiles containing separate molecular profiles for 13 minor and trace gases are provided. Whilst this allows a wide range of default climatological choices, the user also has the option to input model atmospheres. This enables data based upon radiosonde measurements to be included in calculations. The default release of MODTRAN assumes the top of the atmosphere to be located at 100 km above sea-level, but the code was modified to accept the full 120 km range of the reference atmospheres and make it more compatible with simulation codes.

The six pre-defined atmospheric models in MODTRAN are

- Tropical profile: 15 degrees north annual average.
- Mid-latitude summer profile: 45 degrees north July.
- Mid-latitude winter profile: 45 degrees north January.
- Sub-arctic summer profile: 60 degrees north July.
- Sub-arctic winter profile: 60 degrees north January.
- US Standard atmosphere 1976 (US76): profile representing the idealised, steady-state atmosphere for moderate solar activity based on the work of the U.S. Committee on Extension to the Standard Atmosphere (COESA).

The default atmospheric model that has been used in previous simulations of the Mark 6 (and many other Cerenkov telescope) simulations is that of the US76 profile. This has been subsequently found to be an erroneous assumption that can lead to systematic errors in telescope performance.

6.4.2 Model atmosphere dependence on Cerenkov photon yield.

Work done by Bernlöhr [15] has shown the significant impact that differing atmospheric profiles have on the lateral density of Cerenkov photons - a difference of up to 60% near the shower axis. Figure 6.5 shows the lateral distribution of Cerenkov photons as a function of core distance for 100 GeV air showers at an observation altitude of 2200 m (corresponding to the HEGRA telescopes). At moderate latitudes ($\sim$ 30° to 45°), corresponding to the latitudes of present Cerenkov telescope installations, a seasonal effect of 15-20% is apparent and should be included in the energy calibrations of Cerenkov telescopes. The use of inappropriate atmospheric models could lead to systematic errors in absolute flux calibrations.

The reasons for the different light profiles can be seen from figure 6.6 which shows the longitudinal development of showers for four atmospheric profiles. The profiles with lower temperatures in the lower stratosphere and troposphere have the maximum of Cerenkov emission shifted downwards to regions of higher density, which in turn gives a higher index of refraction and therefore higher Cerenkov photon emission efficiency. The actual atmospheric thickness corresponding to the altitude of the maximum of emission remains largely unaffected (varying by only $\sim 5\,\mathrm{g\,cm^{-2}}$), but the thickness of the maximum of emission in the central 50 m increases substantially from the tropical to the antarctic winter profile (by about $30\,\mathrm{g\,cm^{-2}}$).

6.4.3 Radiosonde readings

The impact that different model atmospheric profiles have on the Cerenkov light yield demonstrates the importance of knowing the type of atmospheric model that represents the site of a Cerenkov telescope. Radiosonde readings can give important information on these atmospheric conditions. The term radiosonde is a contraction of radio-sounding device. Radiosondes, at their most basic level, relay temperature, pressure and humidity readings as a function of altitude. The units are floated on weather balloons that can achieve altitudes in excess of 30 km. Wind speed and direction can also be determined by changes in the relative position of the balloon during its flight.

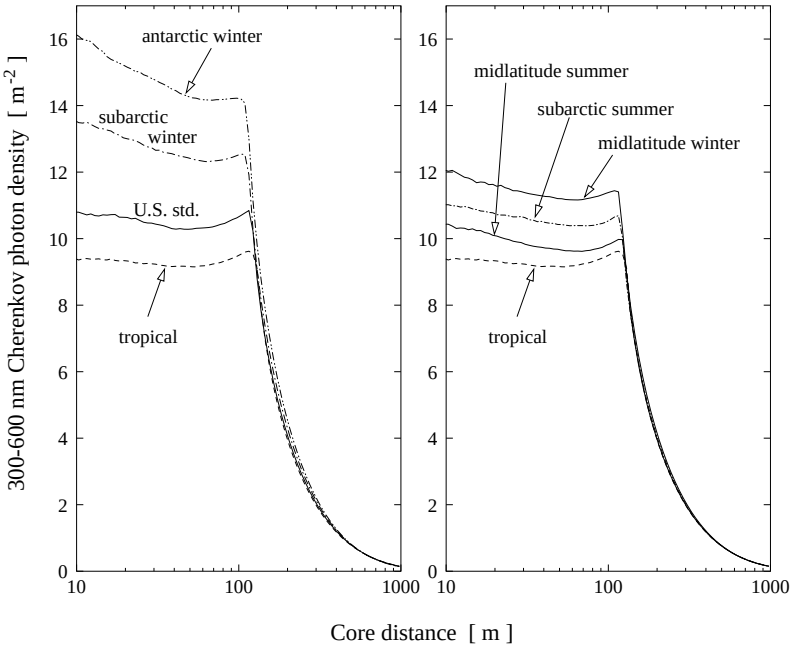

Figure 6.5: Average lateral distributions of Cerenkov light photons in the wavelength range 300-600 nm for vertical 100 GeV gamma-ray showers in CORSIKA 5.71 simulations with different atmospheric profiles (2000 showers simulated for each profile). Absorption of Cerenkov light is taken into account. Observation altitude is 2200 m above sea level. Taken from [15].

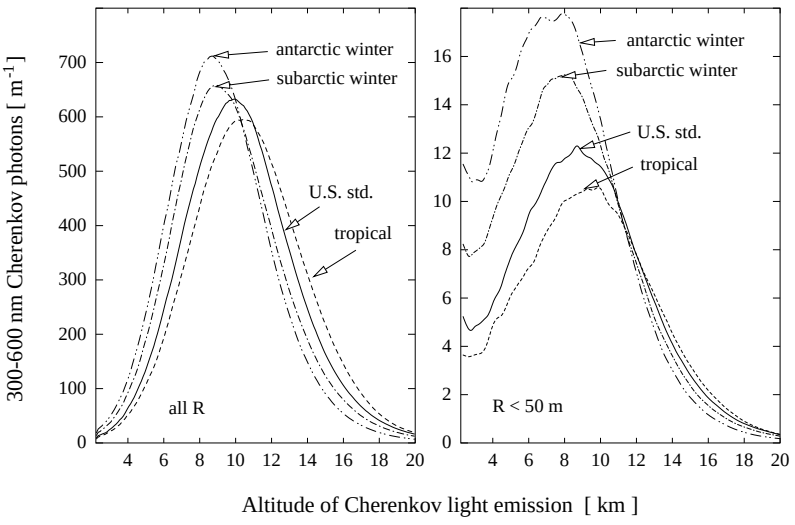

Figure 6.6: Average Cerenkov light emission along the shower axis for vertical 100 GeV gamma-rays with different atmospheric profiles. Left: all emitted photons. Right: photons which should arrive within 50 m from the core at the observation level of 2200 m. No absorption is applied here. Taken from [15].

User supplied profile data can be read into MODTRAN for up to 50 layers allowing the inclusion of actual atmospheric data from radiosondes. The user has the choice of entering gas concentration data in any of several different units, or defaulting to a model atmosphere concentration at the specified altitude. Aerosol vertical distributions, cloud liquid water contents and rain rates can also be input at specified altitudes. The default altitudes for the four aerosol regions may also be modified.

6.5 Infra-red flux as a function of zenith angle with MODTRAN

It is important that the code being used to model the infra-red emission of the sky accurately reflects the actual infra-red emission of the sky. As such it was necessary to compare the simulated infra-red flux of the sky as a function of zenith angle to the actual function (plotted in figure 6.2). Figure 6.7 shows the ratio of the flux at some zenith angle θ ($0^\circ \leq \theta \leq 60^\circ$) to the flux at zenith against $\sec(\theta)$. This plot compares favourably with the distribution seen in figure 6.2. The model atmospheric profiles for this plot all use the default MODTRAN parameters. It is interesting to note that the warmer atmospheres exhibit a shallower temperature distribution than the colder ones. The greatest difference between a warm and a cold atmosphere is in the amount of water vapour it contains. To see the kind of effects that water vapour has on the infra-red profile of the model atmospheres, the column density of water vapour was scaled between 0.5 and 1.5 times the default value. The results of these simulations are presented in figure 6.8. It is the warmer atmosphere types, able to contain more water vapour, that produce the greatest amount of variation, with the sub-arctic winter profile (figure 6.8(f)) having an almost invariant emission profile.

6.6 Generating a Narrabri like atmosphere

The dependence of the Cerenkov signal on the type of atmosphere present around a detector means it is necessary to examine the suitability of the atmospheric parameters used in the simulations of Cerenkov telescopes. Whilst the Mark 6 telescope was fitted with a KT 17 model infra-red radiometer all through its servicable life, the measurements were taken as a cloud monitor and so complete zenith angle plots are scarce. The best available data combining a zenith angle plot and radiosonde readings from a nearby airport

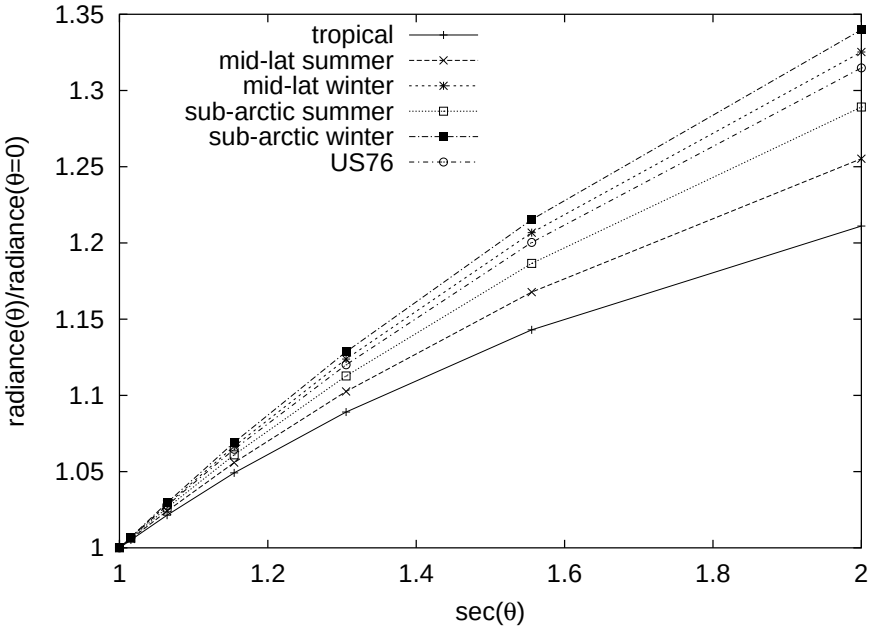

Figure 6.7: The zenith angle infra-red flux variation for default MODTRAN atmospheres

are for February 1999 and specifically the night of 21/2/99, serendipitously a night that has specific significance for the Centaurus X-3 data analysed in chapter 5.

6.6.1 Fitting the Mark 6: Moree readings

Readings from the radiosonde launches taking place at Moree airport (29.48°S 149.83°E) are the closest data available on the altitude variations for the atmosphere for the Mark 6 telescope sited in Narrabri (30.32°S 149.57°E). Radiosonde readings for Moree only go up to ~ 17 km, but as the majority of the atmosphere ($\sim 75\%$) and the maximum height of Cerenkov emission are contained within this region it should be sufficient for modelling purposes. Readings are taken at mandatory and significant pressure levels (such as finding the altitude of the 500 mb level) whereas the model atmosphere data is given as a function of altitude. This means a certain amount of extrapolation must be made to make comparisons between the measured readings and the model values. The radiosonde data were fitted assuming an exponentially decaying pressure profile for three regions. Three regions were necessary to take into account changes in the atmospheric scale height (see section 6.3.1) due to changes in the water vapour density causing a change in the temperature lapse rate (see section 6.3.2). The first region was for 0 to 2 km altitude to take account of any boundary layer; the second went from 2 to 10 km corresponding to a break in the temperature lapse rate due to an increase in relative humidity; and the

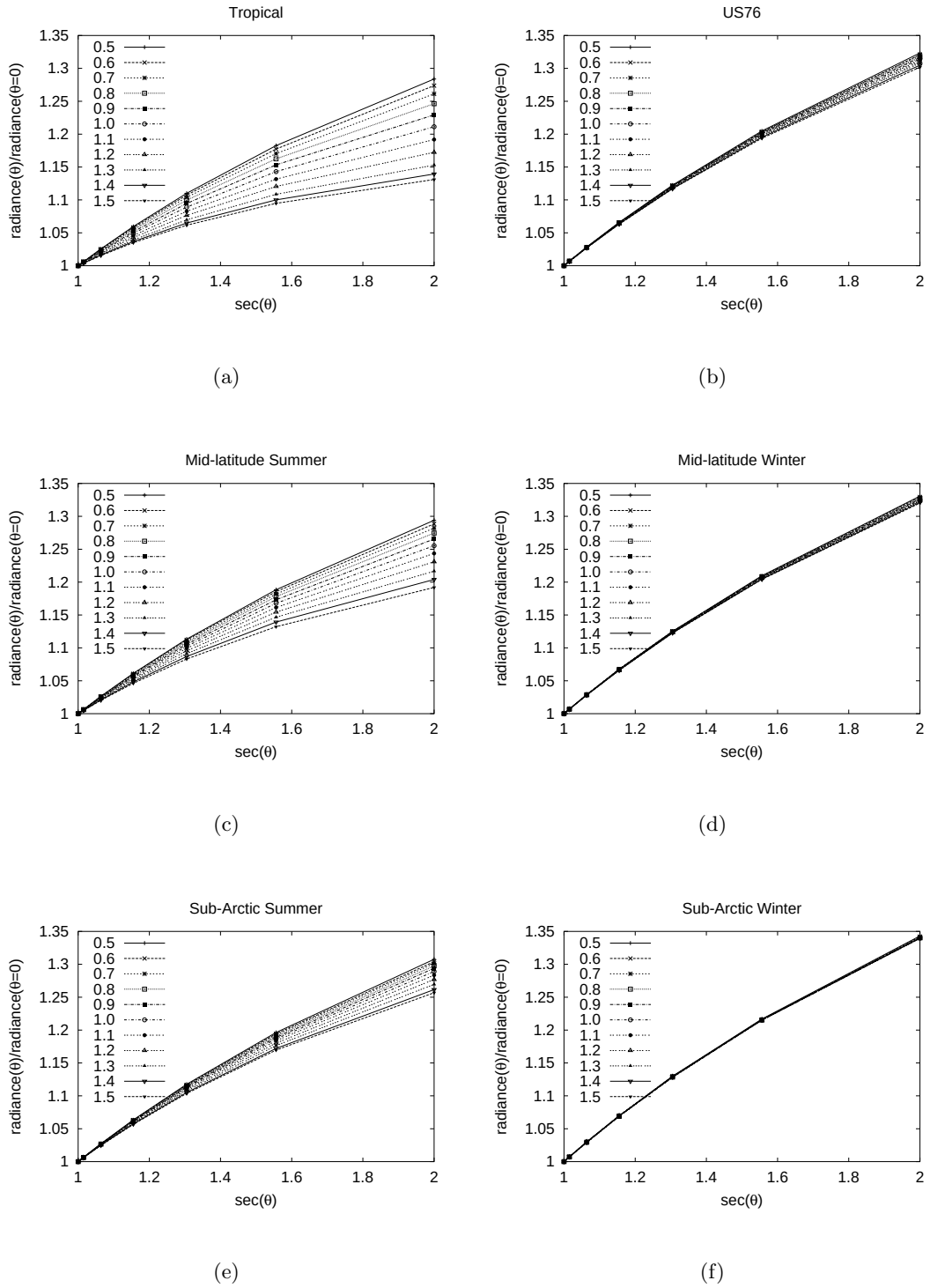

Figure 6.8: The ratio of infra-red flux as a function of zenith angle for the six model atmospheres available in MODTRAN. The water vapour column density scale factor has been varied between 0.5 and 1.5 times the default value for each of the atmosphere types to demonstrate the effect of water vapour on the infra-red flux of the sky.

third zone went from 10 to ~ 17 km where the radiosonde readings ended. The results of these fits were then compared to the pressure values for the model atmospheres provided in MODTRAN. The χ^2 values of this comparison are provided in table 6.2. None of the model atmospheres fit the Moree pressure profile to a good degree of precision, but it can be seen that the mid-latitude summer and tropical profiles give by far the best fits, which is to be expected. Moree is located between the tropical and mid-latitude co-ordinates and the data were taken in the austral summer. The most noticeable aspect of the comparison is that the US76 atmosphere, for a long time the de facto atmosphere used in simulations, is a bad approximation to the Moree data.

Model	χ^2(17 d.o.f.)
Tropical	97
Mid-latitude summer	89
Mid-latitude winter	1968
Sub-arctic summer	1246
Sub-arctic winter	6673
US76	932

Table 6.2: χ^2 values from comparing the 21/2/99 Moree radiosonde pressure values to the model atmosphere profiles obtained from MODTRAN.

The most remarkable feature of the Moree radiosonde data is a lack of any tropopause region, see figure 6.9, something which is reminiscent of the tropical atmosphere. The latitude of Moree would suggest a tropopause beginning at about 15 km altitude, as demonstrated by the COSPAR International Reference Atmosphere (CIRA)[1] for 30° south in February. The CIRA takes radiosonde data from stations around the world and then groups the data according to latitude and season to provide an averaged global atmosphere. As can be seen, even this can not give an accurate model for a localised atmosphere.

Taking the information on temperature and pressure we can work out the density and therefore the thickness of the atmosphere: figure 6.10 shows the numbers for four of the relevant atmosphere types. The tropical and mid-latitude summer atmospheres are the closest approximations to the Moree radiosonde data and the US76 atmosphere was the model type used in the initial simulations for the Mark 6 telescope. Figure 6.11 shows the percentage difference of the thickness for the tropical, mid-latitude summer and US76

[1] further details available at http://www.badc.rl.ac.uk/data/cira/

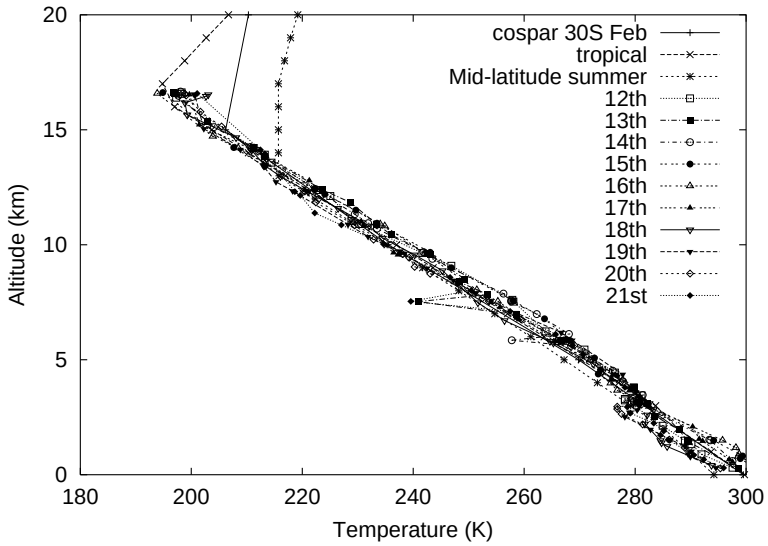

Figure 6.9: Temperature profile of the atmosphere around Moree in February 1999 as taken by radiosonde. Also plotted are the model temperature profiles for the tropical and mid-latitude atmospheres in MODTRAN and the COSPAR International Reference Atmosphere for 30° South in February which is calculated by averaging all available radiosonde data from stations around the world.

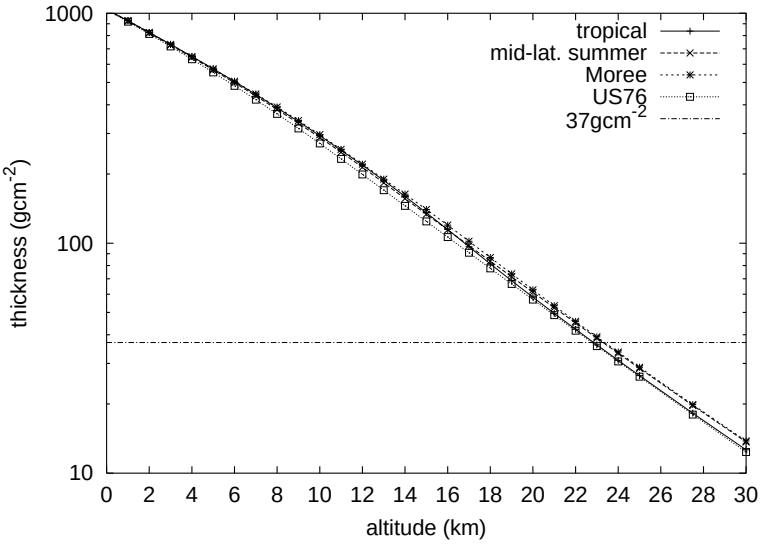

Figure 6.10: The thickness in $\mathrm{g\,cm^{-2}}$ of the tropical (unbroken line), mid-latitude summer (long-dashed line), US76 (dotted line) and the Moree February radiosonde derived (short-dashed line) atmospheric models. Also marked is the $37\,\mathrm{g\,cm^{-2}}$ point (dot-dashed line) which corresponds to the interaction length for a TeV γ-ray.

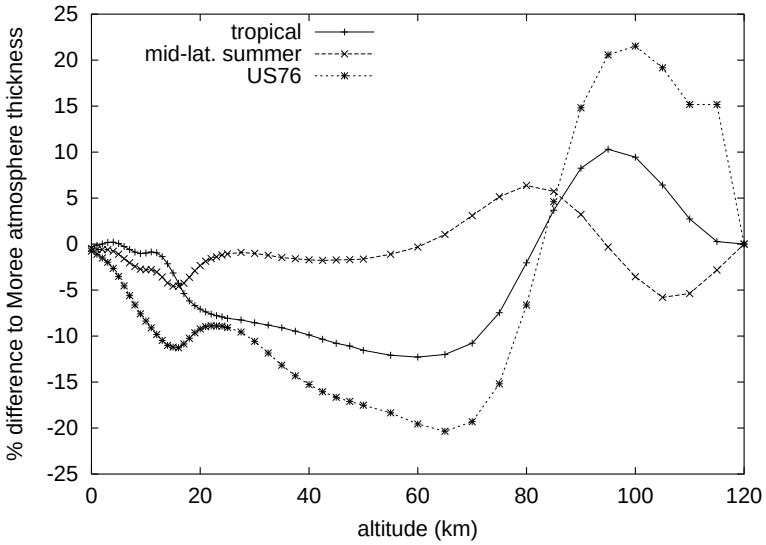

Figure 6.11: The percentage difference in thickness ($\mathrm{g\,cm^{-2}}$) of the tropical (unbroken line), mid-latitude summer (dashed line) and US76 (dotted line) atmospheres to the atmospheric profile for Moree generated from the February 1999 radiosonde data.

atmosphere types to the atmosphere generated from the Moree February radiosonde data. Once again it is the US Standard atmosphere that provides the worst fit, only coming within 5% of the Moree data at 6 km above ground level.

6.6.2 Fitting the Mark 6: the KT 17 data

It is all well and good saying which atmospheric models do and do not fit with the Moree readings, but it is necessary to know that the Moree atmosphere is a reasonable fit to the observed weather conditions in Narrabri before any further analysis can be made. The Moree data were input into MODTRAN for comparison with KT 17 readings taken in Narrabri. The KT 17 readings are given in figure 6.12(a) and the comparison between the ratios of infra-red flux for the KT 17 readings and the MODTRAN results for the Moree atmosphere are then given in figure 6.12(b). The error bars correspond to the uncertainty in the measured temperature value due to the coarse resolution of the ADC measuring the KT 17 output and the inability of the telescope to reach zenith. Within errors the fit between the data sets looks very reasonable, with the fit getting worse at larger zenith angles, an indication that the Narrabri conditions are possibly even drier than the Moree skies; certainly one could not expect the water vapour profile of the atmosphere to be horizontally invariant over the 80 km distance between Narrabri and Moree, so this would

not be surprising.

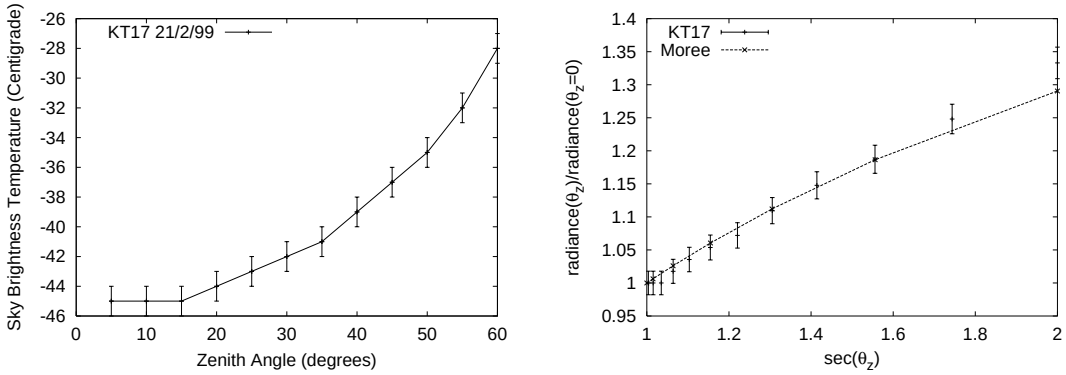

(a) (b)

Figure 6.12: The infra-red flux zenith angle variation for Moree and Narrabri on 21/2/99. The left hand figure shows the measured sky temperature at the Mark 6 site. The right hand figure compares the flux ratios for the KT 17 data and the MODTRAN output for the Moree radiosonde data.

6.6.3 The response of the Mark 6 telescope to different atmospheric models

The response of the Mark 6 telescope was modelled using the MOCCA simulation code [45] and the tropical, mid-latitude summer and Moree type atmospheres for comparison to the original simulations performed using a US76 atmosphere. The resultant effective areas for these atmosphere types are plotted in figure 6.13. There were 50 000 showers generated for each atmosphere type. As one can see, the energy threshold for the telescope stays the same at $\simeq$ 750 GeV and the response of the telescope is consistent above $\sim$ 1 TeV. At lower energies, however, there is a marked reduction in effective area of the telescope in comparison to the US76 atmosphere simulations. The change in effective area for the telescope produces a systematic difference in the fluxes calculated for objects viewed by the Mark 6 telescope, table 6.3 gives the fluxes calculated for the Cen. X-3 data set. The flux derived from the simulations using the US76 atmosphere differs to that calculated from the simulations using the Moree profile by a factor of 1.2 (20%). The new flux values are still within the systematic error calculated for 4.2, which were conservatively estimated at 50% due to uncertainties in the value of the spectral index for Cen. X-3, and the trigger conditions and mirror reflectively for the telescope. This study shows

that there is good reason for a conservative estimate of the systematic errors for the Mark 6 telescope just from an uncertainty in atmospheric conditions alone. The change in effective area at energies of just a few hundred GeV has important implications for the next generation of telescopes. If the next generation of telescopes are required to achieve a low energy threshold then an accurate model of the atmosphere is vitally important because the difference in flux values begins to approach an appreciable amount of the statistical error.

Atmosphere	Flux[$> 850\,\mathrm{GeV}(\mathrm{cm}^2\,\mathrm{s}^{-1})$]
US76	$(2.7 \pm 1.4_{\mathrm{sys}} \pm 0.6_{\mathrm{stat}}) \times 10^{-11}$
Mid-latitude Summer	$(2.9 \pm 1.4_{\mathrm{sys}} \pm 0.7_{\mathrm{stat}}) \times 10^{-11}$
Tropical	$(3.1 \pm 1.6_{\mathrm{sys}} \pm 0.7_{\mathrm{stat}}) \times 10^{-11}$
Moree February 1999	$(3.2 \pm 1.6_{\mathrm{sys}} \pm 0.7_{\mathrm{stat}}) \times 10^{-11}$

Table 6.3: The flux values calculated for the Mark 6 telescope Cen. X-3 data set using different atmosphere types in the telescope simulations.

6.7 Summary

We have seen in this chapter the importance of atmospheric monitoring for Cerenkov astronomy. Atmospheric monitoring yields important information on the count rate behaviour of the telescope and reduces systematic uncertainties for the fluxes from and energy spectra of VHE γ-ray emitting objects by improving calculations of the effective area for a Cerenkov telescope. We have seen how the simple use of the zenith angle variation of the infra-red flux of the sky can give a good indication of the sky clarity. We have also seen that naively using atmospheric data can lead to a seasonal 15-20% systematic error in absolute flux values produced in simulations of standard model atmospheres. These findings have been backed up by data taken of actual atmospheric conditions.

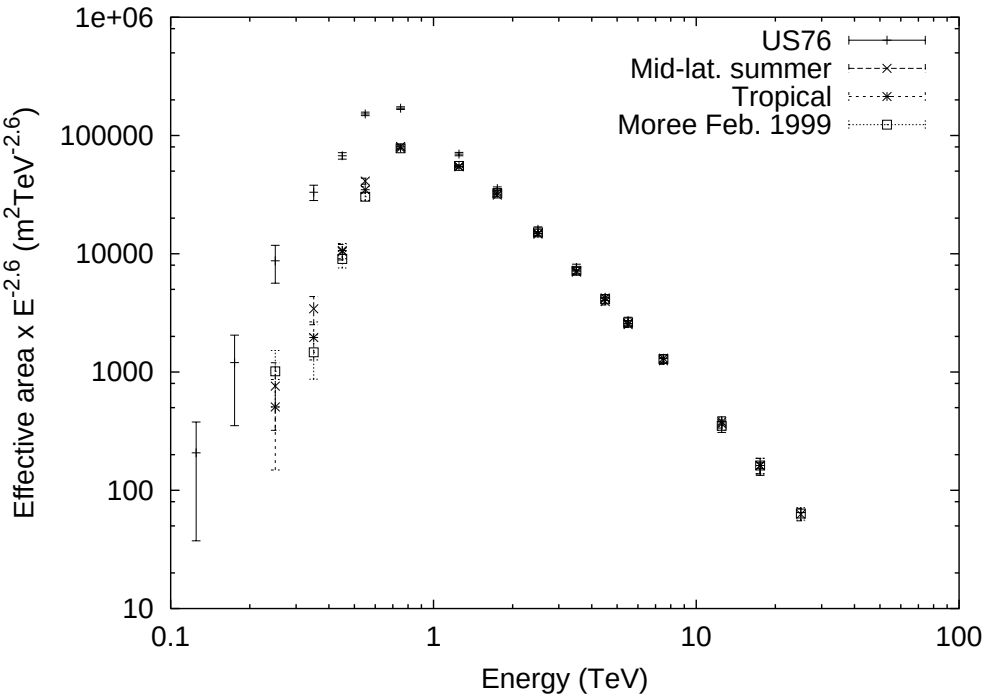

Figure 6.13: Threshold energy of the Mark 6 IACT under differing atmospheric conditions. The original simulations of the telscope are for a US76 atmopshere, which overestimates the effective area of the telescope as compared to that of the mid-latitude summer and tropical types aswell as that of actual atmospheric data for the telescope site.

Chapter 7

Summary, conclusions and the future

7.1 Summary

In this thesis we have seen how the atmosphere has become a useful astronomical tool for detecting the very high energy photons that are emitted by sources of non-thermal radiation. The data obtained with the University of Durham Mark 6 imaging atmospheric Cerenkov telescope, described in chapter 3, from one of these objects, Centaurus X-3, has been discussed in chapter 5. The timing analysis of this data had implications for the theoretical models of VHE emission from X-ray binaries, but showed the need for more accurate results from atmospheric Cerenkov telescopes to draw definitive conclusions. To understand the source physics in an astrophysical object it is necessary to have accurate spectral and timing information for comparison with theoretical models of emission. In order to gain accurate spectral and timing information it is necessary to have an accurate understanding of the detector involved in order to reduce systematic errors. The need for accurate modelling of the atmosphere in telescope simulations in order to reduce systematic uncertainties below 20% was seen in chapter 6. The kinds of measurements that will be provided for the next generation of atmospheric Cerenkov telescopes will be seen in section 7.3.2, but first the conclusions from this study will be given.

7.2 Conclusions

7.2.1 Centaurus X-3

The faint, but persistent flux of VHE γ-radiation from Cen. X-3 has been revised many times as the dataset has been cleaned and as the Mark 6 telescope simulations have been refined. This shows that the large systematic error assigned to the flux calculations for the Mark 6 are well justified, but if the observations of atmospheric Cerenkov telescopes are to relate to meaningful source physics then these errors need to be reduced to acceptable limits. The flux from the whole Cen. X-3 dataset is significant at the 4.34σ level giving a flux of γ-rays above 850 GeV of

$$F(> 850\,\mathrm{GeV}) = (2.7 \pm 1.4_{\mathrm{sys}} \pm 0.6_{\mathrm{stat}}) \times 10^{-11}\,\mathrm{cm}^{-2}\mathrm{s}^{-1}$$

assuming that the atmosphere profiles like that of the US Standard 1976 model atmospheric profile; more shall be said of the appropriateness of this assumption in section 7.2.2.

One of the great inconsistencies in TeV astronomy has been the non-detection of the X-ray binary population following the plethora of claimed detections with non-imaging telescopes. The findings from the analysis of the Cen. X-3 dataset has many implications for both this object and the production of high energy radiation from X-ray binaries in general, but the extraction of definitive conclusions is hampered both by the relative insensitivity of the Mark 6 observations and the broad nature of the analysis strategy. It was unfortunate, but necessary, that the analysis had to be broad in order to test commonly held assumptions that had been used in previous analyses. A few simple tests on the dataset of Cen. X-3 has shown how many of the assumptions used in prior pulsar periodicity searches can be in error. The ability to test for constancy of emission as a function of orbital phase, made possible by the imaging technique, has indicated that the site of VHE emission is not coincident with the compact object, or even in the inner regions of the binary system. This lack of an orbital modulation to the signal is echoed by a similar lack of evidence for orbital modulation in high energy γ-rays from the EGRET detection [100]. This modulation is expected due to the presence of the photon field of the bright companion star giving large values for the optical depth up to and throughout the X-ray eclipse [11]. The most reasonable alternative source for the HE and VHE γ-ray signal is due to jets propagating in the system [10]; jet models have also been successfully used to explain the low/hard state X-ray emission in X-ray binaries [38].

The lack of orbital modulation firstly gives the possibility for a γ-ray signal that has no periodic component at all; secondly, it tells us that if there is any periodic signal it is necessary to expand the period range searched to allow for any Doppler shift of the period and that it is a mistake to focus event times to the X-ray source. It also implies that there is difficulty in containing the source, meaning that any pulsed emission should be short-term and sporadic. This is entirely consistent with the results from non-imaging telescopes. Understanding that pulsed emission is short-term and therefore every γ-ray event time lost by cutting a dataset makes it more difficult to identify pulsed emission is a natural progression from there: the use of hard imaging parameter cuts necessary for maximising the significance of a steady state signal can in fact be destructive in the search for short bursts of pulsed emission in a VHE γ-ray dataset. The softening of the image parameter cuts and widening of the period range searched for the Cen. X-3 data yielded an interesting, but statistically marginal, episode of emission for the night of 21/2/99 based at ~ 2.399 seconds at a $\sim 3\sigma$ level only when combined with a theoretically based assumption [10] of the VHE γ-ray spectrum being hard in comparison to that of the local cosmic-ray spectrum. The evidence for periodicity was found both in a standard frequentist Rayleigh test (see chapter 4.3.3) and from the application of the Bayesian methodology of Gregory & Loredo (see chapter 4.4.3). This value for the period is Doppler shifted from the BATSE derived X-ray half period by 0.37%, corresponding to a bulk motion of $\sim 1100\,\mathrm{km\,s^{-1}}$.

As stated earlier, these results are not of a high statistical significance, but it is possible to see how consistent the results are with theoretical assumptions and previous results. The need for soft cutting in order to maximise the number of γ-ray air showers for the periodicity test, at the expense of the overall significance for any excess events in a dataset, has already been discussed. It is worth noting, however, that the 'softening' of the image cuts essentially only removed the added cut that is afforded by running a three dish system, the remaining cuts were essentially the same as those at the disposal of a single dish system, like that of the Whipple telescope, which have had difficulties in finding significant evidence for emission from X-ray binaries. Soft cut data does not give a statistically significant excess of on-source events and, interestingly enough, neither does the data from single dish IACTs. What of the pulsed episode being based at the second harmonic? Whilst the light curve of Cen. X-3 as seen in the X-rays is generally single peaked, it is known to show a bi-modal behaviour in certain X-ray bands when the system is in the low/hard state; a state which can be characterised by a jet model remember. As for the Doppler shift, since the γ-ray source should not be coincident with

the pulsar this is not a surprising result, but it is also worthy to note that the X-ray binary Hercules X-1 showed evidence for a 0.16% shift in period in the non-imaging telescope data of three separate groups [61, 88, 34]. It is also interesting that the wind speed of the star in Cen. X-3 at $1000\,\mathrm{km\,s^{-1}}$ is twice that of the companion star wind in Her. X-1 [17].

It unfortunately seems that the nature of VHE emission from an X-ray binary is its own worst enemy from a detection point of view: they are faint objects certainly from a d.c. emission perspective; and any periodic component of emission would be sporadic and short term. Looking too deeply for a weak signal in a large amount of noise is always dangerous for accepting a false hypothesis and rejecting a true one. There are measurements that can be made to ensure that the analysis strategy for these objects will have the greatest chance of success in accurately determining the nature of these objects, even if it that is to definitively show that they are not sources of VHE emission. The first task is to identify a system as a $> 5\,\sigma$ source. It is of prime importance for any further observations of the Cen. X-3 system to get a complete observational coverage of the orbit and to reduce the uncertainty in signal size to a sufficient level to be able to say for certain that there is no orbital modulation of the signal. The next step is to gain an accurate value for the spectral slope of any γ-ray emission, for that will give an idea as to the nature of the primary particle population and so the timescale of any periodic component of emission; it will also enable the accurate modelling of datasets from the source so that a dataset can be cut in a way that will give an effective suppression of the background, whilst still maintaining the number of γ-ray events to allow a robust statistical analysis.

The first step to gaining accurate spectral information is in reducing the systematic uncertainties of a telescope. The Mark 6 is no longer functioning, or even intact, with the telescope having been dismantled in April 2000, so there is a very limited amount that can be done to measure and reduce the systematic errors inherent to that dataset. There are, however, lessons that can be learned and information to be gained for the next generation of telescopes from the atmospheric monitoring that took place at the Mark 6 site.

7.2.2 Modelling the atmosphere

An incorrect assumption for the atmospheric profile can introduce a systematic uncertainty of up to 20% in the flux value for a Cerenkov telescope: Bernlöhr demonstrated this in simulations of 100 GeV γ-rays at mountain altitudes [15] and simulations for the Mark 6 telescope confirmed this is still true for a sea-level telescope with an energy thresh-

old at ~ 700 GeV. This is because the differing atmospheric profiles give differing effective collection areas for the Cerenkov light pool. This collection area must be well known over a wide range of energies if the manner that the telescope is to be triggered and the efficiency of the γ-ray selection method are to be accurately simulated. Uncertainties in the magnitude of the effective area result in errors in the deduced flux, while uncertainties in the function of effective area with energy result in errors of the spectral slope determined for any source.

The US Standard 1976 atmosphere was used in the initial simulations of the Mark 6 telescope [6]. By combining the information from a co-axially mounted KT 17 infra-red radiometer about the zenith angle variation of the infra-red flux of the sky for the 21/2/99 with that of radiosondes launched from the nearby Moree airport in February 1999, simulations were made with the MODTRAN 4 atmospheric transmittance code and an atmospheric profile for the Narrabri site was constructed. This atmospheric profile was then compared to a series of standard atmosphere types. The US Standard atmosphere compared disfavourably in all comparisons of pressure, temperature, relative humidity, density and thickness and proved to be an invalid assumption of atmospheric model to be used in simulations of the Mark 6 telescope if systematic uncertainties of less than 50% were desired. The Narrabri February atmosphere was found to be described by either the mid-latitude summer or tropical atmosphere profiles. The tropical atmosphere was found to better describe the temperature profile through the same lack of a definable tropopause and through a similar relative humidity profile at higher altitudes in the troposphere.

It is of interest to note if there is a seasonal variation in the atmospheric profile of the Narrabri site. There are no comparative zenith angle plots for other times of the year, but a comparison of the radiosonde profiles from Moree for the June period by [75] in reference to the Mark 6 PKS 2155-304 dataset found that the tropical atmosphere profile was once again the best model atmosphere type to use.

7.3 The future

7.3.1 The next generation of atmospheric Cerenkov telescopes

It is perhaps due to the myriad benefits of stereoscopic arrays of telescopes that so many of the next generation of IACTs will be based upon this design. The successor to HEGRA, the H.E.S.S. (High Energy Stereoscopic System) project, is being constructed in the Khomas Highlands of Namibia (23.27° N, 16.5° E, 1800 m a.s.l.) at a site that was

shortlisted for the European Southern Observatory, so it is a place with really good skies. The CANGAROO III project has upgraded their telescope to a 10 m diameter mirror and is installing 3 more telescopes of the same class. For the northern hemisphere the Whipple group has expanded into the VERITAS collaboration and intend to build seven 10 m class telescopes at the base of Mount Hopkins (1300 m a.s.l.). The MAGIC (Major Atmospheric Gamma-ray Imaging Cerenkov telescope) project, constructed on the site of the HEGRA telescopes in La Palma, has gone an alternative route of reducing its energy threshold by employing a colossal 230 m^2 surface area provided by 1000 individual mirrors in a single parabolic dish of 17 m diameter. There are even plans afoot, for the not so distant future, to have an array of MAGIC class telescopes working stereoscopically [5].

It is the aim of the next generation of atmospheric Cerenkov telescopes to increase the source catalogues by reducing the flux sensitivities of telescopes to a few thousandths that of the Crab nebula and to be able to differentiate between source physics by having meaningful spectral measurements. The H.E.S.S. telescopes aim to achieve a detection threshold above 40 GeV and a full spectroscopic capability above 100 GeV with an energy resolution of $\leq 20\%$. The H.E.S.S. telescopes should be able to achieve a flux sensitivity of 0.1 Crab in 35 hours and a $7\,\sigma$ detection of Cen. X-3 should come after just 5 hours on-source [92], allowing a rudimentary extraction of an energy spectrum over a reasonably large range ($\sim$ 200 GeV to 5 TeV). It is necessary to understand the systematic errors inherent to the system to a very high standard to be able to deliver on these aims. High resolution energy measurements will allow for the measurement of cut-offs in energy spectra that can distinguish between models of emission, just like the different expected cut-offs can be used to differentiate between the Polar Cap and the Outer Gap models for high energy pulsar emission, as seen in chapter 5.3.1. Much effort can be put into having a large area flux collector for the Cerenkov photons, with a good level of reflectivity so that as many of those photons hitting the mirrors are delivered to the photodetector package. Much effort can go into understanding the way photons are converted into a pulsed signal in the detector package and how that signal is recorded by the data acquisition electronics. Much effort has gone, and will continue to be put, into ensuring that a telescope is running at peak efficiency and that accurate information will be fed into telescope simulations. The atmospheric Cerenkov technique, however, will always be a slave to the weather. One can avoid placing a telescope in an area that is prone to bad weather, but one can not avoid a site known for good weather still having periods of less than optimal viewing conditions. At best one can merely account for the weather conditions that are being

experienced by having good, quantifiable data on those weather conditions.

7.3.2 The atmospheric monitoring for H.E.S.S.

It has already been seen that using an inaccurate model of atmospheric conditions for the region that a telescope is in can provide a 15 to 20% systematic error, this is particularly true for the detection of γ-ray showers in the lower GeV energy reaches, which are more sensitive to fluctuations in shower development and Cerenkov light attenuation. Data taken from radiosonde readings at the nearby ($\sim 100\,\mathrm{km}$) Windhoek airport show the atmosphere to fit a tropical profile well, an advantage of the tropical atmosphere is that it varies little throughout the year, in comparison to high latitudes ($> 40^{\circ}$), and so should provide a stable base model for all calculations. For the purposes of measuring sky clarity there will be co-axially mounted infra-red radiometers on each of the H.E.S.S. telescopes and another infra-red radiometer dedicated to providing an all sky survey every few minutes. This is all well and good for setting a definitive ideal viewing conditions atmosphere, but it is still too coarse an approach for definitive information on the short timescale atmospheric conditions for a telescope. Radiosonde readings give a spot measurement of absolute weather conditions - temperature, pressure and relative humidity - but it is impractical to be continuously sending them up and they can give no information on the aerosol conditions in the atmosphere, an important element in the attenuation of Cerenkov light. Radiometers can tell when a cloud, or obscuring layer, is in the field of view, but it can not tell at what height or how thick this obscuration is. A radiometer can provide a comparative measurement as to the water vapour column density (see chapter 6.5), but the readings are too coarse to be able to discern the visibility of the atmosphere in a numerical sense. A radiometer at best can be used to classify the atmosphere as 'clear', 'hazy' or 'completely obscured'. To be able to distinguish with a higher level of certainty that a lack of low energy events in a night's data is due to an absence of signal or due to the attenuation of the faint amount of light generated in a shower is reason enough to advocate the use of radiometers, but to be able to relate that faint amount of light in a γ-ray image to the actual energy of the primary γ-ray to 20% or less requires a better knowledge of the optical depth profile of the atmosphere at the time that the shower was generated.

Work done by [75] has shown that whilst, thankfully, varying the aerosol content of the atmosphere does not have much effect on the image parameters for γ-ray showers, the triggering rate of a telescope for low energy (of order $100\,\mathrm{GeV}$ γ-ray primaries) can be

greatly affected through changes in the effective collection area of a telescope due to light losses. This has implications for both the calculation of fluxes and energy spectra resolution for a telescope. In figure 7.1 one can see the optical depth as a function of wavelength for light travelling from 10 km to ground level (at 1.8 km a.s.l. for the H.E.S.S. telescopes) for four different aerosol profiles for a tropical atmosphere as generated by MODTRAN 4. The atmospheric model that contains no aerosols obviously has the greatest light transmission; there is a little seasonal variation between a spring/summer model and an autumn/winter model; but the most stark contrast comes when the boundary layer base is shifted by a kilometer, as could be expected in a change from absolutely ideal conditions to a rainy season say. This demonstrates how necessary it is to keep track of the aerosol distribution of the atmosphere.

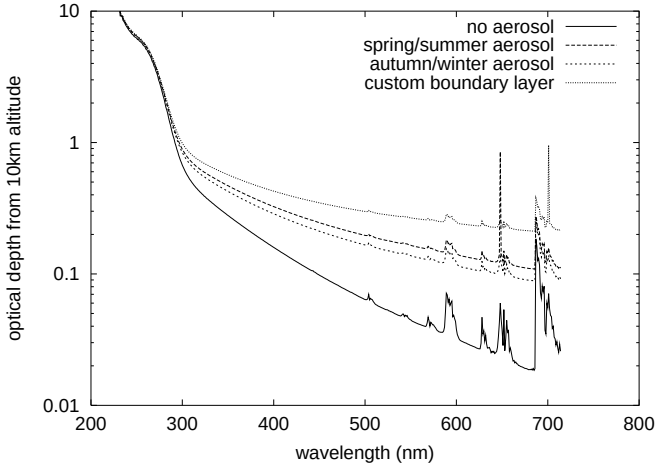

Figure 7.1: Optical depths for the wavelengths of interest to atmospheric Cerenkov telescope simulations for four aerosol profiles in a tropical atmosphere as generated by MODTRAN 4. Values are taken from 10 km altitude down to a ground level of 1.8 km a.s.l., as suitable for the H.E.S.S. telescopes.

The instrument of choice for providing a running snapshot of the aerosol conditions in the atmosphere is a lidar. Lidar stands for light detection and ranging and is an optical equivalent of radar. A laser pulse of known length and power is transmitted into the atmosphere and measuring the magnitude of the light scattered back to a receiver as a function of time gives a quantitative measure of the density of the scattering medium (cloud, dust, molecules, etc) as a function of altitude. The governing equation of the lidar

principle is appropriately known as the lidar equation and is

$$P_r(z) = E_0 \frac{c}{2} \frac{A}{z^2} \beta(z) e^{-2\int_0^z \alpha(z')dz'} \tag{7.1}$$

where

- z is the distance in question.
- $P_r(z)$ is the instantaneous power received from distance z.
- E_0 is the effective pulse energy (taking all optics attenuation into account).
- c is the speed of light.
- A is the receiver aperture.
- $\beta(z)$ is the volume backscatter co-efficient at distance z.
- $e^{-2\int_0^z \alpha(z')dz'}$ is the two-way atmospheric transmittance and accounts for the attenuation of the transmitted and the backscattered power by extinction at various distances (z') between the transceiver and the distance in question (z). The expression equals 1 in an empty atmosphere (i.e., no attenuation).

The volume backscatter co-efficient, $\beta(z)$, represents the amount of light scattered back to the detector. The backscatter is a sum of the components due to molecular scatterers (Rayleigh scattering) and that due to the aerosol component (Mie scattering). The molecular density distribution of the atmosphere is easily modelled (see chapter 6.3.1), as is Rayleigh scattering (see chapter 2.4.2). It is the scattering due to aerosols that presents more difficulties. A simplifying assumption usually made is to assume that the volume backscatter co-efficient is related to the extinction via

$$\beta(z) = k\alpha(z) \tag{7.2}$$

where k is a constant of proportionality known as the lidar ratio and $\alpha(z)$ is the extinction co-efficient (i.e. attenuation in the forward direction). It then becomes a simple matter of relating the amount of backscattered light for the lidar to the extinction profile of the atmosphere to gain the optical depth profile for the atmosphere

$$\begin{aligned} \tau &= \int_0^z \alpha(z).\mathrm{d}z \\ &= \int_0^z \frac{\beta(z)}{k}.\mathrm{d}z \end{aligned}$$

where τ is the optical depth. A useful discussion of the lidar ratio can be found in [103], it can take a value between 0.02 in high humidities to 0.05 in low humdities, but in most cases can be assumed to equal 0.03.

It is the aim for the H.E.S.S. site to eventually have a multiwavelength scanning lidar system to characterise the transmission profile of the atmosphere over the wavelength regions of relevance to the Cerenkov spectrum and the photomultiplier tubes of the camera. The first phase of this was to purchase a commercial ceilometer, of the type that measures cloud bases at airports, and adapt it for the purposes of atmospheric monitoring at an IACT site. The ceilometer in question is a Vaisala model CT25k[1] with a detection range from 0 to 7.5 km in bin steps of 30 m. The unit is eye-safe by employing a 905 nm infra-red solid state laser at low power, allowing continuous unattended operation. As the laser power is low the noise tends to dominate the system, so a data message for each run is the aggregate signal of 65 536 pulses, lasting 100 ns each, at a repetition rate of 5.57 kHz. This means data acqusition takes just over 11 seconds and an atmospheric profile can be generated every 15 seconds if so required. Whilst information on the infra-red attenuation is not directly useful to the blue/UV optical depth information needed for the atmospheric Cerenkov technique, it does mean that the ceilometer can be run coincidentally with the telescopes without adding to the night sky background and allows unattended operation. The 905 nm optical depth profile can be used to gain height information on the aerosol content of the atmosphere, this information can then be fed into MODTRAN to generate optical depth profiles for the wavelengths of interest.

The ceilometer system is still in the early stages of testing, but it is possible to see some of the promise it shows. Plotted in figure 7.2 is a plot of the backscatter as a function of distance from the ceilometer unit at the H.E.S.S. site in Namibia for two data runs taken on the 2/8/02. Each run consists of $\sim$ 100 readings from the ceilometer (which consist of 65 536 laser pulses each). The readings were taken as night fell, which shows in the smaller error bars for the later run - a lower amount of background light in the darker conditions results in a smaller spread of the backscatter values for each bin. The plateau between 1 and 2 km can be attributed to an obscuring layer, indeed that night was unsuitable for observations due to a general haze covering the area that meant even the Gamsberg mountain some 50 km away was not visible during the daytime. An optical depth plot generated from the extinction profile for those readings is given in figure 7.3. Also plotted are the expected optical depth plots for a default tropical atmosphere with

[1] http://www.vaisala.com/page.asp?Section=16216

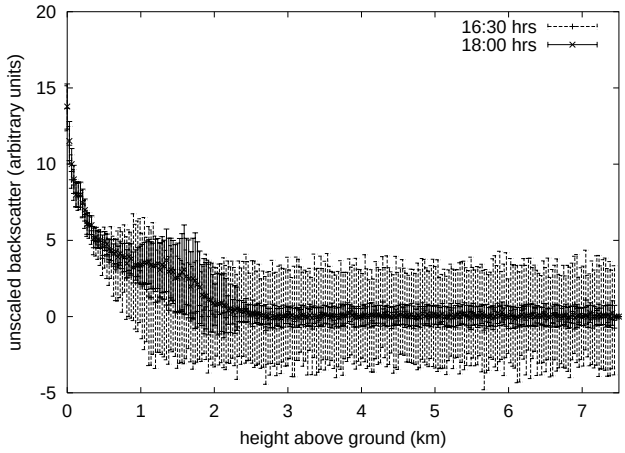

Figure 7.2: Backscatter return values from the ceilometer taken on the H.E.S.S. site on 2/8/02.

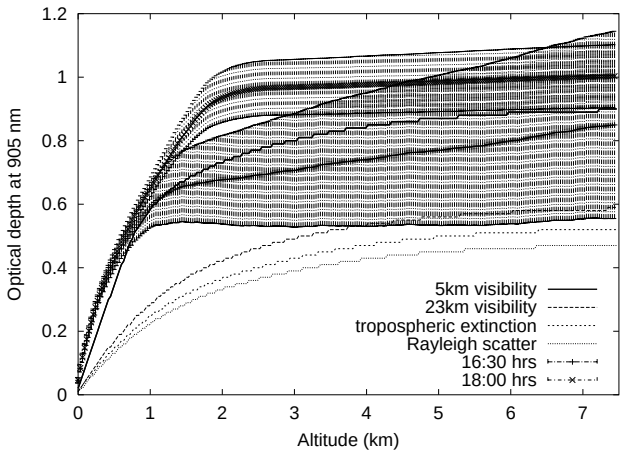

Figure 7.3: Optical depth profile generated from the backscatter profiles in figure 7.2. Also plotted are model optical depth profiles generated by MODTRAN 4 for a default tropical atmosphere with differing aerosol profiles ranging from a pure Rayleigh scattering atmosphere (no aerosols, thin line); a tropospheric extinction (visibility = 50 km, dotted line); a rural profile with visibility at 23 km (dashed line); and a rural profile with visibility at 5 km (thick line).

differing visibilities: the best seeing one could expect from a purely Rayleigh scattering molecular atmosphere; the 50 km visibility conditions of a tropospheric distribution of aerosols; a 'good' seeing scenario with 23 km visibility from a boundary layer with a rural distribution of aerosols; and the 'poor' conditions of 5 km visibility from a rural distribution of aerosols. Here rural means the type of aerosol distribution one could expect in countryside located away from any industrial pollution, such as would be expected from the Khomas Highlands. Visibility is defined according to the Meteorological Optical Range (MOR) visibility as a 5% contrast threshold along a horizontal line of sight. It can be seen that the optical depth profile produced by the 5 km visibility conditions matches the 'poor' observation classification of the night in question and is very different from the profiles for more ideal viewing conditions. The fit is still not an ideal one and could benefit from a classification of the visibility conditions from the lidar data itself as well as inputting the actual heights of the aerosol layers.

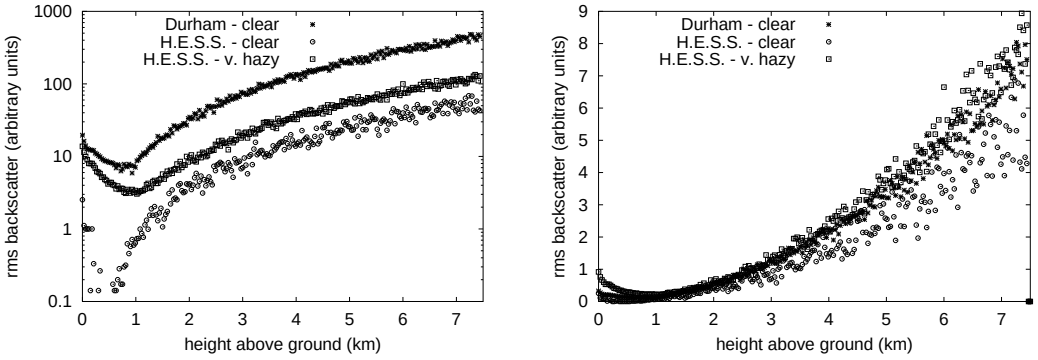

(a) (b)

Figure 7.4: rms distribution of backscatter return values from the ceilometer.

An exact height for the layer is difficult to attribute as the backscatter return values are close to the resolution limit of the ceilometer in the rarefied conditions that make the Gamsberg plateau such a good choice for a telescope in the first place, but there are ways to compensate for this. The ceilometer has an option to scale the power of the returned light in each bin by the square of the distance from the ceilometer that bin corresponds to; this compensates for the inverse square relation of the intensity of light due to distance from the scattering site. Unfortunately as the noise level is independent of height from a measurement point of view, this means that the noise will be correspondingly accentuated with height. Noise, hopefully, is a random process and so will act to cancel itself out over

a large number of measurements, whereas genuine features will be a constant presence and so sum together over these measurements. This is the reasoning behind each ceilometer measurement being the combined result of 65 536 laser pulses after all. As such, by looking at the distribution of a series of ceilometer messages some useful information can be deduced as to the condition of the atmosphere, even if a usable optical depth profile can not generated by readings taken in this mode. Figure 7.4(a) shows the root-mean-square (rms) distribution of the scatter values for each height bin for three different series of conditions: a clear sky in Durham; a clear sky in Namibia; and a hazy sky in Namibia. The y-axis is on a logscale in order that features from all three plots can be easily seen on a single chart. This shift in y-scale magnitude is simply down to the different background light levels experienced by the ceilometer in the different conditions, with the Durham sky giving the largest amount of background light and the clear Namibian sky giving the least amount. Normalising for the background light values, as measured by the ADC on the ceilometer, in figure 7.4(b) shows a remarkable agreement between the differing sky conditions, along with the expected degradation for useful readings from the signal at large distances from the transceiver. It is the distribution along the x-axis that is of importance. For the hazier conditions, corresponding to a greater density of aerosols, the minimum of the rms curve is shifted along the x-axis. The greater the number of aerosols in the atmosphere, the higher into the atmosphere the boundary layer (which is where the greatest amount of light extinction occurs) will penetrate. By measuring where the minimum of the rms distribution occurs we can measure the height of the boundary layer termination and then feed this value into the MODTRAN calculations. When the ceilometer data is combined with water vapour column density values inferred from the radiometer readings and temperature and pressure values from radiosonde data it will allow for an unprecedented accuracy in the atmospheric profile used in the telescope simulations that calculate the effective area for the H.E.S.S. telescopes that is necessary for the accurate calculation of fluxes and spectra for VHE γ-ray emitting objects.

7.4 The end of the beginning

Whilst only a handful of TeV γ-ray sources have been established at present, a summary of these sources with a detection significance of $\geq 5\,\sigma$ being given in table 7.1, with datasets of limited statistical precision, this should change as the next generation of atmospheric Cerenkov telescope installations come online. The increased flux sensitivity

and energy resolution of these detectors should increase source catalogues, allow classification of acceleration mechanisms and show specific characteristics of individual objects; demonstrating the maturity of this field to its peers.

Object	Type	reference
Crab nebula	plerion	[106]
PSR B1706-44	plerion	[56]
Vela X-1	plerion	[109]
SN1006	super	[98]
Cassiopeia A	nova	[4]
RX J1713.7-3946	remnants	[72]
Mrk 421	blazar	[83]
Mrk 501	blazar	[86]
PKS2155	blazar	[27]
1ES2344+514	blazar	[21]
H1426+428	blazar	[47]

Table 7.1: A table of sources with claimed detections of $\geq 5\,\sigma$ by the start of 2002.

References

[1] F. A. Aharonian and A. M. Atoyan. *Ap. J.*, **381**, 220–227 (1991).

[2] F. A. Aharonian and A. M. Atoyan. *Space Sci. Rev.*, **75**, 357–373, (1996).

[3] F. A. Aharonian, A. G. Akhperjanian, J. A. Barrio, K. Bernlöhr, H. Bojahr, O. Bolz, H. Börst, J. L. Contreras, J. Cortina, S. D. V. Fonseca, J. C. Gonzalez, N. Götting, G. Heinzelmann, G. Hermann, A. Heusler, W. Hofmann, D. Horns, A. Ibarra, C. Iserlohe, I. Jung, R. Kankanyan, M. Kestel, J. Kettler, A. Kohnle, A. Konopelko, H. Kornmeyer, D. Kranich, H. Krawczynski, H. Lampeitl, E. Lorenz, F. Lucarelli, N. Magnussen, O. Mang, H. Meyer, R. Mirzoyan, A. Moralejo, L. Padilla, M. Panter, R. Plaga, A. Plyasheshnikov, J. Prahl, G. Pühlhofer, W. Rhode, A. Röhring, G. Rowell, V. Sahakian, M. Samorski, M. Schilling, F. Schröder, M. Siems, W. Stamm, M. Tluczykont, H. J. Völk, C. Wiedner and W. Wittek. *A&A*, **361**, 1073–1078 (2000).

[4] F. Aharonian, A. Akhperjanian, J. Barrio, K. Bernlöhr, H. Börst, H. Bojahr, O. Bolz, J. Contreras, J. Cortina, S. Denninghoff, V. Fonseca, J. Gonzalez, N. Götting, G. Heinzelmann, G. Hermann, A. Heusler, W. Hofmann, D. Horns, A. Ibarra, C. Iserlohe, I. Jung, R. Kankanyan, M. Kestel, J. Kettler, A. Kohnle, A. Konopelko, H. Kornmeyer, D. Kranich, H. Krawczynski, H. Lampeitl, M. Lopez, E. Lorenz, F. Lucarelli, N. Magnussen, O. Mang, H. Meyer, R. Mirzoyan, A. Moralejo, E. Ona, L. Padilla, M. Panter, R. Plaga, A. Plyasheshnikov, J. Prahl, G. Pühlhofer, G. Rauterberg, A. Röhring, W. Rhode, G. P. Rowell, V. Sahakian, M. Samorski, M. Schilling, F. Schröder, M. Siems, W. Stamm, M. Tluczykont, H. J. Völk, C. A. Wiedner and W. Wittek. *A & A*, **370**, 112-120 (2001).

[5] F. A. Aharonian, A. K. Konopelko, H. J. Völk and H. Quintana. *Astropart. Phys.*, **15** 335–356 (2001).

[6] P. Armstrong, P. M. Chadwick, P. J. Cottle, J. E. Dickinson, M. R. Dickinson, N. A. Dipper, S. E. Hilton, W. Hogg, J. Holder, T. R. Kendall, T. J. L. McComb, C. M. Moore, K. J. Orford, S. M. Rayner, I. D. Roberts, M. D. Roberts, M. Robertshaw, S. E. Shaw, K. Tindale, S. P. Tummey and K. E. Turver. *Exp. Ast.*, **9**, 51–80 (1999).

[7] T. D. C. Ash, A. P. Reynolds, P. Roche, A. J. Norton, M. D. Still and L. Morales-Rueda. *M.N.R.A.S.*, **307** 357–364 (1999).

[8] M. C. B. Ashley and J. S. Jurcevic. *Proc. Ast. Soc. Aus.*, **9**, 334–335 (1991).

[9] A. M. Atoyan and F. A. Aharonian. *M.N.R.A.S.*, **302** 253–276 (1999).

[10] A. M. Atoyan, K.-M. Aye, P. M. Chadwick, M. K. Daniel, K. Lyons, T. J. L. McComb, J. M. McKenny, S. J. Nolan, K. J. Orford, J. L. Osborne and S. M. Rayner. *A&A*, **383**, 864–880 (2002).

[11] W. Bednarek. *A&A*, **362**, 646–654 (2000).

[12] A. R. Bell. The acceleration of cosmic rays in shock fronts. I. *M.N.R.A.S.*, **182**, 147–156 (1978).

[13] A. R. Bell. The acceleration of cosmic rays in shock fronts. II. *M.N.R.A.S.*, **182**, 443–455 (1978).

[14] L. Bergström, P. Ullio and J. H. Buckley. *Astropart. Phys.*, **9**, 137–162 (1998).

[15] K. Bernlohr. *Astropart. Phys.*, **12**, 255–268 (2000).

[16] G. R. Blumenthal and R. J. Gould. *Rev. Mod. Phys.*, **42**, 237–269 (1970).

[17] B. Boroson, T. Kallman and S. D. Vrtilek. *Ap. J.*, **562**, 925–935 (2001).

[18] K. T. S. Brazier, et al. In *Proc. 21st Int. Cosmic Ray Conf. (Adelaide)*, **2**, 296 (1990).

[19] D. J. Buckley, M. C. Dorrington, P. J. Edwards, T. J. L. McComb, S. P. Tummey and K. E. Turver. *Exp. Ast.*, **9**, 237–249 (1999).

[20] L. Burderi, T. Di Salvo, N. R. Robba, A. La Barbera and M. Guainazzi. *Ap. J.*, **530**, 429–440 (2000).

[21] M. Catanese, C. W. Akerlof, H. M. Badran, S. D. Biller, I. H. Bond, P. J. Boyle, S. M. Bradbury, J. H. Buckley, A. M. Burdett, J. Bussons Gordo, D. A. Carter-Lewis, M. F. Cawley, V. Connaughton, D. J. Fegan, J. P. Finley, J. A. Gaidos,

T. Hall, A. M. Hillas, F. Krennrich, R. C. Lamb, R .W. Lessard, C. Masterson, J. E. McEnery, G. Mohanty, J. Quinn, A. J. Rodgers, H. J. Rose, F. W. Samuelson, M. S. Schubnell, G. H. Sembroski, R. Srinivasan, T. C. Weekes, C. W. Wilson and J. Zweerink. *Ap. J*, **501**, 616-623 (1998).

[22] M. F. Cawley, D. J. Fegan, K. Harris, P. W. Kwok and A. M. Hillas. *Exp. Ast.*, **1**, 173–193 (1990).

[23] M. F. Cawley in *Towards a major atmospheric Cerenkov detector II*, 176 (Calgary 1993).

[24] P. M. Chadwick, N. A. Dipper, I. W. Kirkman, T. J. L. McComb and K. J. Orford. In *NATO ASIC Proc. 199: Very High Energy Gamma Ray Astronomy*, p. 121–123 (1987).

[25] P. M. Chadwick, T. J. L. McComb and K. E. Turver. *J. Phys. G: Nucl. Part. Phys.*, **16**, 1773–1803 (1990).

[26] P. M. Chadwick, M. R. Dickinson, N. A. Dipper, T. R. Kendall, T. J. L. McComb, K. J. Orford, J. L. Osborne, S. M. Rayner, I. D. Roberts, S. E. Shaw and K. E. Turver. *Ap. J.*, **503**, 391–395 (1998).

[27] P. M. Chadwick, K. Lyons, T. J. L. McComb, K. J. Orford, J. L. Osborne, S. M. Rayner, S. E. Shaw, K. E. Turver and G. J. Wieczorek. *Ap. J.*, **513**, 161-167 (1999).

[28] P. M. Chadwick, K. Lyons, T. J. L. McComb, K. J. Orford, J. L. Osborne, S. M. Rayner, I. D. Roberts, S. E. Shaw and K. E. Turver. *J. Phys. G.: Nucl. Part. Phys.*, **25**, 1223–1233 (1999).

[29] P. M. Chadwick, K. Lyons, T. J. L. McComb, K. J. Orford, J. L. Osborne, S. M. Rayner, I. D. Roberts, S. E. Shaw and K. E. Turver. *J. Phys. G.: Nucl. Part. Phys.*, **26**, L5–L9 (2000).

[30] P. M. Chadwick, M. K. Daniel, K. Lyons, T. J. L. McComb, J. M. McKenny, S. J. Nolan, K. J. Orford, J. L. Osborne, S. M. Rayner and K. E. Turver. *A&A*, **364**, 165–169 (2000).

[31] G. Chodil, H. Mark, R. Rodrigues, F. Seward, C. D. Swift, G. Hiltner, G. Wallerstein and E. J. Mannery. *Phys. Rev. Lett.*, **19**, 681–683 (1967).

[32] G. W. Clark, J. R. Minato and G. Mi. *Ap. J.*, **324**, 974–994 (1988).

[33] Ashok Das and Thomas Ferbel. *Introduction to Nuclear and Particle Physics*. John Wiley & Sons, Inc, 1994.

[34] B. L. Dingus, D. E. Alexandreas, R. C. Allen, R. L. Burman and K. B. Butterfield. *Phys. Rev. Lett.*, **61**, 1906–1909 (1988).

[35] D. J. Bird et al. In *Proc. 25th ICRC (Durban)* **5**, 353–356 (1997).

[36] R. W. Clay et al. In *Proc. 26th ICRC (Salt Lake City)* **OG4**, 421–424, 1997.

[37] R. Fender. 'Relativistic jets from X-ray binaries.' In *'Astrophysics and Cosmology: a collection of critical thoughts.'* W. Kundt and C. van der Brook, editors, Springer (1999).

[38] R. Fender. Energetics of jets from X-ray binaries. *Astrophysics and Space Science Supplement*, **276**, 69–77 (2001).

[39] Robert G. Fleagle and Joost A. Businger. *An Introduction to Atmospheric Physics*, volume 5 of *International Geophysics Series*. New York Academic Press, second edition, 1963.

[40] R. Giacconi, H. Gursky, E. Kellogg, E. Schreier and H. Tananbaum. *Ap. J., (Lett.)*, **167**, L67–L73 (1971).

[41] P. W. Gorham, M. F. Cawley, D. J. Fegan, K. G. Gibbs, R. C. Lamb, D. F. Liebing, N. A. Porter, V. J. Stenger and T. C. Weekes. *Ap. J., (Lett.)*, **308**, L11–L15 (1986).

[42] P. C. Gregory and T. J. Loredo. *Ap. J.*, **398**, 146–168 (1992).

[43] A. K. Harding and J. K. Daugherty. *Advances in Space Research*, **21**, 251–254 (1998).

[44] A. M. Hillas Ann. Rev. Astron. Astrophys., **22**, 425–444 (1984).

[45] A. M. Hillas. In *Proc. 19th ICRC (La Jolla)*, **3**, 445 (1985).

[46] A. M. Hillas. *Space Sci. Rev.*, **75**, 17–30 (1996).

[47] D. Horan, H. M. Badran, I. H. Bond, S. M. Bradbury, J. H. Buckley, M. J. Carson, D. A. Carter-Lewis, M. Catanese, W. Cui, S. Dunlea, D. Das, I. de la Calle Perez, M. D'Vali, D. J. Fegan, S. J. Fegan, J. P. Finley, J. A. Gaidos, K. Gibbs, G. H.

Gillanders, T. A. Hall, A. M. Hillas, J. Holder, M. Jordan, M. Kertzman, D. Kieda, J. Kildea, J. Knapp, K. Kosack, F. Krennrich, M. J. Lang, S. LeBohec, R. Lessard, J. Lloyd-Evans, B. McKernan, P. Moriarty, D. Muller, R. Ong, R. Pallassini, D. Petry, J. Quinn, N. W. Reay, P. T. Reynolds, H. J. Rose, G. H. Sembroski, R. Sidwell, N. Stanton, S. P. Swordy, V.V. Vassiliev, S.P. Wakely and T.C. Weekes. *Ap. J.*, **571**, 753-762 (2002).

[48] J. B. Hutchings, A. P. Cowley, D. Crampton, J. van Paradus and N. E. White. *Ap. J.*, **229**, 1079–1084 (1979).

[49] Sherwood B. Idso. *Water Resources Research*, **17**, 295–304 (1981).

[50] O. C. de Jager. *The analysis and interpretation of VHE gamma ray measurements*. PhD thesis, Potschefstroom University, 1987.

[51] O. C. de Jager, B. C. Raubenheimer and J. W. H. Swanepoel. *A&A*, **221**, 180–190 (1989).

[52] J. V. Jelley. *Cerenkov Radiation and its applications*. Pergamon Press for the United Kingdom Atomic Energy Authority, 1958.

[53] J. G. Jernigan, R. I. Klein and J. Arons. *Ap. J.*, **530**, 875–889 (2000).

[54] P. C. Joss and S. A. Rappaport. *ARA&A*, **22**, 537–592 (1984).

[55] R. L. Kelley, S. Rappaport, G. W. Clark and L. D. Petro. *Ap. J.*, **268**, 790–799 (1983).

[56] T. Kifune, T. Tanimori, S. Ogio, T. Tamura, H. Fujii, M. Fujimoto, T. Hara, N. Hayashida, S. Kabe, F. Kakimoto, Y. Matsubara, Y. Mizumoto, Y. Muraki, T. Suda, M. Teshima, T. Tsukagoshi, Y. Watase, T. Yoshikoshi, P. G. Edwards, J. R. Patterson, M. D. Roberts, G. P. Rowell and G. J. Thornton. *Ap. J. (Lett.)*, **438**, L91-L94 (1995).

[57] R. I. Klein, J. Arons, G. Jernigan and J. J.-L. Hsu. *Ap. J., (Lett)*, **457**, L85–L90 (1996).

[58] F. X. Kneizys, D. C. Robertson, L. W. Abreu, P. Acharya, G. P. Anderson, L. S. Rothman, J. H. Chetwynd, J. E. A. Selby, E. P. Shettle, W. O. Gallery, A. Berk, S. A. Clough and L. S. Bernstein. 'The modtran 2/3 report and lowtran 7 model.'

Technical report, Ontar Corporation, 9 Village Way, North Andover, MA 01845 (November 1996).

[59] W. Krzeminski. *App. J., (Lett.)*, **192**, L135–L138 (1974).

[60] F. K. Lamb, C. J. Pethick and D. Pines. *Ap. J.*, **184**, 271–290 (1973).

[61] R. C. Lamb, M. F. Cawley, D. J. Fegan, K. G. Gibbs, P. W. Gorham, A. M. Hillas, D. A. Lewis, N. A. Porter, P. T. Reynolds and T. C. Weekes. *Ap. J., (Lett.)*, **328**, L13–L16 (1988).

[62] S. LeBohec and J. Holder. astro-ph/0208396

[63] D. A. Lewis, R. C. Lamb and S. D. Biller *Ap. J.*, **369**, 479–484 (1991).

[64] T.-P. Li and Y.-Q. Ma. *Ap. J.*, **272**, 317–324 (1983).

[65] Malcolm Longair. *High Energy Astrophysics: particles, photons and their detection*, volume 1. Cambridge University Press, second edition, 1992.

[66] Malcolm Longair. *High Energy Astrophysics: stars, the Galaxy and the interstellar medium*, volume 2. Cambridge University Press, second edition, 1992.

[67] V. Mannings. *A&A*, **258**, 335–340 (1992).

[68] Vincent Mannings. *TeV Gamma-Ray Emission From Accreting Binary Pulsars*. PhD thesis, University of Durham, 1990.

[69] K. V. Mardia. *Statistics of directional data*. Academic Press, 1972.

[70] I. F. Mirabel and L. F. Rodriguez. *ARA&A*, **37**, 409–443 (1999).

[71] G. Mohanty, S. Biller, D. A. Carter-Lewis, D. J. Fegan, A. M. Hillas, R. C. Lamb, T. C. Weekes, M. West and J. Zweerink. *Astropart. Phys.*, **9**, 15–43 (1998).

[72] H. Muraishi, T. Tanimori, S. Yanagita, T. Yoshida, M. Moriya, T. Kifune, S. A. Dazeley, P. G. Edwards, S. Gunji, S. Hara, T. Hara, A. Kawachi, H. Kubo, Y. Matsubara, Y. Mizumoto, M. Mori, Y. Muraki, T. Naito, K. Nishijima, J. R. Patterson, G. P. Rowell, T. Sako, K. Sakurazawa, R. Susukita, T. Tamura and T. Yoshikoshi. *A & A*, **354**, L57-L61 (2000).

[73] F. Nagase. *Pub. Ast. Soc. Pac.*, **41**, 1–79 (1989).

[74] F. Nagase, R. H. D. Corbet, C. S. R. Day, H. Inoue, T. Takeshima, K. Yoshida and T. Mihara. *Ap. J.*, **396**, 147–160 (1992).

[75] S. J. Nolan. PhD thesis, University of Durham, submitted 2002.

[76] Carl Nordling and Jonny Österman. *Physics Handbook*. Chartwell-Bratt Ltd, fourth edition, 1987.

[77] A. R. North, B. C. Raubenheimer, O. C. de Jager, A. J. van Tonder and G. van Urk. *Nature*, **326**, 567–569 (1987).

[78] A. R. North, et al. In *Proc. 21st Int. Cosmic Ray Conf. (Adelaide)*, **2**, 275 (1990).

[79] R. A. Ong. *Phys. Rep.*, **305** 93–202 (1998).

[80] K. J. Orford. *Exp. Ast.*, **1**, 305–310 (1991).

[81] W. S. Paciesas, G. N. Pendleton, J. P. Lestrade, G. J. Fishman, C. A. Meegan, R. B. Wilson, T. A. Parnell, R. W. Austin, F. A. Berry and J. M. Horack. 'Performance of the large-area detectors for the Burst and Transient Source Experiment (BATSE) on the Gamma Ray Observatory.' In *EUV, X-ray, and gamma-ray instrumentation for astronomy and atomic physics; Proceedings of the Meeting, San Diego, CA, Aug. 7-11, 1989 (A90-50251 23-35). Bellingham, WA, Society of Photo-Optical Instrumentation Engineers*, volume 1159, p. 156–164 (November 1989).

[82] A. A. Panferov. *A&A*, **351**, 156–160 (1999).

[83] M. Punch, C. W. Akerlof, M. F. Cawley, M. Chantell, D. J. Fegan, S. Fennell, J. A. Gaidos, J. Hagan, A. M. Hillas, Y. Jiang, A. D. Kerrick, R. C. Lamb, M. A. Lawrence, D. A. Lewis, D. I. Meyer, G. Mohanty, K. S O'Flaherty, P. T. Reynolds, A. C. Rovero, M. S Schubnell, G. Sembroski, T. C. Weekes and C. Wilson. *nature*, **358**, 477 (1992).

[84] A. J. Prata. *Q. J. Roy. Met. Soc.*, **122**, 1127–1151 (1996).

[85] J. E. Pringle and M. J. Rees. *A&A*, **21**, 1–9 (1972).

[86] J. Quinn, C. W. Akerlof, S. Biller, J. Buckley, D. A. Carter-Lewis, M. F. Cawley, M. Catanese, V. Connaughton, D. J. Fegan, J. P. Finley, J. Gaidos, A. M. Hillas, R. C. Lamb, F. Krennrich, R. Lessard, J. E. McEnery, D. I. Meyer, G. Mohanty,

A. J. Rodgers, H. J. Rose, G. Sembroski, M. S. Schubnell, T. C. Weekes, C. Wilson and J. Zweerink. *Ap. J. (Lett.)*, **456)**, L83-L86 (1996).

[87] B. C. Raubenheimer and H. J. Smit. *Astropart. Phys.*, **7**, 63–71 (1997).

[88] L. K. Resvanis, A. Szentgyorgyi, J. Hudson, L. Kelley, J. G. Learned, C. Sinnis, V. Stenger, D. D. Weeks, J. Gaidos, M. Kertzman, F. Loeffler, T. Palfrey, G. Sembroski, C. Wilson, U. Camerini, J. P. Finley, W. Fry, J. Jennings, A. Kenter, M. Lomperski, R. Loveless, R. March, J. Matthews, R. Morse, D. Reeder and P. Slane. *Ap. J., (Lett.)*, **328**, L9–L12 (1988).

[89] P. T. Reynolds, M. F. Cawley, D. J. Fegan, A. M. Hillas, P. W. Kwok, R. C. Lamb, M. J. Lang, D. A. Lewis, D. J. Macomb, K. S. O'Flaherty, G. Vacanti and T. C. Weekes. *Ap. J.*, **382**, 640–646 (1991).

[90] R. W. Romani. *Ap. J.*, **470**, 469–478 (1996).

[91] G. P. Rowell, P. G. Edwards, J. R. Patterson and G. J. Thornton. *Astropart. Phys.*, **7**, 35–48 (1997).

[92] G. P. Rowell and C. Wiedner. 'Observability of H.E.S.S. targets during november 2001 - may 2002.' Internal note, Max-Planck-Institut für Kernphysik, D 69029 Heidelberg, P.O. Box 103980 (October 2001).

[93] E. Schreier, R. Levinson, H. Gursky, E. Kellogg, H. Tananbaum and R. Giacconi. *App. J., (Lett.)*, **172**, L79–L89 (1972).

[94] S. E. Shaw. *Gamma/Hadron Discrimination using Composite Cherenkov Telescopes.* PhD thesis, University of Durham, 1999.

[95] E. M. Standish. *A&A*, **233**, 252–271 (1990).

[96] J. H. Swank. *Nucl. Phys. B - Proc. Suppl.*, **69**, 12–19 (1999).

[97] T. Takeshima, T. Dotani, K. Mitsuda and F. Nagase. *Pub. Ast Soc. Jap.*, **43**, L43–L50 (1991).

[98] T. Tanimori, Y. Hayami, S. Kamei, S. A. Dazeley, P. G. Edwards, S. Gunji, S. Hara, T. Hara, J. Holder, A. Kawachi, T. Kifune, R. Kita, T. Konishi, A. Masaike, Y. Matsubara, T. Matsuoka, Y. Mizumoto, M. Mori, M. Moriya, H. Muraishi, Y. Muraki, T. Naito, K. Nishijima, S. Oda, S. Ogio, J. R. Patterson, M. D. Roberts,

G. P. Rowell, K. Sakurazawa, T. Sako, Y. Sato, R. Susukita, A. Suzuki, R. Suzuki, T. Tamura, G.J. Thornton, S. Yanagita, T. Yoshida and T. Yoshikoshi. *Ap. J. (Lett.)*, **497**, L25-L28 (1998).

[99] Theriault, J-M. *Pure Appl. Opt.*, **7**, 889–905 (1998).

[100] D. J. Thompson, D. L. Bertsch, C. E. Fichtel, R. C. Hartman, R. Hofstadter, E. B. Hughes, S. D. Hunter, B. W. Hughlock, G. Kanbach, D. A. Kniffen, Y. C. Lin, J. R. Mattox, H. A. Mayer-Hasselwander, C. von Montigny, P. L. Nolan, H. I. Nel, K. Pinkau, H. Rothermel, E. J. Schneid, M. Sommer, P. Sreekumar, D. Tieger and A. H. Walker. *Ap. J., Suppl. Ser.*, **86**, 629–656 (1993).

[101] I. R. Tuohy. *M.N.R.A.S.*, **174**, 45P–50P (1976).

[102] G. Vacanti, M. F. Cawley, E. Colombo, D. J. Fegan, A. M. Hillas, P. W. Kwok, M. J. Lang, R. C. Lamb, D. A. Lewis, D. J. Macomb, K. S. O'Flaherty, P. T. Reynolds and T. C. Weekes. *Ap. J.*, **377**, 467–479 (1991).

[103] D. Veberic, A. Filipcic, M. Horvat, D. Zavrtanik and M. Zavrtanik. hep-ex/0202015v3

[104] W. T. Vestrand, P. Sreekumar and M. Mori. *Ap. J., (Lett.)*, **483**, L49–L52 (1997).

[105] T. C. Weekes and K. E. Turver. 'Gamma-ray astronomy from 10-100 GeV: A new approach'. In *ESA Recent Advan. in Gamma-Ray Astronomy (SEE N78-11899 02-88)*, p 279–286 (July 1977).

[106] T. C. Weekes, M. F. Cawley, D. J. Fegan, K. G. Gibbs, A. M. Hillas, P. W. Kowk, R. C. Lamb, D. A. Lewis, D. Macomb, N. A. Porter, P. T. Reynolds and G. Vacanti. *Ap. J.*, **342**, 379–395 (1989).

[107] T. C. Weekes. *Space Sci. Rev.*, **59**, 315–364 (1992).

[108] N. E. White, J. H. Swank and S. S. Holt. *Ap. J.*, **270**, 711–734 (1983).

[109] T. Yoshikoshi, T. Kifune, S. A. Dazeley, P. G. Edwards, T. Hara, Y. Hayami, F. Kakimoto, T. Konishi, A. Masaike, Y. Matsubara, T. Matsuoka, Y. Mizumoto, M. Mori, H. Muraishi, Y. Muraki, T. Naito, K. Nishijima, S. Oda, S. Ogio, T. Ohsaki, J. R. Patterson, M. D. Roberts, G.P. Rowell, T. Sako, K. Sakurazawa, R. Susukita, A. Suzuki, T. Tamura, T. Tanimori, G. J. Thornton, S. Yanagita and T. Yoshida. *Ap. J. (Lett.)*, **487**, L65-L68 (1997).